# Nanomaterial based Biosensor Powered by Solar Cell

A DISSERTATION
SUBMITTED TO THE FACULTY OF
UNIVERSITY OF MINNESOTA
BY

Bo Zhang

IN PARTIAL FULFILLMENT OF THE REQUIREMENTS
FOR THE DEGREE OF
DOCTOR OF PHILOSOPHY

Advisor: Tianhong Cui

November, 2014

**Acknowledgement**

I would like to give my sincere gratitude to my advisor, Professor Tianhong Cui for his guidance and supports during my Ph.D. study. Professor Cui always encourages me when I encounter failures, and point out the direction when I was lost. Many thanks go to the Professors of the committee, Professor Terry Simon, Professor Ping Wang, and Professor Rusen Yang. I also would like to thank my collaborators, Dr. Min Zhang, Dr. Peng Li. I am also grateful to all my colleagues of the Technology Integration and Advanced Nano/micro Systems Laboratory for the assistance and all the moment we shared. I would like to thank the staff at the Minnesota Nano Center and Characterization Facility for the great helpful discussions on experimental and data analysis. Financial support of this work was provided in part by Minnesota Partnership Funding.

Finally, I would like to give my deepest gratitude to my parents for their endless support. I appreciate the patience and encouragement provided by my dear wife Qiao Li, my good friends, Lingjun Sun, Peng Li, Longzhong Huang, Zonghui Su, Yang Li and Xu Chen, during my PhD study. To all of these great people, I am pleased to express my gratitude.

**Abstract**

Biosensors development using nanomaterials provides promising approaches to offer high performance of sensors in resolution and detection limits. Renewable energy development is attracting interests as an alternative to other sources of energy such as fossil fuels and nuclear energy. Therefore, if biosensor systems can be integrated with nanomaterials and photovoltaics, this biosensor platform can detect various biotargets and support itself by solar energy harvesting with better performance and lower cost. It can reduce cost and pollution from battery or electrical power in a green strategy. It will bridge technological advances in multidiscipline to address fundamental emerging issues in applied science and engineering.

A flexible biosensor based on "bottom up" layer-by-layer self-assembled graphene is investigated. This graphene biosensor can detect different concentrations of biotargets (e.g., glucose, vascular endothelial growth factor, acetylcholine) as a detection platform by measuring the conductance change of the self-assembled graphene. After optimizing of the biosensor structure and dimensions, the suspended graphene sensors are capable of detecting very low concentrations of prostate specific antigen down to 0.4 fg/ml ($4\times10^{-16}$ g/ml), showing a great advantage over conventional testing methods with only 0.4 ng/ml ($4\times10^{-10}$ g/ml) detection limit.

To fabricate solar cell power source, a simple, rapid and robust approach to controllably create nanostructures on a shrink polymer substrate photocathode, demonstrating a 34.1% enhancement of energy conversion efficiency for dye-sensitized solar cells (DSSCs). Glass photoanodes are also replaced with patterned shrink polymer substrates to form the

flexible all-polymer DSSCs. A low-cost shrink lithography technique with 21 nm resolution to support the nanostructure fabrication of biosensor and solar cell in a low-cost way. By using this novel lithography technique, a biosensor based on suspended graphene nanoribbon with only 50 nm width was successfully fabricated. This shrinkage strategy was extended to the fabrication of tunable micro/nano structures with very low cost. These shrink induced micro/nano structures are tunable and controllable on the material properties (e.g. conductance, surface wetting ability, surface morphology), which offering more controllable and flexible applications to biochemical detection and energy harvesting with simple and low cost strategy.

## Table of Contents

Acknowledge……i
Abstract……ii
Table of Contents……iv
List of Figures……vi
CHAPTER 1 ..... 1
INTRODUCTION ..... 1
1.1 Background and Motivation ..... 1
1.2 Objectives of Research ..... 3
1.3 Methodology ..... 4
1.4 Thesis Overview ..... 7
CHAPTER 2 ..... 8
FABRICATION OF GRAPHENE BASED BIOSENSORS ..... 8
2.1 Introduction ..... 8
2.2 Different Fabrication Methods of Graphene and Graphene Composites ..... 9
2.2.1 Mechanical Exfoliation Derived Graphene Biosensor ..... 11
2.2.2 Microfluidic Induced Graphene Biosensor ..... 12
2.2.3 Self-Assembled Graphene Biosensor ..... 16
2.3 Special Structure Biosensors ..... 17
2.3.1 Low-Cost Flexible Biosensor ..... 17
2.3.2 Suspended Graphene Biosensor ..... 18
2.4 Conclusion ..... 21
CHAPTER 3 ..... 23
VARIOUS BIOTARGETS DETECTION OF GRAPHENE BIOSENSORS ..... 23
3.1 Introduction ..... 23
3.2 Sensing Mechanism Discussion ..... 25
3.2.1 Surface Modification ..... 25
3.2.2 Detection Method ..... 26
3.2.3 Sensing Mechanism ..... 27
3.3 Different Biotargets Detection ..... 29
3.3.1 Glucose Detection ..... 29
3.3.2 Multiple Ion Detection ..... 30
3.3.3 Acetylcholine (ACh) Detection ..... 33
3.3.4 PSA Detection ..... 34
3.3.5 Vascular Endothelial Growth Factor (VEGF) Detection ..... 38
3.4 Suspended Graphene Biosensor Performance ..... 41
3.5 Comparison of Different Graphene and Graphene Composite Sensors ..... 44
3.6 Conclusion ..... 48
CHAPTER 4 ..... 50
LOW-COST AND HIGH PERFORMANCE DYE SENSITIZED SOLAR CELL ..... 50
4.1 Introduction ..... 50
4.2 Working Principle of DSSC ..... 51
4.3 High Performance DSSC with Shrink Induced Nanostructures ..... 54

4.3.1 Fabrication Processes ..... 56
4.3.2 Characterize of Shrink Induced Nanostructures ..... 59
4.3.3 Characterization of DSSC ..... 64
4.4 All Polymer and Flexible DSSCs ..... 69
4.5 Conclusion ..... 76
CHAPTER 5 ..... 77
SHRINK INDUCED FABRICATION AND APPLICATIONS ..... 77
5.1 Introduction ..... 77
5.2 Thermoplastic Shrink Lithography and Its Applications ..... 81
5.3 Hydrogel Shrink Lithography and Its Applications ..... 90
5.4 Application of Shrink Induced Nanostructures to Biosensing ..... 102
5.5 Conclusion ..... 111
CHAPTER 6 ..... 113
BIOSENSOR SYSTEM POWERD BY DSSC ..... 113
6.1 Introduction ..... 113
6.2 Self Powered Biosensor System Development and Characterization ..... 115
6.3 Conclusion ..... 120
CHAPTER 7 ..... 122
CONCLUSIONS ..... 122
7.1. Summaries ..... 122
7.2 Conclusions ..... 125
7.3 Future Recommendations ..... 126
Reference ..... 127

## List of Figures

Figure 1.1: Sketch of typical structure of LbL self assembled biosensor……5
Figure 1.2: The ISFET structure of biosensor system and its sensing principles……6
Figure2.1: Sketches of three different types of graphene based biosensors from pure to hybridized graphene composites: (a) mechanical exfoliation method derived graphene biosensor structures; (b) microfluidic method induced graphene composites without introducing other hybrid material; (c) self assembledgraphene hybridized with polymer. (d-f) SEM images of surface profile of pure graphene, microfluidic induced graphene composites, and self assembled hybridized graphene composites, respectively. …….11
Figure 2.2: The fabrication processes of mechanical exfoliation graphene biosensors…12
Figure 2.3:The fabrication processes of microfluidic induced graphene biosensors……13
Figure 2.4: SEM images of (a) microchannel array, (b) sensor structure, and (c) porous surface profile of microfluidic induced graphene films. (d) AFM image of the graphenenanoplatelets deposited randomly across the channel of two electrodes……14
Figure 2.5: AFM was used to characterize the thickness of graphene films in different microchannels with various heights. The thickness of the graphene films were raising along with the increasing of the microchannel heights……..15
Figure 2.6: The fabrication processes of self-assembled graphene biosensors……16
Figure 2.7: (a) AFM image of LbL self assembled graphene (scanning area is 1 μm by 1 μm). (b) SEM image of LbL self assembled graphene displaying its porous defoliation surface profile. The average graphene nanoplatelet is about 100 nm by 100 nm.....17
Figure 2.8: (a) Schematic illustration of self-assembled graphene nanocomposite before immunization. (b) Optical image of self-assembled graphenesensor on a flexible PET substrate.....18
Figure 2.9: (a) 45 ° tilted SEM image of the suspended graphene beam array. The channel length is 10 μm, and the width of the graphene beam is 10 μm. (b) Anchor part of the beam demenstrates the well fixed ends of the graphene beam. Inset: high magnitude of SEM image of LbL self assembled graphene displays its porous defoliation surface profile details. The average graphene nanoplatelet is about 100 nm by 100 nm.20
Fig. 2.10: Normalized noise power spectrum of the graphene biosensor was characterized. Comparison of graphene's noise power spectra with and without suspension situation shows lower level of 1/f noise in suspended devices.....21
Figure 3.1 (a) Schematic illustration of interaction between capture antibodies and target protein molecules in a label free detection. After graphene biosensor modified by capture antibodies encounters PSA solution, the immunoreation will take place, and the conductance of graphene changes. (b) Schematic illustration of a graphene sensor in a labeled detection. HRP labels the different concentration of PSA, and catalyzes the convertion from ascorbic acid to dehydroascorbic acid, causing the local pH shifts. The conductance of graphene is sensitive to pH shifts.....27
Figure 3.2 (a) different concentrations of glucose solution testing results; (b) resolutions of graphene and CNT comparison, graphene based glucose sensor can get 10 pM resolution which is higher than CNT as only 100 pM.....30

Figure 3.3 (a) Schematic of an ISSA: when testing solution contains only one type of ion, only the matched ionophore sensing channel trigersasignal; (b) Pictures of ISSA and measurement system; (c) Structure of ISSA sensing region; (d) Ionphore working mechanism.……....31
Figure 3.4: Testing solution contains only (a) NaCl; (b) KCl; (c) $CaCl_2$; (d) HCl. In order to get clearer readout, normalized conductance was introduced. Conductance under the condition of 1 mM concentration was used as initial conductance $G_0$ , and other conductance tested under different concentrations subtracted $G_0$to get ΔG. Normalized conductance represented as $\Delta G/G_0$.……32
Figure 3.5 (a) different concentrations of ACh solution testing results; (b) resolutions of graphene and CNT comparison, graphene based ACh sensor can get 1 pM resolution which is far higher than CNT as only 1 nM.……...33
Figure 3.6 (a) Shift in conductance versus concentration of PSA for label free graphene sensor. Inset: conductance versus time data recorded after alternate delivery of the following concentrations of PSA: (1) PBS contains no PSA, (2) 4 fg/ml, (3) 4 pg/ml, (4) 4 ng/ml, (5) 4 μg/ml. Initial conductance $G_0$ represents the graphene conductance in PBS solution, and other conductance tested under different PSA concentrations subtracte $G_0$ to get $\Delta G$. (b) Conductance versus time testing was taken place between graphene and CNT biosensors after different concentrations of PSA were delivered. The results show that the detection limit of graphene sensor is down to 4 fg/ml, much better than CNT sensor with a detection limit of only 4 ng/ml.……35
Figure 3.7 (a) Shift in conductance versus concentration of PSA for labeled detection with graphene and CNT biosensors. The detection limit of graphene based sensors is 0.4 pg/ml, showing great advantage over CNT sensors which is only 4 ng/ml. Conductance was normalized by dividing initial conditions which was PBS containing no PSA. (b) Resistance versus time data recorded for labeled graphene sensors detection of different concentrations of PSA. After incubated in various concentration of PSA and labeled by HRP, shifts of graphene resistance were monitored when catalytic reaction started. Resistance was normalized through dividing the resistance at the time when the mixture of ascorbic acid and hydrogen peroxide were induced by the original resistance. (c, d) Similar testing was took place for the detection of normal rabbit antigen IgG. The detection limit of graphene sensors is 4 pg/ml, much better than the CNT sensors with a detection limit of only 40 ng/ml.……37
Figure 3.8 Real-time characterization of biosensor modified by different types of receptors. Resistance versus time data recorded after alternate delivery of the following concentrations of VEGF: (1) deionized water contains no VEGF, (2) 1 pg/ml, (3) 10 pg/ml, (4) 100 pg/ml, (5) 1 ng/ml, (6) 10 ng/ml, (7) 100 ng/ml.……39
Figure 3.9 100 fg/ml and 500 fg/ml VEGF were detected. There were different outputs between 0 g/ml and 100 or 500 fg/ml VEGF. But there was no difference between 100 and 500 fg/ml VEGF measurement results, which confirmed the detection limit was 1 pg/ml.……..40
Figure 3.10 (a) Shift in normalized conductance versus PSA concentration for suspended and unsuspended graphene sensors. The detection limit of suspended device can reach down to 0.4 fg/ml. (b) Conductance versus time testing for suspended (blue curve) and

unsuspended (red curve) graphene with different concentrations of PSA solution induced: (1) PBS contains no PSA, (2) 0.4 fg/ml, (3) 4 fg/ml, (4) 4 pg/ml, (5) 4 ng/ml, (6)4 μg/ml. The results reconfirm that the detection limit of suspended graphene sensor is much better than unsuspended devices. In addition, normal rabbit IgG were delivered to suspended graphene sensor immunized with PSA capture antibodies under the same experiment conditions, and the conductance of graphene sensor kept constant (black curve), demonstrating the specificity of suspended graphene biosensor……...42
Figure 3.11(a) Conductance versus time testing for suspended graphene and CNT biosensors with different PSA concentrations: (1) PBS contains no PSA, (2) 0.4 fg/ml, (3) 4 fg/ml, (4) 4 pg/ml, (5) 4 ng/ml, (6)4 μg/ml. The results show that the detection limit of graphene sensor is down to 0.4 fg/ml, compared with the CNT sensor with a detection limit of 4 pg/ml. (b) Normalized noise power spectrum was also characterized for the suspended graphene and CNT biosensor. The result proves that graphene device has lower 1/f noise……....43
Figure 3.12 (a, b) Change of resistance versus PSA concentration for mechanical exfoliation graphene biosensors. The detection limit is 40 pg/ml. (c, d) Shifts of resistance versus PSA concentration for microfluidic induced graphene biosensors. The detection limit is 4 pg/ml. (e, f) Shifts of resistance versus PSA concentration for self assembled graphene biosensors. The detection limit is 4 fg/ml. The data for figures in the right was extracted from the stable region of the real time conductance measurement curve in the left. After delivering the PSA solution each time, it takes several minutes for the resistance to get stable, allowing sufficient inmunoreaction and avoiding the disturbance generated by the delivery of PSA solutions.....46
Figure 3.13 Sensitivity analysis of different graphene biosensors. The self assembled graphene presents the highest sensitivity.....46
Figure 3.14 Long term stability analysis of different graphene biosensors……...47
Figure 4.1The basic structure of typical DSSC…….53
Figure 4.2 (a) Scheme of the fabrication process of shrink induced wrinkles and nanogaps. The shrink polymer substrate with wrinkles and nanogaps generated on the top surface will serve as photocathode. (b) Scheme of DSSCs incorporating with shrink induced structures. (c) Scheme of the photocathodes utilizing shrink induced wrinkles and nanogaps to enhance the incident light scatteringand Pt catalytic area…….55
Figure 4.3 (a) SEM image of wrinkles generated from shrunk Pt film 50 nm thick without ITO layer. (b) SEM image of wrinkles and nanogaps obtained from shrink ITO/Pt films with 30/50 nm thick. Inset: the disc-shaped 2D FFT pattern, indicating a broad distribution of wavelength in k-space. (c) Wavelength distributions of shrink induced nanostructures are generated fromdifferent bilayers with various thickness of ITO layer, but the Pt films are kept as 50 nm thick.The larger wavelength peak represents the wrinkles and the smaller one is for nanogaps.Two spectra peaks are measured by introducingthe ITO films, but only one peak appears without ITO film, which confirms that fragile ITO layer causes the nanogaps……60
Figure 4.4 SEM images of different thickness of ITO layers incorporated with 50 nm Pt film deposited on PS substrate after shrinking……..61

Figure 4.5 (a) The current densities versus voltage characteristics of the DSSCs with various shrink induced nanostructures due to different thickness of ITO layers. Only properly designed structures can enhance the ECE greatly. (b) IPCE spectra of DSSCs with different photocathodes. The nanogaps with 200 nm and 300 nm wavelength, generated by ITO with 16 nm and 30 nm thick respectively from the quantitative analysis, enable a great IPCE enhancement at incident wavelengths from 300 nm to 400 nm. (c) The optimal DSSC with Pt/ITO 50/30 nm thick presents 34.1% increase of ECE compared with DSSC with the flat photocathode. (d) Long term stability characterization of DSSCs. The DSSCs kept 94% of its initial efficiency after 500 hours at 60° C under a real irradiance of successive outdoor sunlight soaking……..63
Figure 4.6 (a) The current densities versus voltage characteristics of the DSSCs with various shrink induced nanostructures. The ITO layer was kept as 30 nm thick, but the thickness of Pt film was different. (b) The ECE of different samples corresponding to the testing in (a). Ten devices were tested, and the error bars represent standard deviations in values…….65
Figure 4.7 Comparison of DSSCs with same photoanodes but different photocathode area…….66
Figure 4.8 Sheet resistance of different thickness of ITO layers with 50 nm Pt filmdeposited on PS substrate after shrinking……...67
Figure 4.9 (a) Scheme of all-polymer DSSC with shrink induced structures on both anode and photocathode. Inset: SEM image of shrink induced micro pillar coated with $TiO_2$. (b) The current densities versus voltage characteristics of DSSCs with or without shrink induced structures. There is up to 59.3% ECE enhancement of DSSC with shrink induced micro/nanostructures compared with the control group with flat electrodes…...69
Figure 4.10 Schematic illustration of fabrication process of micro pillar array on shrink polymer substrate……...70
Figure 4.11 (a) Optical images of fabricated silicon mold. The diameter of micro pillar is about 30 μm. (b) Optical images of embossed pattern on PS substrate. (c) SEM image of micro pillar array on photoanodes after shrinking. The diameter of micro pillar is about 15μm. (d) SEM image of $TiO_2$ coated photoanodes with micro pillar array……..71
Figure 4.12 (a) Schematic illustration of fabrication processes of the flexible electrode with micro pillar arrays; (b) Unbending state of DSSC; (c) Bending state of DSSC. The all-polymer structure of DSSC presents very good flexibility……...72
Figure 4.13 (a) Optical microscopy image of pillar arrays on silicon mold (120 μm pitch, 30 μm diameter); (b) Patterns on shrink polymer before shrink (c) SEM images of Pillar arrays fabricated on PDMS (60 μm pitch, 10 μm diameter); (d) High magnitude SEM image of pillar; (e) Substrate is coated with $TiO_2$ by doctor blade method; (f) High magnitude SEM image of pillar coated with $TiO_2$……73
Figure 4.14 I-V curves of DSSCs with different densities of pillar arrays. The high density of pillar array electrode (60 μm pitch, 10 μm diameter) can enhance the ECE by 45.7% compared with no pillar array electrode. The ECE is rising along with the increasing of pillar array density. The density of pillar arrays can be simply controlled by adjusting the shrink temperature……74

Figure 4.15 Characterization of bending effects on DSSC. DSSC with 3D structure will keep better performance compared with no structure ones. The ECE only decreases 7.6% for DSSC with 3D structure, but 29% for the DSSC without 3Dstructure. The decreasing of ECE after bending was caused by the cracking of ITO layer, which were mentioned in several other literatures……..75
Figure 5.1 (a) Sketch of shrink lithography processes. The shrink lithography uses embossing molding method to pattern the shrink film, and thermally shrink the film as a shadow mask subsequently. Metal patterns are obtained by sputtering. SEM images of (b) mold and (c) 21 nm line. (d) AFM image of 21 nm line……..81
Figure 5.2 (a) Shift in line width versus embossing pressure for shrink lithography. Width of the lines raises with the increase of embossing press when the operating temperature is controlled at room temperature. (b) Line width versus shrink temperature under the condition of controlling the embossing press at 50 kN. Width of the metal lines decreased with the rising of the temperature.....82
Figure 5.3 SEM images of the grooves embossed by the mold with the increase of embossing press when the operating temperature is controlled at room temperature.....84
Figure 5.4 SEM images of the metal lines fabricated by shrink lithography from the same mold at different shrink temperatures.....84
Figure 5.5 (a) A load on the mold positioned onto the shrink film causes local plastic deformation below the tips around. (b) The recovery of shrink film will decrease the width of the patterns greatly.....84
Figure 5.6 Sketches of (a) unsuspended and (b) suspended graphene nanoribbon. (c) SEM images of suspended grapheme nanoribbon. (d) High magnitude SEM image of graphene nanoribbon. (e) The detection limit results of graphene nanoribbon based biosensor in both suspended and unsuspended situations. Conductance versus time data recorded after alternate delivery of the following concentrations of PSA: (1) PBS contains no PSA, (2) 0.1 pg/ml, (3) 1 pg/ml, (4) 10 pg/ml, (5) 1 ng/ml, (6) 1 μg/ml. inset: the illustration of PSA sensing mechanism, where the graphene nanoribbon is modified with PSA antibody receptors. PSA bonded specifically to receptors will produce a conductance change of the graphene nanoribbon……..87
Figure 5.7 (a) Schematic illustration of basic concept of movable type shrink lithography. Optical image of wafer scale pattern array (b) before shrink and (c) after shrink. Different patterns including (d) line with 20 nm width and (e) dot with 20 nm diameter were achieved on the same wafer substrate by simply using different sub-molds.....89
Figure 5.8 SEM image of different sub-molds including (a) line arrays and (b) dot arrays.....91
Figure 5.9 (a) Optical image of $SiO_2$/Si wafer substrate. (b) Frame fabricated by laser cutting machine was fixed on top of substrate. (c) Movable type sub-molds were assembled with the frame. (d) Optical image of individule sub-mold.....92
Figure 5.10. SEM images of nanopatterns generated by shrink lithography from the same mold were taken and demonstrated the inverse relationship between feature size of patterns and shrink temperature.....95
Figure 5.11 (a) The width of lines and the diameter change of dots fabricated by shrink lithography from the same mold were decreased with the rising of the shrink temperature.

(b) Thermo gravimetric analysis of hydrogel. The weight of sample after shrinking to the weight of sample before shrinking ratio decreases along with the increasing of shrink temperature. (c) Real time record of thermo gravimetric testing. $W_0$ is the initial weight. (d) The thickness of hydrogel can be tuned by adjusting the surface wetting ability of substrate.....96
Figure 5.12 The thickness of hydrogel can be tuned by adjusting the surface wetting ability of substrate. The step measurement of hydrogel film thickness on different substrate with different surface wetting abilities: (a) contact angle 2°, (b) contact angle 27° , (c) contact angle 85° .....97
Figure 5.13 (a) Optical image of large-scale shrunk hydrogel film with line array patterns. The black dash line area is the original hydrogel area before shrink. (b) SEM of line array patterns.....98
Figure 5.14 (a) Sketch of suspended graphene nanoribbon array based biosensor for PSA testing. The immunoreactions between PSA and anti-PSA result in the decrease of graphene nanoribbon array resistance. (b) SEM images of suspended graphene nanoribbon array. The width of the ribbon is about 50 nm. (c) The graphene nanoribbon biosensor was characterized by pH measurements. (d) Different concentrations of PSA solutions were introduced to both the suspended and unsuspended graphene nanoribbon biosensors. The suspended biosensors demonstrated better detection limit than the unsuspended biosensors.....99
Figure 5.15 Schematic illustration of synthesis of the shrink induced graphene composites. (a) LbL self-assembly of graphene nanoplatelets on the PO substrate. (b) The structure of the LbL self-assembled graphene layers. (c) Heat shrink of the PO substrate, and the tunable wrinkles were generated.....101
Figure 5.16 SEM images of graphene composites treated at different temperature: (a) 100°C; (b) 120°C; (c) 140°C. Left: the lower magnitude of SEM image; right: the larger magnitude of SEM image. The surface morphologies of the samples from various shrink temperature is obvious different. The density of the graphene nanowrinkles is increasing along with the increasing of the shrink temperature.....104
Figure 5.17 (a-e) 3D AFM images of the self-assembled graphene composites from various shrink temperature. The (f) surface roughness and (g) surface area of the graphene composites versus the shrink temperature curves demonstrate that the higher shrink temperature induces higher density of the nanowrinkles.....105
Figure 5.18 SEM images of uniaxial shrink graphene composites. During the shrink process, two edges of a PO shrink film were clamped by clips to ensure it could only shrink in one direction while the other one is fixed.....106
Figure 5.19 Chemical sensors based on the shrink induced graphene composites were fabricated. The original resistance versus the shrink temperature curve was investigated. .....107
Figure 5.20 Glucose detection was characterized on the chemical sensor based on the shrink induced graphene composites, presenting a detection limit down to 10 pM. The control group with nonshrink substrate was investigated, presenting worse detection limits compared with shrink substrate group. The shrink substrate will introduce low-cost nanowrinkles.....108

Figure 5.21 Contact angle of the graphene composites raised along with the increasing of the shrink temperature.....110
Figure 6.1 Schematic illustration of fabrication processes of the shrink induced three-dimensional structures for biosensor and DSSC……..116
Figure 6.2: (a) The all-polymer structure of DSSC presents very good flexibility. (b) Circuit connection between biosensor and solar cell. (c) All components were packaged to form a biosensor system……..117
Figure 6.3 Detection limits characterization of three types of biosensors. The biosensor fabricated with pillar array can achieve 1 pM detection limit, better than the flat substrate with only 10 pM. In order to get clearer readout, normalized resistance was introduced……119

# CHAPTER 1

# INTRODUCTION

## 1.1 Background and Motivation

A biosensor is a device detecting and transmiting a physiological or biochemical changes. Typically, it is an electronic transducer integrating biological components, and converts a biochemical signal into a quantified electrical response [1-3]. Research in biosensors started in 1980's, and has been growing very fast due to the high demands of health care industry developments. Successful biosensor technology has expanded the current market over $13 billion [4]. Low-cost, reliable, and small biosensors capable of quickly detecting various diseases can dramatically reduce the heavy loads of regular clinical diagnosis. Many fully developed biosensors are integral parts of disease control including diabetes, prostate cancer, [5-6] etc. Sensitive and specific biosensors have also played important roles in food safety and environment monitoring applications [7-8]. Especially, small, portable biosensors are more attractive to integrate with communication/information technologies for real time management.

Nowadays, the development of novel biosensors using nanomaterials provides promising approaches to offer high performance in resolution and detection limit. The nanomaterials such as nanoparticle [9], carbon nanotube (CNT) [10], and silicon nanowire [11], provide effective approaches for novel biosensors with better performance. However, the detection limit and response time still have much space to improve. A variety of methods demonstrate neither ultra-low detection limit nor very large detection ranges, including enzyme-linked immunosorbent assay (ELISA) and surface plasmon

resonance (SPR). Many of them are incredible expensive and complex to realize. New nanomaterials and new methods are badly needed to promote further development of biosensor researches. 2010 Nobel Laureate Andre Geim and Konstantin Novoselov have introduced graphene, a two-dimensional nanomaterial, to researchers. Investigation in graphene reveals that graphene is a promising nanomaterial for next generation of biosensors [12-14]. However, in order to achieve better performance and lower cost, new methods are required to propose. Especially, a novel patterning method with extremely low cost to pattern sub-100 nm feature-size patterns will benefit the development of nanomaterial based biosensors greatly, due to the high cost of fabrication processes.

Meanwhile, many types of biomedical equipments are built in very complex structures, and the power consumption is very high. Even for small portable and smaller biosensors, batteries are still required for the power supply. The disposal of batteries will add extra cost and environmental pollutions. Renewable energy development and energy harvesting are attracting interests as an alternative to other sources of energy such as fossil fuel and nuclear energy [15]. Photovoltaic (PV) devices converting light directly into electricity are a viable solution for energy these days. Nowadays, the silicon wafer-based technology has attained industrial maturity, but several other new emerging technologies based on thin-film solar cell [16], dye-sensitized solar cell (DSSC) [17], and organic materials solar cell [18] offer potential advantages including lower cost and acceptable energy conversion efficiency. Especially, DSSC is a very promising technique based on a semiconductive photoelectrochemical system. It has attracted more and more researchers' attention since Michael Grätzel developed the first high efficiency DSSC in

1991 [19]. The DSSC has a number of attractive features including: conventional roll-printing techniques compatible, transparent, flexible, and low-cost. Although its conversion efficiency is less than the silicon based solar cell, its potential efficiency has been estimated good enough to allow them to compete with fossil fuel electrical generation [20].

Therefore, it is desirable to further develop biosensor systems by integrating with innovative nanomaterials and structures toward better performance and lower costs. By employing the photovoltaic techniques, the nanomaterial based biosensors are capable of working without external energy sources, reducing the cost in a green strategy.

### 1.2 Objectives of Research

The main objective of thesis research is to develop nanomatrial based biosensors integrated with solar cell, which is aiming to achieve high performance in detection limit, sensitivity, stability, etc. Due to the unique structural, electrical, chemical, and mechanical properties of nanomaterials, the characteristic results of biosensors will demonstrate the advantages in the applications. With nanomaterials and improved fabrication processes, the cost of biosensors will be decreased dramatically. High efficiency DSSC will be integrated into the biosensor system for sensing without external sources. Different types of sensor structures and manufacture strategies are investigated based on the biosensor platform, considering various factors and conditions that affect sensing performance to optimize the biosensors and to find the best operating conditions for optimal sensing performance. Furthermore, more detailed analyses about biosensing characteristics as well as stability characteristics of the biosensors are implemented.

Shrink lithography, a low-cost patterning method, will be introduced into the fabrication processes of biosensors and DSSCs. Smaller feature-size structures will enhance the performance of both biosensors and DSSCs [21-22]. It is very important to achieve such nano scale patterns without introducing high cost technique. One of the most important research objectives is to develop the shrink lithography to generate low-cost nano-scale structures to power the nanomatrial based biosensor system a lot.

### 1.3 Methodology

The prevailing methods to detect biotargets include ELISA [23], SPR [24], micro cantilevers [25], etc. However, the proposed nanomatrial based biosensors are different from conventional approaches with better characteristic performance, unique fabrication processes and sensing mechanism. In the present study, self-assembly technique is used to fabricate the biosensors. Self-assembly process is a solution based nanofabrication approach for the transformation of molecules or protein into stable, well organized structures by electrostatic forces. Self-assembly process has the following benefits: it is cost effective, versatile, facile, and the process result is stable and robust. There are numerous mechanisms of self assembly including surface force, chemical self-assembly, biomolecule assisted self assembly, and electrostatic force, etc. Among all of the self assembly technique, Layer-by-Layer (LbL) self assembly is the most promising. As is shown in Fig. 1.1, by alternatively immersing substrate into different charged nanomaterial suspensions, various types of nanomaterials are capable of forming uniform thin films.

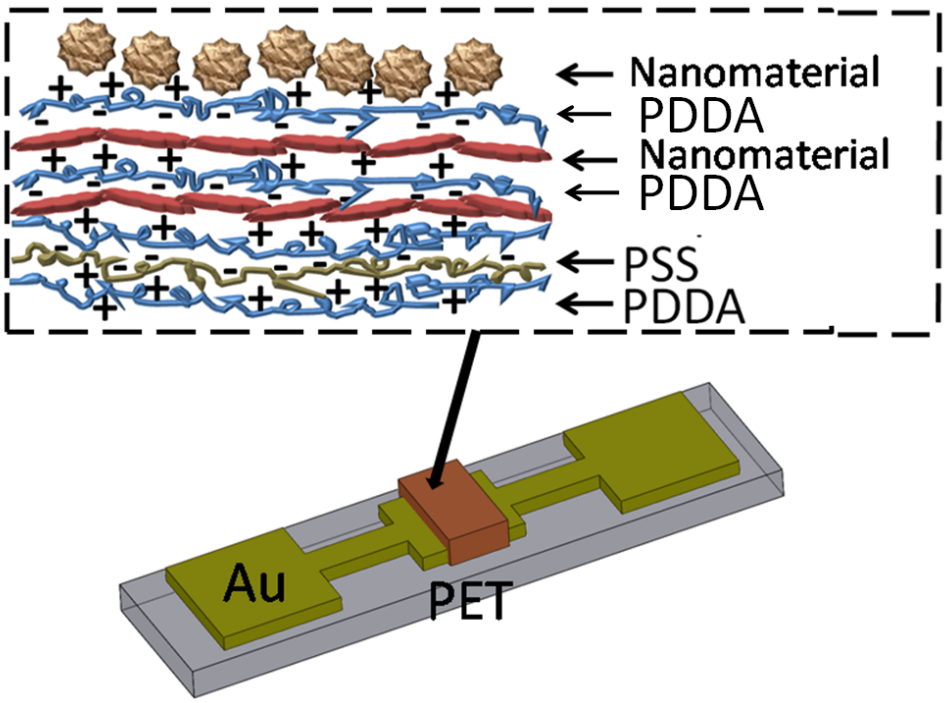


Figure 1.1: Typical structure of LbL self assembled biosensor.

Fig. 1.2 shows the basic ion sensitive field effect transistor (ISFET) structure of the nanomatrial based biosensor system and its sensing mechanism. Target solutions are introduced into the recording chamber, and an Ag/AgCl reference electrode is immersed in order to apply a desired gate voltage. The energy is supplied by photovoltaic devices based on photon active polymer. Given that the conductance of semiconductor nanomaterail is proportional to the product of charge carrier density and mobility, it is evident that changes in density and/or mobility of charge carriers must be responsive when molecules or ions are absorbed by sensing materials [26]. The equation $\sigma = nq\upsilon$ can show the relationship clearly, where $\sigma$ is conductance, $n$ is carrier density, $q$ is charge per carrier, and $\upsilon$ is the carrier mobility. By adjusting the gate voltage, different concentrations of biotargets will introduce different electrical responses of the ISFET

biosensors. DSSC will be integrated with the sensor, providing the power required from sensing process. In the following sections, the development progress and biosensing performance of different sensors are presented in details.

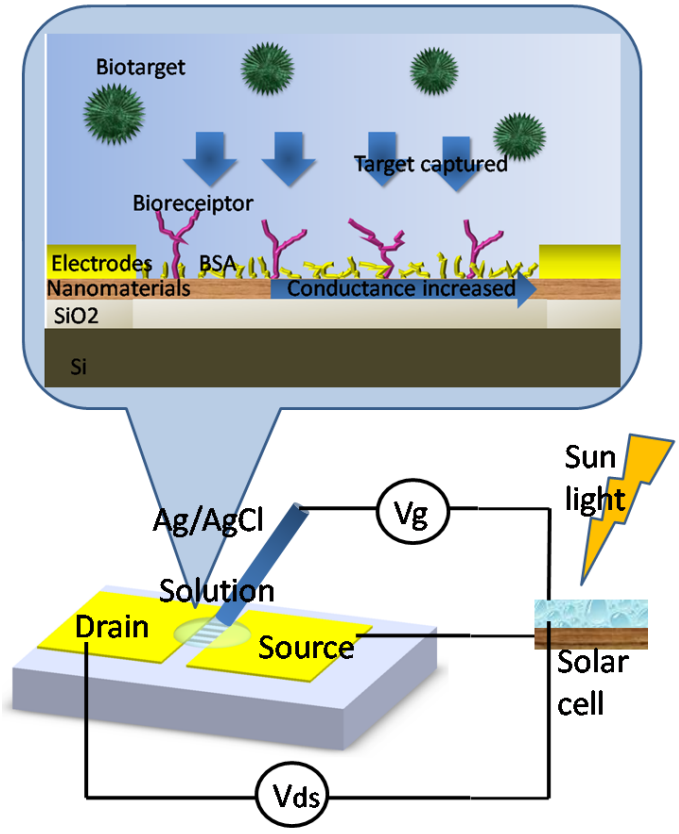


Figure 1.2: The ISFET structure of biosensor system and sensing principles.

Novel fabrication methods are used in the sensor and solar cell development processes. Nano-scale structures are introduced to enhance the performance of biosensor and solar cell in a low-cost way. Shrink lithography can generate sub-micrometer patterns by simply using the shrinkage properties of shape memory polymer such as polystyrene (PS) and polyolefin (PO). With hot embossing on shrink polymer, 22 nm patterns can be

fabricated in an extremely low-cost way compared with other conventional nanofabrication techniques such as E-beam lithography on nanoimprinting.

### 1.4 Thesis Overview

Graphene sensing layer synthesis methods used in this study are introduced in Chapter 2. Graphene preparation, characterization, and graphene based biosensor fabrication are discussed extensively. Chapter 3, the fundamental mechanisms of biotarget sensing in graphene based nano devices are discussed. Different biotargets including prostate specific antigen (PSA), glucose, vascular endothelial growth factor (VEGF) detection results are demonstrated by graphene based biosensors. Different structures of biosensors are also investigated. In Chapter 4, the theory and development processes of DSSC are presented. Flexible DSSC with high efficiency is also presented. With shrink induced nanostructures, better efficiency of DSSC discussed. Both principle and fabrication processes of the low-cost shrink lithography are discussed in Chapter 5. Several shrink lithography application cases are introduced. In Chapter 6, a nanomatrial based biosensor system powered by DSSC is presented. The testing results demonstrate the good performance of nanomatrial based biosensor system. Finally, in Chapter 7, the conclusions are summarized from biosensor and DSSC. Future works is suggested for the further development of nanomatrial based biosensors.

# CHAPTER 2

# FABRICATION OF GRAPHENE BASED BIOSENSORS

## 2.1 Introduction

Recently, graphene has attracted more and more attention due to its unique structural, electrical, chemical, and mechanical properties [27-30]. With rational physical and/or chemical modification, graphene is capable of detecting many types of molecules and ions, including pH [31], glucose [32], DNA [33]. Moreover, its inherently low electrical noise gives a very promising way to achieve very low detection limits [34]. Graphene's two dimensional nature structure means that all its atoms are exposed to the adsorbing gas molecules, providing the greatest sensor area per unit volume [35]. Besides, it has inherently low electrical noise due to the quality of its crystal lattice, and due to its two-dimensional nature, which tends to screen charge fluctuations more than one-dimensional systems such as carbon nanotubes [36]. In addition, graphene's charge carriers (electrons or holes) have zero rest mass and travel rapidly through its honeycomb lattice [37]. This high-mobility conduction makes graphene qualify for high-speed nano-scale electronics. Beyond its desirable electronic properties, graphene has practical advantages for making sensors, such as its amenability to making devices by conventional lithographic approaches and the good long-term stability of such devices [38]. However, current techniques used to produce graphene membranes are underdeveloped and generally not scalable. These techniques rely on low-yield, serial processes typically involving the transfer of optically identified exfoliated graphene or graphene grown on metal substrates [39] to a perforated substrate [40] such as a commercial transmission electron microscopy

(TEM) grid [41] or to a substrate for additional microfabrication processing (i.e., patterned metal deposition, etching, etc.). In any case, optical identification is a meticulous process, even for the trained eye, which together with the delicate nature of graphene transfer precludes the possibility of wafer scale fabrication.

In addition, to date, researches of graphene have been focused exclusively on graphene sensors supported on substrates [42], although charge traps at the interface and in the substrate have been shown to act as external scattering centers and degrade transport properties in single-layer graphene whose atoms are all exposed directly to fluctuations of extrinsic impurities [43]. The signal-to-noise ratios of suspended graphenenanodevices were improved in low frequency regime (below 1 kHz) for both hole and electron carriers compared with those supported on substrates owing to concomitantly increased transconductance and decreased noise level by suspended structure [44].

### 2.2 Different Fabrication Methods of Graphene and Graphene Composites

Graphene-based biosensors are proposed for sensitive and label-free detection of many types of biomarkers [45] with rational physical and/or chemical modification. Several graphene synthesis approaches were developed, including lithographic patterning[46], unzipping of carbon nanotubes [47], epitaxial growth on SiC or metals, chemical exfoliation of graphite oxide [48], and chemical vapour deposition (CVD) growth on metal substrates [49]. In order to extend the good properties of graphene to achieve specific applications, pure graphene sheets have been extensively integrated with other materials such as polymers and nanoparticles into various hybrid structures to enhance the performance of biosensors [50].

At present, some researchers have been dedicated to the construction of graphene nanocomposites with various strategies. Among different types of pure or hybridized graphene structures, there typical structures are the most popular. Pure graphene is believed to be the most direct and simple structure (i.e., single or several layers of graphene sheets generated by exfoliation method or CVD method), and has been successfully used to prepare pH and DNA biosensors [51-52]. The second type of structure is graphenenanoplatelets assembled composites (i.e., after synthesizing stable dispersion of graphenenanoplatelets solutions, the substrate was introduced for the assembly of graphenenanoplatelets without any other materials hybrid) [53]. Several biosensors were developed based on the graphene composites. The third type of structure is hybridized graphene composites (i.e., nanoparticles or polymer were hybridized with graphene platelets to synthesize hybrid structure) [54]. Numerous biosensors were derived from this type of graphene structure with enhanced performance and specific functions. As shown in Fig. 2.1, three types of graphene based composites from pure to hybrid were synthesized for the construction biosensors. Herein, the pure graphene was generated by mechanical exfoliation method developed by our group [55]. The assembled graphene composites were fabricated by microfluidic method without introducing other hybrid material. And the hybridized graphene composites were formed by self assembly technique. The performance of the three different types biosensors were investigated and compared.

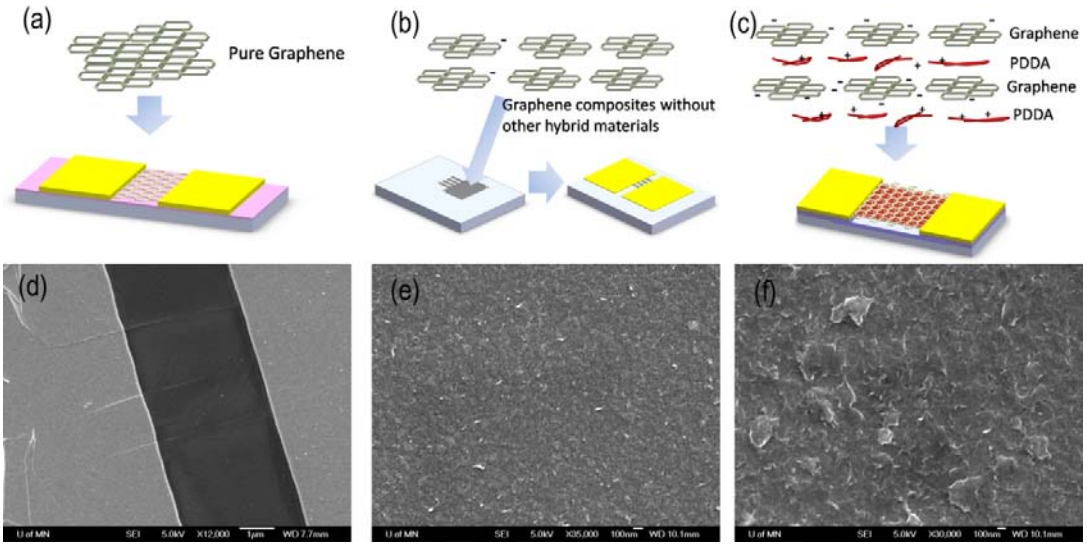


Figure2.1: Sketches of three different types of graphene based biosensors from pure to hybridized graphene composites: (a) mechanical exfoliation method derived graphene biosensor structures; (b) microfluidic method induced graphene composites without introducing other hybrid material; (c) self assembled graphene hybridized with polymer. (d-f) SEM images of surface profile of pure graphene, microfluidic induced graphene composites, and self assembled hybridized graphene composites, respectively.

### 2.2.1 Mechanical Exfoliation Derived Graphene Biosensor

To fabricate pure graphene biosensor, a photoresist layer (Shipley S1818) was used as a transfer stamp to exfoliate graphene patterns from highly oriented pyrolytic graphite (HOPG), and transferred patterns onto a $SiO_2$/Si substrate [55]. First, patterns in microscale were formed on the surface of HOPG (MikroMasch Inc., ZYA grade) by photolithography followed by an oxygen plasma etching with STS etcher (Model 320, 30 seconds). A layer of S1818 was spun on the pre-treated HOPG, and a thermal releasing

tape was used to gently peel graphene flakes off, and transferred them onto the $SiO_2$/Si substrate. After that, chromium/gold layers 50/200 nm thick were deposited on the substrate by an AJA sputter system (Model ATC 2000). After the patterning of metal layers at the two edges of graphene sheets, they play the roles of electrodes for the biosensors.

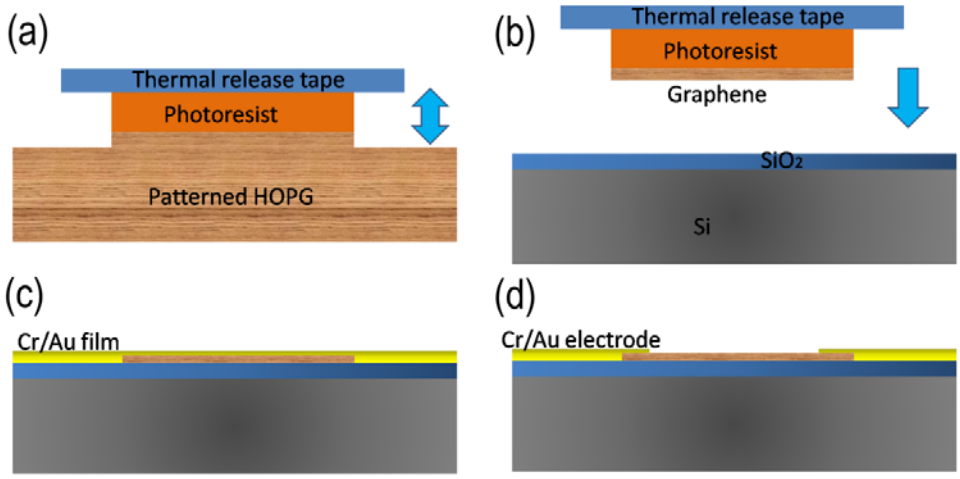


Figure 2.2: The fabrication processes of mechanical exfoliation graphene biosensors.

### 2.2.2 Microfluidic Induced Graphene Biosensor

The fabrication processes of microfluidic induced graphene films were illustrated in Fig. 2.3. Microfabrication was utilized to build the microchannels, and microfluidics was used to deposit the graphene films. First, a layer of photoresist (Shipley S1813) was spin coated on several cleaned silicon wafers with 300 nm thick silicon dioxide on surface, followed by a patterning of photoresist with photolithography. Subsequently, the patterned substrate was immersed into HF buffer solution (10:1) to obtain the microchannel array in the silicon dioxide layer. According to control the etching time,

different channel heights from 50 nm to 250 nm were generated. After striping of the photorisist, research grade graphene (PureSheets$^{TM}$, NanointegrisInc, 0.25 mg/ml) suspension solution were introduced into the reservoir. Due to the hydrophilic property of silicon dioxide, the capillarity induced the graphene suspension solution into the microchannel array. Next, the whole system was placed in avacuum oven (Model 280A) for 30 min to degas and dry up the solution at room temperature under vacuum condition. Then, the extra graphene films in the reservoir were gently scraped off by blade. Chromium/gold layers 10/100 nm thick were deposited at the two ends of the microchannels with an AJA sputter system (Model ATC 2000), and sensor electrodes were patterned by photolithograph with photoresist.

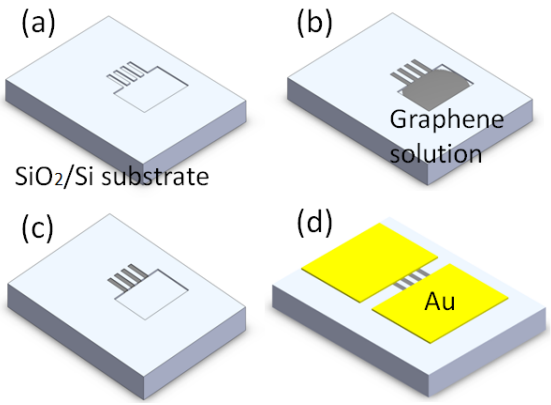


Figure 2.3:The fabrication processes of microfluidic induced graphene biosensors.

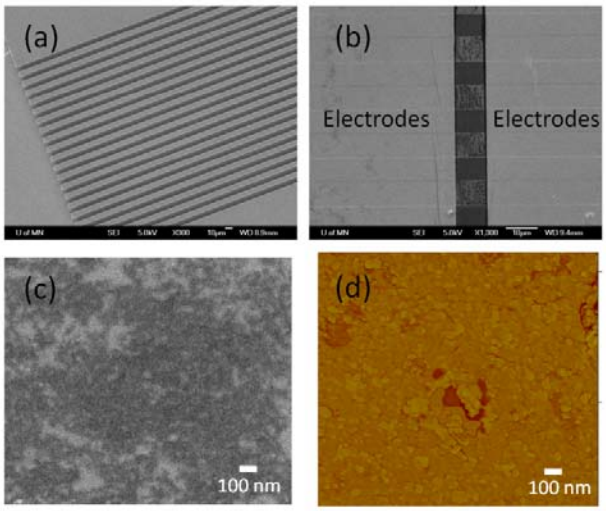


Figure 2.4: SEM images of (a) microchannel array, (b) sensor structure, and (c) porous surface profile of microfluidic induced graphene films. (d) AFM image of the graphenenanoplatelets deposited randomly across the channel of two electrodes.

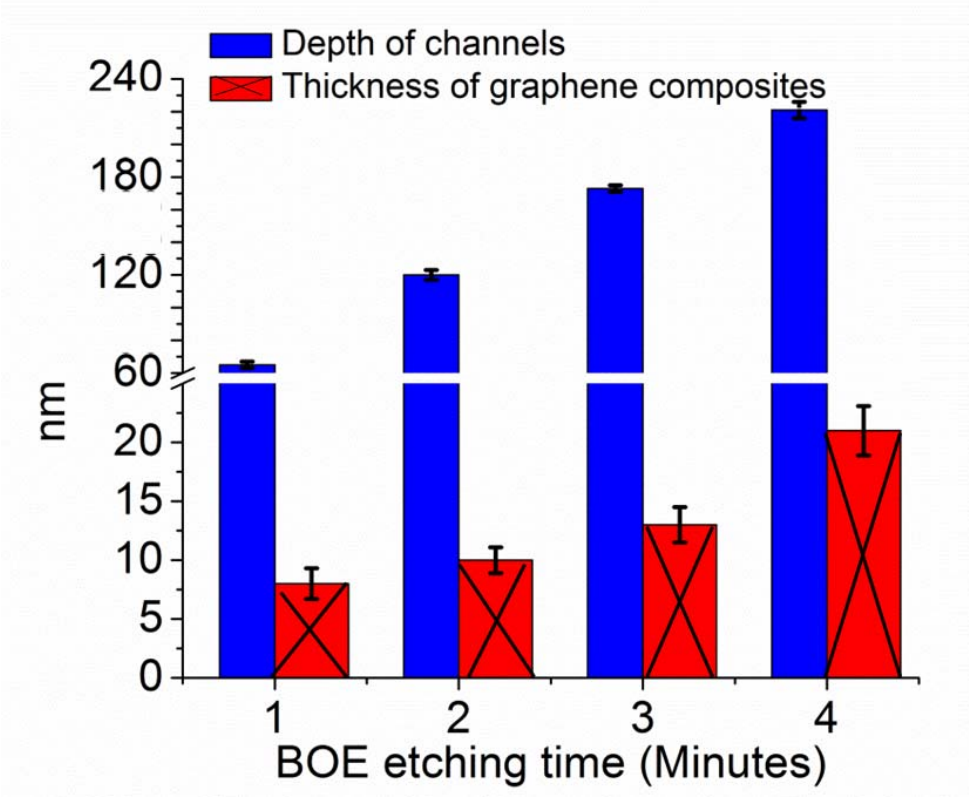

Figure 2.5: AFM was used to characterize the thickness of graphene films in different microchannels with various heights. The thickness of the graphene films were raising along with the increasing of the microchannel heights.

The microfluidic induced graphene films were also inspected by scanning electron microscope (SEM) and atomic force microscope (AFM). As is shown in Fig. 2.4, the microchannel array was fabricated in the silicon dioxide layer on a silicon substrate. Two electrodes were deposited on the microchannel to form the sensor structure, which is shown in Fig. 2.4b. Fig. 2.4c, d present the porous surface profile of microfluidic induced graphene, and the graphene nanoplatelets were deposited randomly across the channel of two electrodes. In addition, AFM was also used to characterize the thickness of graphene films in different microchannels with various heights. To control the etching time of silicon dioxide in HF buffer solution, the heights of microchannels were obtained from 65 nm to 221 nm. After degasing and drying up in vacuum oven, the thickness of the deposited graphene films were measured in the microchannels with different heights. As is shown in Fig. 2.5, the thickness of the graphene films were rising along with the increasing of the microchannel heights. This can be explained that different amounts of graphene suspension solution were introduced by capillarity and various channel heights. As a result, the thickness of the graphene films is capable of controlly tuning by adjusting the height of microchannel.

### 2.2.3 Self-Assembled Graphene Biosensor

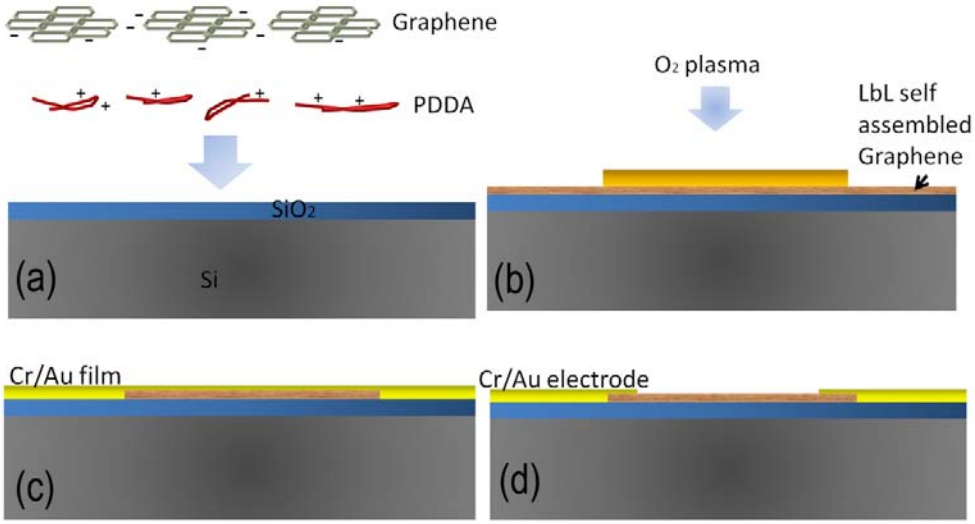


Figure 2.6: The fabrication processes of self-assembled graphene biosensors.

The sensor reported herein was fabricated on a silicon substrate with a layer of $SiO_2$ on the surface. The polyelectrolytes used in this study were poly(diallyldiamine chloride) (PDDA) and poly(styrene sulfonate) (PSS), purchased from Sigma–Aldrich Inc. The concentrations of aqueous PDDA and PSS were 1.5 and 0.3 wt% respectively, with an addition of 0.5 M sodium chloride to enhance the surface properties. Research grade graphene (PureSheets$^{TM}$, 0.25 mg/ml) was purchased from Nanointegris Inc. The silicon wafer was immersed into the charged suspensions with a sequence of [PDDA (10 min) + PSS (10 min)]$_2$ + [PDDA (10 min) + graphene suspension (20 min)]$_5$. Another lithographic step was used to fabricate a sensing area on self-assembled graphene film, with the assistance of oxygen plasma etching. Chromium/gold layers 50/200 nm thick were deposited on the substrate with an AJA sputter system (Model ATC 2000). Subsequently, sensor electrodes were patterned by photolithograph. The thickness and

resistance of 5 bilayers of self assembledgraphene film were 45 ± 5 nm and 0.9 ± 0.01 kΩ, characterized by surface profiler P16 and Agilent data logger (34970A, Agilent Inc.) respectively. As shown in Fig. 2.7, the self-assembled graphene were inspected by SEM and AFM, presenting the defoliation of surface profile.

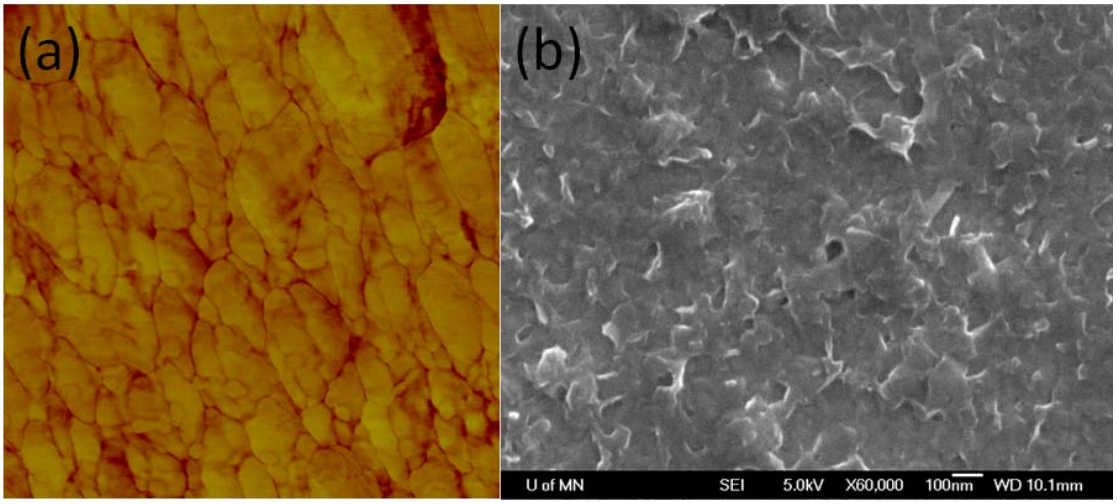


Figure 2.7: (a) AFM image of LbL self assembled graphene (scanning area is 1 μm by 1 μm). (b) SEM image of LbL self assembled graphene displaying its porous defoliation surface profile. The average graphene nanoplatelet is about 100 nm by 100 nm.

## 2.3 Special Structure Biosensors

### 2.3.1 Low-Cost Flexible Biosensor

These days, biosensors are required to be lower-cost to decrease the heavy load of medical care. Flexible biosensor will also benefit people a lot, making the sensor adaptable to wearable devices and implanted devices. Therefore, low-cost and flexible biosensor is great for sensor development. Herein, a polyethylene terephthalate (PET)

wafer substrate was used to replace the silicon wafer substrate to form the low-cost flexible biosensors. As shown in Fig.2.8, using self-assembly of graphene on PET, a low-cost and flexible biosensor was synthesized. Based on the self-assembly technique and the PET substrate, the manufacture of graphene biosensors is much easier, and fully compatible with the standard microelectronic fabrication processes.

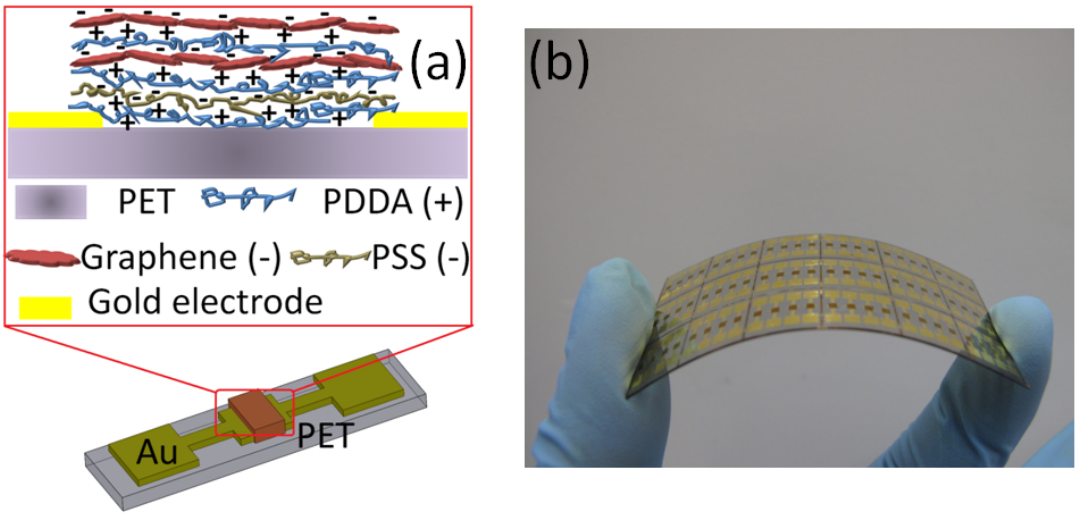


Figure 2.8: (a) Schematic illustration of self-assembled graphene nanocomposite before immunization. (b) Optical image of self-assembled graphenesensor on a flexible PET substrate.

### 2.3.2 Suspended Graphene Biosensor

To date, research on graphene has been focused exclusively on graphene sensors anchored on substrates. Any uncontrolled and random perturbations at the interface and on the substrate would lead to significant device current fluctuations and contribute to the electrical flicker noise known as low-frequency 1/f noise, which will attenuate the

sensitivity, especially in the extremely low concentration situations [56].The detection limit of a sensor that can be processed is ultimately determined by its signal-to-noise ratio. If the input signal and sensor structure are constant, the output signal is supposed to be more stable and sensitive due to the lower 1/f noise. The signal to noise ratio must be improved because the electrical flicker noise is ubiquitous in solid state electronic devices. Therefore, a suspended self-assembled graphene biosensor was proposed to decrease the 1/f noise.

Microfabrication was utilized to build the structure, and self-assembly method was used to deposit the graphene. First, graphenenanocomposite layers were self assembled on a clean silicon wafer with $SiO_2$ 300 nm thick. The substrate was immersed into the charged suspensions with a sequence of [PDDA (10 min) + PSS (10 min)]$_2$ + [PDDA (10 min) + graphene suspension (20 min)]$_5$. Subsequently, the self-assembled graphene was patterned to ribbons by oxygen plasma etching with STS etcher (Model 320, 30 seconds). Next, chromium/gold layers 50/200 nm thick were deposited on the substrate by an AJA sputter system (Model ATC 2000). After the patterning of metal layers at the two ends of graphene ribbons, they play the roles of clamps and electrodes for the biosensors. Then, the unsuspended graphene biosensors were fabricated. In order to obtain suspended grapheme biosensors, the $SiO_2$ layer 300 nm thick underneath graphene ribbons was etched away by buffered HF (BOE 10:1) for 5 minutes. Finally, the self assembled graphene was released by $SF_6$ dry etching of the silicon underneath with STS etcher (Model 320, 10 minutes). According to the dry etching rate and the etching time, the gap under the graphene layer was about 10 μm.

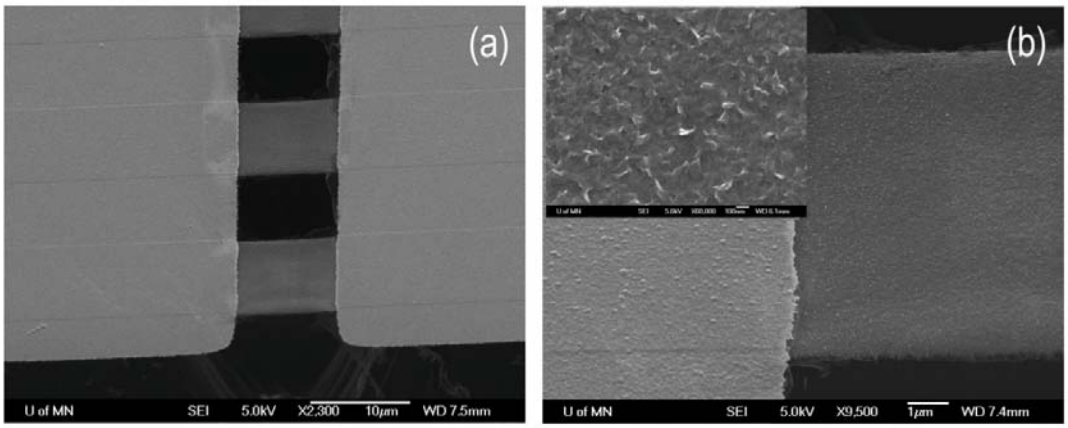


Figure 2.9: (a) 45 ° tilted SEM image of the suspended graphene beam array. The channel length is 10 μm, and the width of the graphene beam is 10 μm. (b) Anchor part of the beam demenstrates the well fixed ends of the graphene beam. Inset: high magnitude of SEM image of LbL self assembled graphene displays its porous defoliation surface profile details. The average graphene nanoplatelet is about 100 nm by 100 nm.

The noise spectra of suspended and unsuspended graphene devices were further investigated under the same experimental conditions, and concentrated on low-frequency (below 1 kHz) noise reported to be dominant in limiting performance of nanodevices[57]. The current power spectra can be expressed as

$$S_I = AI^2 f^{\beta},$$

where $S_I$ is the noise power density, $I$ is current, $f$ is the frequency, $A$ is defined as the 1/f noise amplitude, and $\beta$ is the frequency exponent with a value close to -1[57]. Fig. 2.10 shows the noise power spectrum $S_I$, normalized by the mean square of current, for both suspended and unsuspended graphene biosensors as a function of frequency. The noise level of the self assembled graphene devices are decreased by one order of magnitude

from the unsuspended state to the suspended state. It was reported that trapped charges at the interface and in the substrate degrade transport characteristics of a single-layer graphene[57], which exhibits the effect in our experiment results. In addition, due to the self assembly technique and polymers, the surface profile of the graphene layers shows great porous topography, more suitable to decorate capture proteins, providing the greatest sensing surface area per unit volume. Moreover, the suspended structure exposing to both sides of the graphene layers doubles the sensing area comparing with the similar pattern in an unsuspended structure, which is helpful to enhance the output signal.

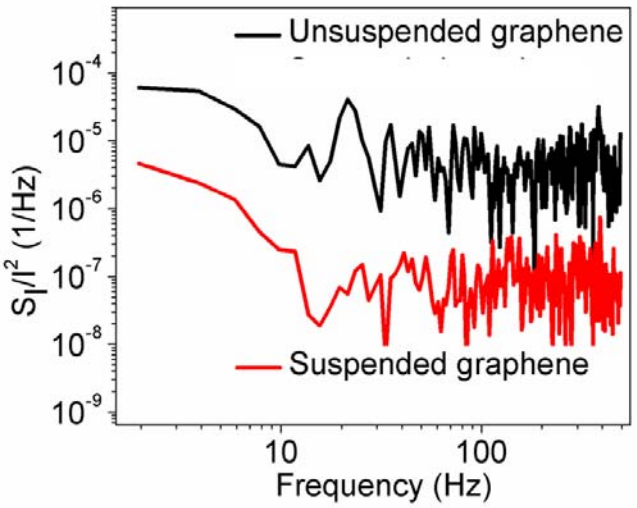


Fig. 2.10: Normalized noise power spectrum of the graphene biosensor was characterized. Comparison of graphene's noise power spectra with and without suspension situation shows lower level of 1/f noise in suspended devices.

## 2.4 Conclusion

The general farication background information on graphene and graphene composits has been discussed in this chapter. There different types of graphene and graphene composits preparison processes were presented.The pure graphene was generated by mechanical exfoliation method developed by Dr. Peng Li. The assembled graphene composites were fabricated by microfluidic method without introducing other hybrid material. And the hybridized graphene composites were formed by self assembly technique. The performance of the three different types biosensors were investigated and compared. The manufacture processes of biosensors were also introduced here, including flexible biosensor and suspended graphene sensors.

# CHAPTER 3

# VARIOUS BIOTARGETS DETECTION OF GRAPHENE BIOSENSORS

## 3.1 Introduction

Nowadays, the developments of biosensors using nanomaterials provide promising approaches to offer high performance in resolution and detection limits. The nanomaterials such as nanoparticle [58], carbon nanotube (CNT) [59], and silicon nanowire [60], give effective approaches for novel biosensors with better performance. But the detection limits, sensitivity and response time still have much space to improve. A variety of methods demonstrate neither ultra-low detection limits nor very large detection ranges, and many of them are incredible expensive and complex to realize. On the other hand, due to the increasing need from new therapeutics that target different mechanisms of action and methods for earlier diagnosis, new high performance of biosensors are required to increase understanding of disease processes and progression [61]. Particularly, the clinical utility of immunoreactions to discriminate health and disease states requires the capability to measure extremely low concentration proteins, which is also important to understand cellular processes and to search for new therapies [62].

To satisfy the requirements from biomedical and biosensing applications, graphene is proposed as sensing material to achieve better performance biosensors with low cost because of its outstanding electronic properties. Given that the conductance of graphene is proportional to the product of charge carrier density and mobility, it is evident that changes in density and/or mobility of charge carriers must be responsive when molecules

or ions are absorbed by graphene [63]. Herein, it is a good opportunity for graphene to act as sensing material due to its conductance shifts. However, it is still not efficient to achieve the best performance of graphene sensors. Many of the predicted properties arising from the two-dimensional nature of graphene [63] can be obscured or altered by perturbations caused by an interaction with an underlying substrate. For example, any uncontrolled and random perturbations from the substrates would lead to significant current fluctuations and contribute to low-frequency 1/f noise in graphene, which will determine and limit the detection limits of graphene based sensors, especially in the extremely low concentration situations [64].

In addition, current techniques used to produce suspended graphene membranes are under developed and generally not scalable. These techniques rely on low-yield, serial processes typically involving the transfer of optically identified exfoliated graphene1 or graphene grown on metal substrates [65] to produce a suspended membrane. In any case, optical identification is a meticulous process, even for the trained eye, which together with the delicate nature of graphene transfer precludes the possibility of wafer scale fabrication. In order to fabricate low cost and high yield suspended graphene structure for investigate, self-assembled graphene is an optional direction. Due to its simplicity and versatility, self-assembly technique allows thin films of graphene, nanoparticle, or protein to deposit on the structure on nanometer scale [66]. The self-assembled graphene nanosheets are suspended between two micro-patterned electrodes, acting as a platform of a new detection protocol which can be extended for critical applications to clinical diagnosis, food toxin detection, and environment monitoring.

### 3.2 Sensing Mechanism Discussion

#### 3.2.1 Surface Modification

After the graphene sensor structure finished, the bio-receptors should be immobilized on the surface of sensing area. There are generally two types of surface modification processes, including label free modification and labeled modification. Herein, prostate specific antigen (PSA) biosensor will be used as an example to demonstrate the processes of surface modification.

To manufacture label free PSA biosensors, a graphene sensor was first immersed into 0.1% PLL (poly-l-lysine, Sigma–Aldrich Inc.) aqueous solution for 1 hour, followed by drying with a nitrogen stream. Next, the graphene sensor was incubated for overnight at 4 ºC in PSA capture antibody solution (BioCheck Inc.) at a concentration of 10 μg/ml, prepared by a dilution into PBS (Dulbecco's phosphate buffered saline, Invitrogen Inc.). The sensor was rinsed with a PBS solution 3 times using a shaker (100 rpm, 19 mm circle) for 10 minutes each time. Next, the sensor was incubated in 3% bovine serum albumin (BSA, Sigma–Aldrich Inc.) blocking solution at room temperature for 5 hours to block nonspecific binding sites. After repeating the rinsing step, the label free sensor was ready for testing.

To manufacture horseradish peroxidase (HRP) labeled PSA biosensors, a graphene sensor was first immersed into 0.1% PLLaqueous solution for 1 hour, followed by drying with a nitrogen stream. Next, the graphene sensor was incubated for overnight at 4 ºC in PSA capture antibody solution at a concentration of 10 μg/ml, prepared by a dilution into PBS. The sensor was rinsed with a PBS solution 3 times using a shaker (100 rpm, 19 mm

circle) for 10 minutes each time. Next, the sensor was incubated in 3% BSA blocking solution at room temperature for 5 hours to block nonspecific binding sites.Subsequently, the graphene biosensors were incubated in various concentrations of PSA (EMD Chemicals Inc.) for 1 hour. Finally, After PSA sensors were incubated in HRP conjugated PSA secondary antibodies (255 ng/ml, BioCheck Inc.) for 1 hour, the labeled sensors were also ready for testing.

### 3.2.2 Detection Method

In label free state (Fig. 3.1a), the conductance of the graphene based biosensor modified with the PSA capture antibody shifts as the concentration change of PSA solutions. In the labeled state (Fig. 3.1b), the HRP conjugated with PSA antibody catalyzes a biochemical reaction by the mixture of ascorbic acid and hydrogen peroxide. The conductance of the graphene biosensor varies as the local pH shifts [67]. After LbL self assembly of graphene, the PSA capture antibody was modified onto the graphene, and the sensor was blocked withBSA. Different concentrations of PSA diluted in PBS were introduced onto the label free graphene sensor, and the conductance shift was monitored by the Agilent data logger.

Furthermore, the labeled cancer sensor was also tested to compare with label free one. After the HRP labeled immunization processes were executed, a mixture of 1 mM ascorbic acid (Sigma-Aldrich Inc.) and 1 mM o-phenylenediamine (Sigma-Aldrich Inc.) was produced with a dilution to PBS solution (1 mM Na-phosphate buffer, pH 6.0, with 15 mM NaCl). The role of o-phenylenediamine was to expedite the HRP catalyzed reactions. The conductance of graphene biosensor changes due to the local pH shift

caused by the conversion of ascorbic acid into dehydroascorbic acid during the enzymatically catalyzed reduction [67].

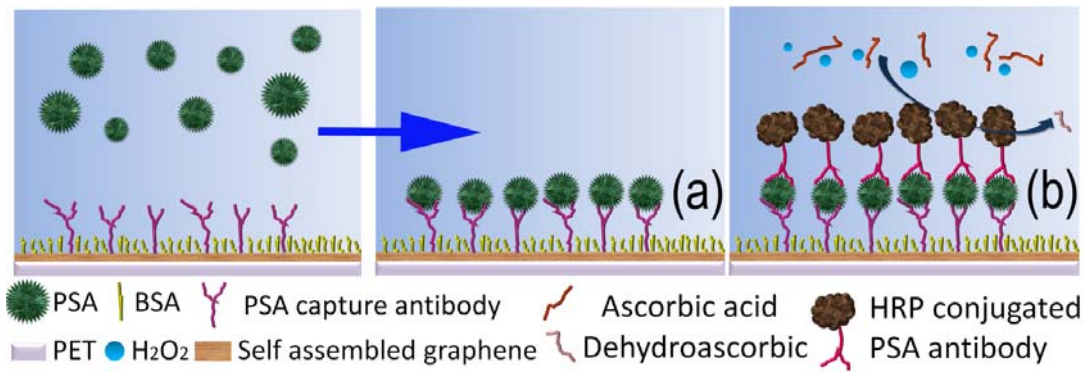


Figure 3.1 (a) Schematic illustration of interaction between capture antibodies and target protein molecules in a label free detection. After graphene biosensor modified by capture antibodies encounters PSA solution, the immunoreation will take place, and the conductance of graphene changes. (b) Schematic illustration of a graphene sensor in a labeled detection. HRP labels the different concentration of PSA, and catalyzes the convertion from ascorbic acid to dehydroascorbic acid, causing the local pH shifts. The conductance of graphene is sensitive to pH shifts.

### 3.2.3 Sensing Mechanism

In the work here, enzymes orantibodies will be immobilized on the substrate to trigger the biochemical reaction, causing the resistance change of biosensing materials. A physical and mathmaticl model should be proposed to analyze the activities of bioreceiptors.

Enzyme, the specialized proteins that catalyze biochemical reactions, are very important in the detection process of biosensors. In biochemistry and biosensing, Michaelis–Menten

kinetics is one of the simplest and best-known models of enzyme kinetics [68].Although Michaelis-Menten kinetics only works well when the concentrationof enzyme is less than that of substrates, it is a great model to understand enzymes' behaviors.

The basic chemical reaction equation can be represented schematically as:

$$E + S \underset{k_r}{\overset{k_f}{\rightleftarrows}} ES \xrightarrow{k_{cat}} E + P$$

where *E* is the enzyme, *S* is the substrate, *P* is the biochemical reaction product, and *ES* is enzyme-substratecomplex. $k_f$, $k_r$and $k_{cat}$ are the rate constants. The double arrows between *S* and *ES* represent the fact that enzyme-substrate binding is areversible process.

The Michaelis-Menten constant can be defined as follows:

$$k_m = \frac{k_r + k_{cat}}{k_f}$$

The rate of products is:

$$v = \frac{d[P]}{dt} = \frac{V_{\max}[S]}{k_m + [S]}$$

Where $V_{max}$ is the maximum velocity at which the reaction becomes saturated.

Uasually, antibodies will act as bio-receiptors to capture certain molecules or proteins acoording to special chemical group bonding. In this way, antibodies are very selective, only responding to matched antigens.

The equation,

$$\sigma = nqv$$

can show the resistance change clearly, where σ is conductance, n is carrier density, q is charge per carrier, and $v$ is the carrier mobility. When antibodies captured antigens,

which are usually charged, the graphene conductance will be changed by the changed surface charge [67].

### 3.3 Different Biotargets Detection

#### 3.3.1 Glucose Detection

The glucose sensors are in the forefront of recent advances in biosensors due to the high demand of diabetes diagnosis and the necessity of the monitoring glucose level in the fermentation process in the food industry [69]. Many research efforts have been made to develop new methods and technologies to improve glucose monitoring in the cheap, accurate, and easy-to-use method.

The sensors were verified for functionality and detect limitation of glucose sensing. After the experimental set up, 200 μL glucose solution was added to the sensing region. The self assembled glucose oxidaze (GOx) on the surface of sensors reacted with the glucose and created hydrogen ions as such:

$$\beta - D - \text{glucose} + O_2 \xrightarrow{GOx} D - \text{glucono} - \delta - \text{lactone} + H_2O_2$$

$$D - \text{glucono} - \delta - \text{lactone} + H_2O \rightarrow D - \text{gluconate}^- + H^+$$

Biocatalyzed hydrolysis of glucose in the presence of GOx resulted in the changes of local pH, and can be detected by the graphene which was reported as high sensitivity material on pH detecting [70].

As shown in Fig. 3.2a, the hydrogen ions from this chemical reaction increases the conductivity of the semi-conductive chip and the current will also increase accordingly. The tested current increases with the concentration of glucose solution increasing. After the biochemical reaction, the sufficient hydrogen ions are absorbed by LBL self

assembled graphene. This chemical doping process is able to increase the carrier density of graphene [71].

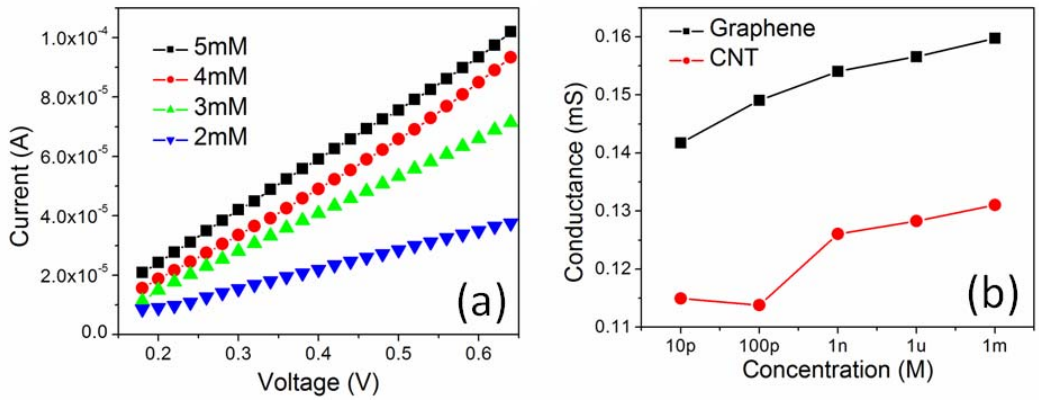


Figure 3.2 (a) different concentrations of glucose solution testing results; (b) resolutions of graphene and CNT comparison, graphene based glucose sensor can get 10 pM resolution which is higher than CNT as only 100 pM.

As shown in Fig. 3.2b, the detection limits of graphene and CNT sensor were measured, screening graphene better detecting ability. For graphene based sensor, it can detect as low as 10 pM glucose while CNT based sensor can only get 100 pM. Because of the unique lattice structure of graphene, the 1/f noise which is ubiquitous and dominates the signal-to-noise performance in nanodevices is strongly suppressed in graphene devices comparing with CNT or other nanomaterials.

### 3.3.2 Multiple Ion Detection

Homeostatic regulation of ions, such as sodium, potassium, calcium, and hydrogen, is very critical for most cellular functions, especially for the stability of a human body system. Imbalance of these ions in a human body may cause diseases including heart

failure ($Na^+$, $K^+$, $Ca^{2+}$), hypertension ($Na^+$, $K^+$), kidney disease ($Na^+$, $Ca^{2+}$), etc. Therefore, testing and monitoring concentration of these ions in a human body play a very significant role in an early diagnose and control of relevant diseases. However, the prevailing methods for ion sensitive sensing such as ion sensitive electrodes [72] and radio isotopic tracer [73] suffer from a low selectivity of sensing multiple ions or very long response time, and most of them are expensive and complex. To overcome the hurdles of these previous ion sensitive sensing methods, the LbL self assembled graphene is introduced to the ion sensitive sensing applications. The ion sensitive sensor array (ISSA) based on LbLself assembled graphene provides a promising way to selectively sense different ions simultaneously with a very short response time and a very high detection resolution due to its ultra high electron mobility and chemical sensitivity.

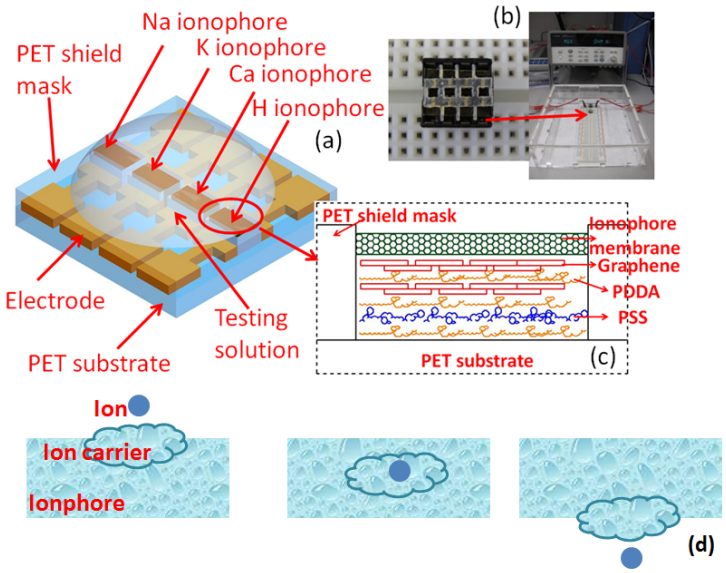


Figure 3.3 (a) Schematic of an ISSA: when testing solution contains only one type of ion, only the matched ionophore sensing channel triggers a signal; (b) Pictures of ISSA and

measurement system; (c) Structure of ISSA sensing region; (d) Ionphore working mechanism.

In order to investigate the selectivity of the ISSA, the testing solution containing one type of ions was applied to the ISSA, and the conductance of channels coated with different ionophores were recorded. Ionophore is usually synthesized by microorganisms to transport ions across the bilayer of the membrane. Chemical compounds (mobile ion carriers) that bind to a particular ion, shielding its charge from the surrounding environment, and thus facilitating its crossing of the hydrophobic interior of the lipid membrane. As is shown in Fig. 3.4, the LbL self assembled graphene conductance increases when absorbing these penetrating ions. Different sensing ionophore channels had the corresponding signals representing the ion concentrations in the testing solution.

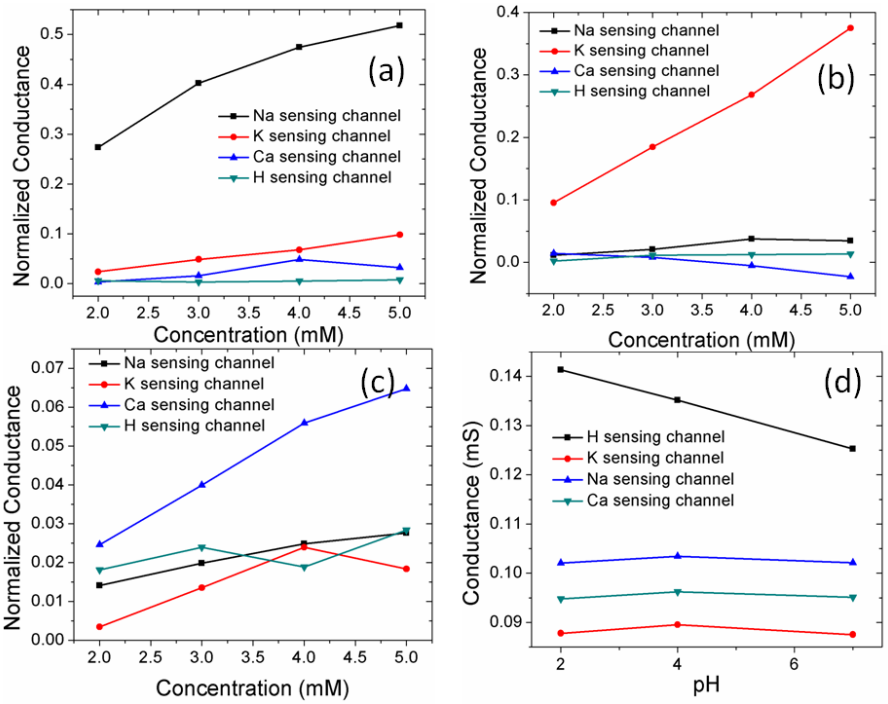

Figure 3.4: Testing solution contains only (a) NaCl; (b) KCl; (c) $CaCl_2$; (d) HCl. In order to get clearer readout, normalized conductance was introduced. Conductance under the condition of 1 mM concentration was used as initial conductance $G_0$ , and other conductance tested under different concentrations subtracted $G_0$to get ΔG. Normalized conductance represented as $\Delta G/G_0$

### 3.3.3 Acetylcholine (ACh) Detection

ACh is one of the most important chemical neurotransmitters involving both the peripheral nervous system and central nervous system in human body, which is considered to play a critical role in many human nervous activities including learning, attention, memory, and muscle contraction. An abnormally low concentration of acetylcholine is associated with Alzheimer's disease, which ranks the fourth in the causes of death among adults. Besides, the deficiency of ACh in the brain is possible to cause a number of neuropsychiatric disorders such as Parkinson disease and myasthenia gravis [74]. Therefore, it is important and of great increasing interest in the development of accurate sensing methods to measure ACh concentration.

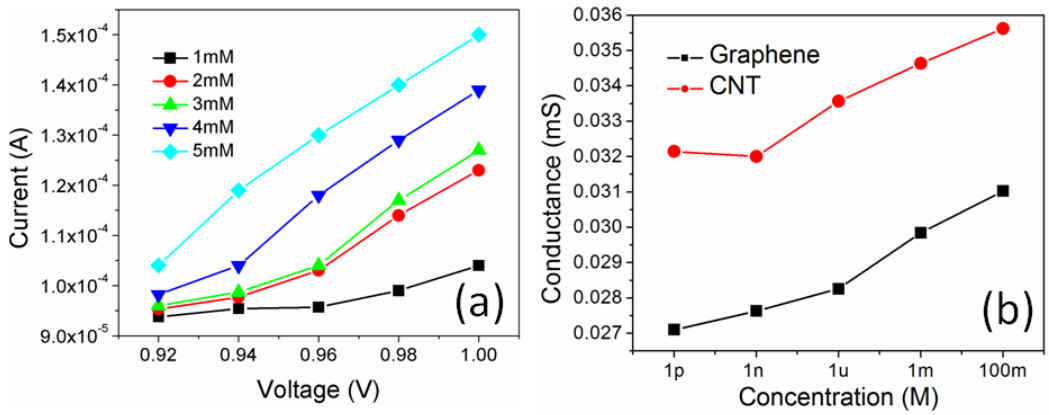

Fig. 3.5 (a) different concentrations of ACh solution testing results; (b) resolutions of graphene and CNT comparison, graphene based ACh sensor can get 1 pM resolution which is far higher than CNT as only 1 nM.

The graphene sensors were verified for functionality and detect limitation of ACh sensing. After the sensor set up, 200 μLAChsolution was added to the sensing region. The self assembledAChE on the surface of sensors reacted with the ACh and created brand-new compounds as such:

$$(CH_3)_3N^+CH_2CH_2OCOCH_3 + H_2O \xrightarrow{AChE} (CH_3)_3N^+CH_2CH_2OH + HOCOCH_3$$

Biocatalyzed hydrolysis of ACh in the presence of AChE resulted in acetic acid that changes the pH of the solution, and can be detected by the graphene which was reported as high sensitivity material on pH detecting [75]. As shown in Fig. 3.5a, the product of this reaction increases the conductivity of the semi-conductive chip and the current will also increase accordingly. The tested current increases with the concentration of ACh solution increasing. As shown in Fig. 3.5b, the detect limitations of graphene and CNT is measured, presenting graphene better detecting ability. For graphene based sensor, it can detect as low as 1 pM ACh which is three orders of magnitude higher than CNT based sensor tested as 1 nM. Because of the unique lattice structure of graphene, 1/f noise, ubiquitous and dominates the signal-to-noise performance in nanodevices, is strongly suppressed in graphene devices comparing with CNT or other nanomaterials.

### 3.3.4 PSA Detection

Cancer marker has been elucidated as a powerful medical tool in disease prediction, diagnosis, and monitoring [76]. Clinical utility of protein biomarker to discriminate

health and disease requires the capability of measurement of extremely low concentration proteins [77]. The prevailing methods for detection of cancer marker include the enzyme linked immunosorbent assay (ELISA) [78], surface plasmon resonance (SPR) [79], microcantilevers [80], etc. Especially, nano materials, such as nanoparticle, carbon nanotube, and silicon nanowire, provide effective approaches fornovel biosensors with better performance. However, a variety of methods demonstrate neither ultra-low detection limits nor very large detection ranges, and many of them are incredible expensive and complex to realize. Therefore, using self assembly of graphene, a flexible, low-cost, and label free cancer marker biosensor was synthesized for a real-time detection of PSA in a large detection range from 4 fg/ml to 4 μg/ml.

In label free state, the conductance of the graphene based biosensor modified with the PSA capture antibody shifts as the concentration change of PSA solutions. In the labeled state, the HRP conjugated with PSA antibody catalyzes a biochemical reaction by the mixture of ascorbic acid and hydrogen peroxide. The conductance of the graphene biosensor varies as the local pH shifts.

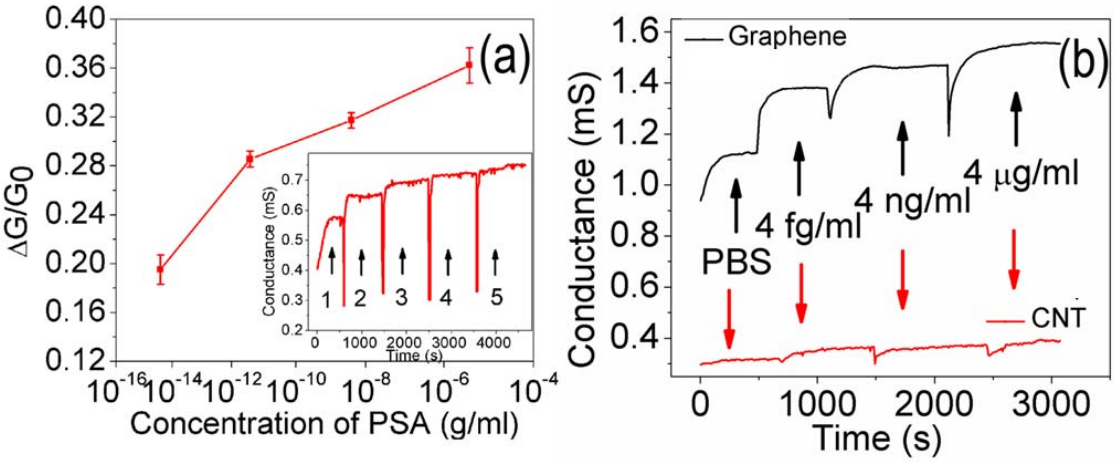

Figure 3.6 (a) Shift in conductance versus concentration of PSA for label free graphene sensor. Inset: conductance versus time data recorded after alternate delivery of the following concentrations of PSA: (1) PBS contains no PSA, (2) 4 fg/ml, (3) 4 pg/ml, (4) 4 ng/ml, (5) 4 μg/ml. Initial conductance $G_0$ represents the graphene conductance in PBS solution, and other conductance tested under different PSA concentrations subtracte $G_0$ to get $\Delta G$. (b) Conductance versus time testing was taken place between graphene and CNT biosensors after different concentrations of PSA were delivered. The results show that the detection limit of graphene sensor is down to 4 fg/ml, much better than CNT sensor with a detection limit of only 4 ng/ml.

The label free cancer sensor was characterized by measuring different concentrations of PSA solutions prepared by PBS. After LbLself assembly of graphene, the PSA capture antibody was modified onto the graphene layers, and the sensor was blocked with BSA. As shown in Fig 3.6a, the normalized conductance of graphene raises with the increase of PSA concentration from 4 fg/ml to 4 μg/ml. The conductance-versus-time measurements recorded on the graphene biosensor further confirms the trend in real-time detection. The CNT based sensor manufactured under the same conditions was conducted to compare with graphene sensor on the detection limits. Real time results (Fig. 3.6b) indicate that the CNT based sensor is only capable of detecting 4 ng/ml PSA, much worse than graphene sensor.

Furthermore, the labeled cancer sensor was also tested, and compared with label free one. As shown in Fig. 3.7a, the normalized conductance of graphene raises with the increase of PSA concentration from 0.4 pg/ml to 4 μg/ml, but the CNT sensor can only test down

to 4 ng/ml. In time domain (Fig.3.7b), the normalized resistance of graphene diversifies as the variety of concentraion PSA immunization. However, the labeled sensor has a lower performance than the label free sensor. The reasons are the following: firstly, the label free sensor allows the direct immunoreaction without the amplifying solutions implemented for afterward signaling, which may easily induce the secondary electrical noise [81]; secondly, there is a polymethylmethacrylate (PMMA) passivation layer 300 nm thick on labeled sensor [78], which tends to enervate the absorption of PSA. Although the PSA detection was used for the proof of protocol, this approach should be a generic one for almost any target with a known antibody. Similar experiment was performed for a detection of normal rabbit IgG, and it reconfirmed that the graphene sensor showed better performance than typical one dimentional material CNT in detection limits (Fig. 3.7c, d).

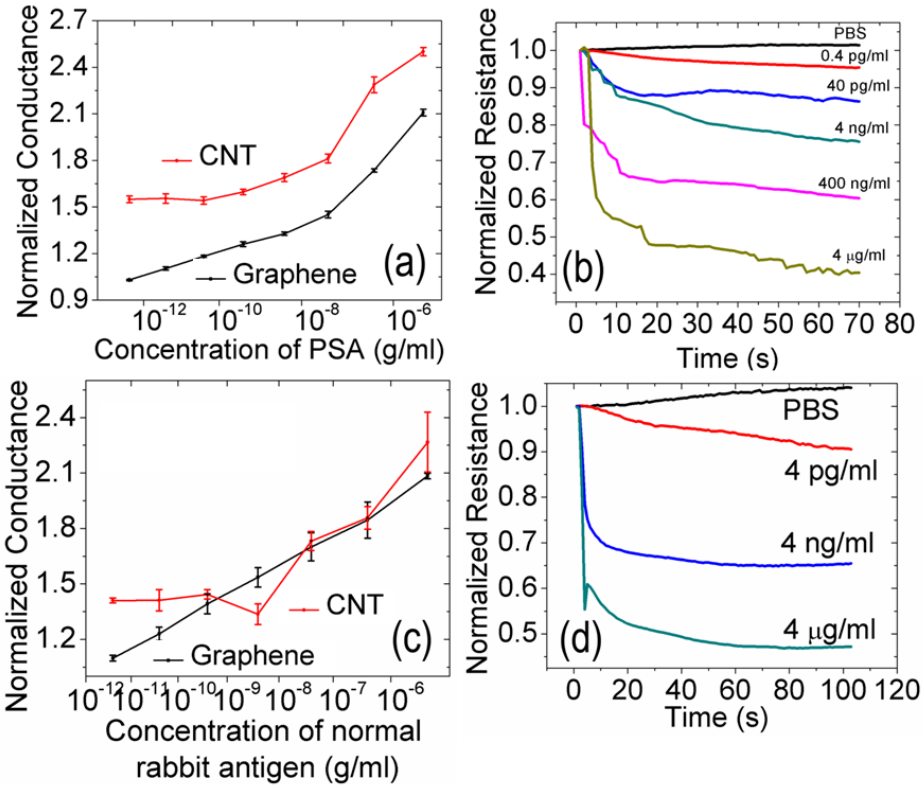

Figure 3.7 (a) Shift in conductance versus concentration of PSA for labeled detection with graphene and CNT biosensors. The detection limit of graphene based sensors is 0.4 pg/ml, showing great advantage over CNT sensors which is only 4 ng/ml. Conductance was normalized by dividing initial conditions which was PBS containing no PSA. (b) Resistance versus time data recorded for labeled graphene sensors detection of different concentrations of PSA. After incubated in various concentration of PSA and labeled by HRP, shifts of graphene resistance were monitored when catalytic reaction started. Resistance was normalized through dividing the resistance at the time when the mixture of ascorbic acid and hydrogen peroxide were induced by the original resistance. (c, d) Similar testing was took place for the detection of normal rabbit antigen IgG. The detection limit of graphene sensors is 4 pg/ml, much better than the CNT sensors with a detection limit of only 40 ng/ml.

### 3.3.5 Vascular Endothelial Growth Factor (VEGF) Detection

VEGF is a biomarker protein generated by cells that stimulate vasculogenesis and angiogenesis, which are critical to restore the oxygen supplied to tissues when blood circulation is inadequate [82]. Pharmacological inhibition of VEGF has been proved effective in inhibiting angiogenesis and vascular leak associated with certain types of cancers such as breast cancer [83] and numerous eye diseases [84]. Therefore, testing and controlling of VEGF are very important to diagnose and control these diseases. The detection and inhibition of VEGF can be realized by using its receptors, such as bevacizumab, andaflibercept. Bevacizumab is an anti-VEGF antibody, and aflibercept is a novel type of soluble decoy receptor with substantially higher affinity than conventional

soluble VEGF receptors. It will be more guidance in the drug usage if the performance and biological activities of different VEGF receptors can be fully understood. By using self-assembly of graphene, a low-cost and sensitiveimmunosensor was synthesized for a real-time detection of VEGF in the range of sub-picogram per milliliter. The VEGF detection performances of different receptors including anti-VEGF antibody 1 from Mayo Clinic, bevacizumab, andafliberceptwere also investigated and compared.

Three types of VEGF receptors performance were investigated based on unsuspended square shape graphene on $SiO_2$/Si substrate. After the VEGF receptors modified onto the LbL self-assembled graphene biosensors, different concentrations of VEGF were introduced onto the label free graphene immunosensors.Each individual chip was sorted into 24-well tissue culture plates to record their resistance shifts by Agilent Data Logger (34970A, Agilent Inc.).

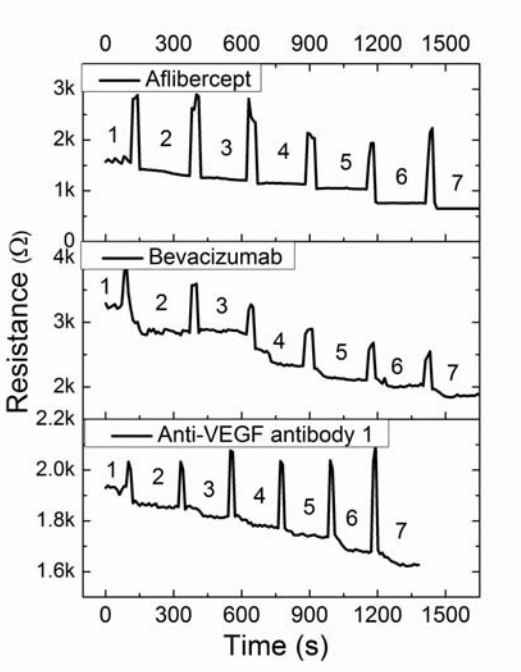

Figure 3.8 Real-time characterization of biosensor modified by different types of receptors. Resistance versus time data recorded after alternate delivery of the following concentrations of VEGF: (1) deionized water contains no VEGF, (2) 1 pg/ml, (3) 10 pg/ml, (4) 100 pg/ml, (5) 1 ng/ml, (6) 10 ng/ml, (7) 100 ng/ml.

As shown in Fig. 3.8, real-time measurement results of different types of immunosensors modified by anti-VEGF antibody 1, bevacizumab, and aflibercept indicate that the anti-VEGF antibody 1 based sensor is capable of detecting 1 pg/ml VEGF, which is the most sensitive sensors among the three types of sensors. In order to confirm the detection limit of graphene biosensor modified with anti-VEGF antibody 1, further investigation was applied. As shown in Fig 3.9, 100 fg/ml and 500 fg/ml VEGFwere introduced. Different outputs were obtained between 0 g/ml and 100 or 500 fg/ml VEGF. But there was no difference between 100 and 500 fg/ml VEGF measurement results.This result demonstrated the detection limit at pico-gram level.

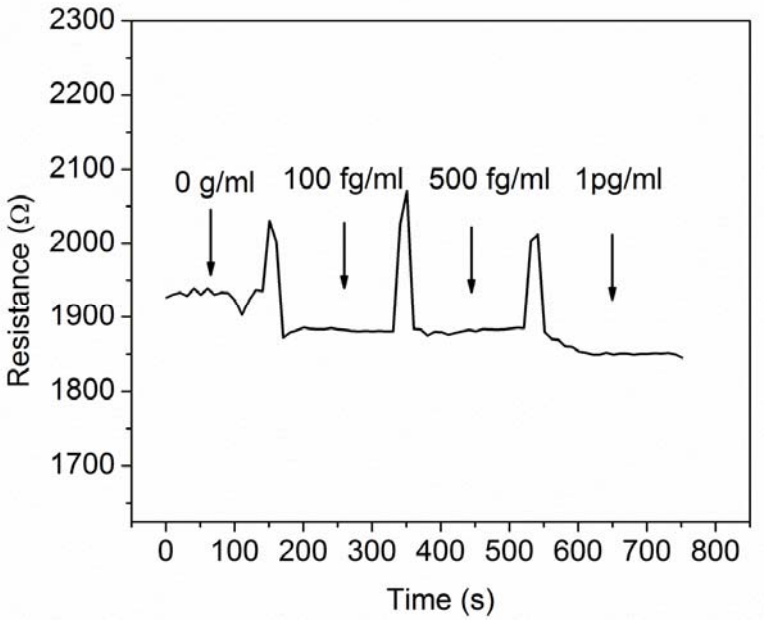

Figure 3.9 100 fg/ml and 500 fg/ml VEGF were detected. There were different outputs between 0 g/ml and 100 or 500 fg/ml VEGF. But there was no difference between 100 and 500 fg/ml VEGF measurement results, which confirmed the detection limit was 1 pg/ml.

### 3.4 Suspended Graphene Biosensor Performance

To date, researches of graphene biosensors have been focused exclusively on graphene supported on substrates, however, the charge traps at the interface and in the substrate have been shown to act as external scattering centers and degrade transport properties in graphene whose atoms are all exposed directly to fluctuations of extrinsic impurities. Researchers have found that the signal-to-noise ratios of suspendedgraphenenanodevices were improved in lowfrequencyregime (below 1 kHz) for both hole and electroncarriers compared with those supported on substrates. But the fundamental mechanism of lower noise brought by suspended graphene structure is still under investigation. In particular, there is no detail discussion about this abnormal phenomenon in the biosensing applications. Herein, suspended graphene sensors were investigated. The fabrication processes were discussed in Chapter 2.

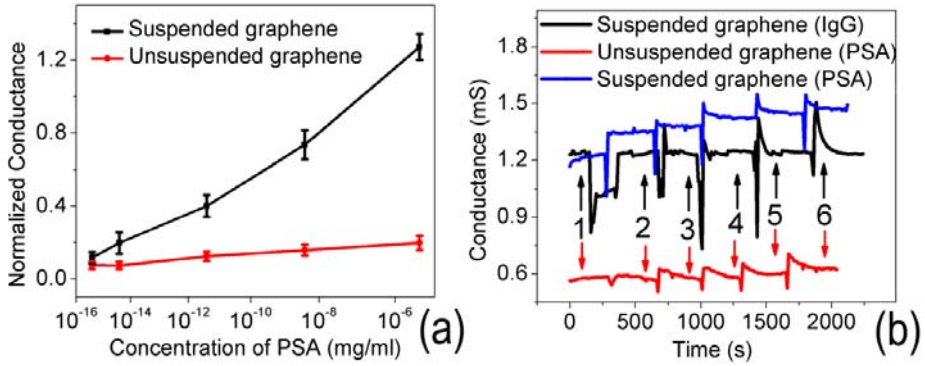

Figure 3.10 (a) Shift in normalized conductance versus PSA concentration for suspended (upper curve) and unsuspended (lower curve) graphene sensors. The detection limit of suspended device can reach down to 0.4 fg/ml. (b) Conductance versus time testing for suspended (first curve) and unsuspended (third curve) graphene with different concentrations of PSA solution induced: (1) PBS contains no PSA, (2) 0.4 fg/ml, (3) 4 fg/ml, (4) 4 pg/ml, (5) 4 ng/ml, (6)4 μg/ml. The results reconfirm that the detection limit of suspended graphene sensor is much better than unsuspended devices. In addition, normal rabbit IgG were delivered to suspended graphene sensor immunized with PSA capture antibodies under the same experiment conditions, and the conductance of graphene sensor kept constant (second curve), demonstrating the specificity of suspended graphene biosensor.

The label free suspended graphene cancer sensor was characterized by measuring conductance with alternate delivery different concentrations of PSA solutions prepared by PBS. Upon the introduction of PSA solution, the sensor resistance went down, that is, the conductance of the sensor increased. The normalized conductance is defined as $G/G_0$ for PSA detection, where $G_0$ is the device conductance in PBS, and G is the device conductance in the PSA solution. Due to the stickiness of water and surface force in micro-scale, all the detection experiments were processed in aqueous environment to avoid the collapse of suspended structure of self assembled graphene. As shown in Fig 3.10a, the normalized conductance of graphene raises with the increase of PSA concentration from 0.4 fg/ml to 4 μg/ml. In comparison, the unsuspended graphene cancer sensor manufactured under the same conditions was conducted to compare with

suspended sensors on the detection limits. It is clear to see that suspended graphene sensors were capable of detecting the shifts from 0.4 fg/ml to 4 fg/ml, but unsuspended devices were not. As shown in Fig. 3.10b, the conductance-versus-time measurements recorded on the graphene biosensor in both suspended and unsuspended situations further confirms the trend in a real-time detection, indicating that the suspension is capable of enhancing the performance of detecting limits. The non-specific reaction of normal rabbit IgG was also implemented to prove the specificity of this biosensor immunized with PSA capture antibodies. By measuring the real-time response of graphene sensor, it is noticed that their conductance were almost the same before inducing 4 pg/ml PSA solution in unsuspended devices, and the signal was very fluctuating. After suspending the graphene, the "step" response of the device led to a much more stable signal. These interesting results are determined by the strong decrease of electrical noise in suspended graphene comparing with the unsuspended one.

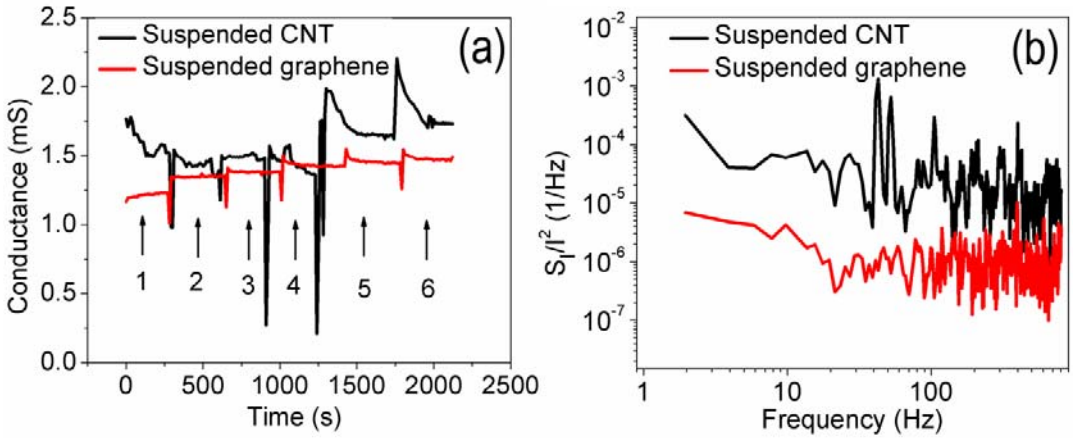


Figure 3.11(a) Conductance versus time testing for suspended graphene (lower curve) and CNT (upper curve) biosensors with different PSA concentrations: (1) PBS contains no PSA, (2) 0.4 fg/ml, (3) 4 fg/ml, (4) 4 pg/ml, (5) 4 ng/ml, (6)4 μg/ml. The results show

that the detection limit of graphene sensor is down to 0.4 fg/ml, compared with the CNT sensor with a detection limit of 4 pg/ml. (b) Normalized noise power spectrum was also characterized for the suspended graphene and CNT biosensor. The result proves that graphene device has lower 1/f noise.

Self assembled CNT sensor manufactured under the same conditions to the self assembled graphene sensor was conducted to compare with graphene sensors on the detection limits. As shown in Fig. 3.11a, real-time results indicate that the CNT sensor was only capable of detecting 4 pg/ml PSA, which was much less sensitive than the graphene sensor. The difference of the detection limits between graphene and CNT sensor can be explained by intrinsic 1/f noise. In the case of CNT such fluctuations noise can arise from trapped charges in the antibodiesor the presence of defects within self assembled tube networks. Interestingly, an effective screening of chargefluctuations from external impurity charges is identified in graphene due to its high quality of crystal lattice and two dimensional honeycombstructure.Such screening effect can explain the reduction of electrical noise level indicated by the normalized noise power spectrum of suspended graphene and CNT sensors, as shown in Fig. 3.11b.

### 3.5 Comparison of Different Graphene and Graphene Composite Sensors

Three types of graphene based composites from pure to hybrid were synthesizedfor the construction of PSA biosensors. The fabrication details have been discussed in Chapter 2. The performance of different types of PSA biosensors were investigated, such as detection limits, sensitivity, stability, etc.

After immobilization of PSA capture antibody, the detection limits of three types of graphene biosensors were characterized by measuring resistance with alternate different concentrations of PSA solutions prepared by PBS. As is shown in Fig. 3.12a and b, the resistance of pure graphene based biosensor decreased with the increasing of PSA concentration from 40 pg/ml to 4 ng/ml. In comparison, resistance-versus-time measurements recorded for the other two types of graphene biosensors manufactured and tested under the same conditions. As is shown in Fig.3.12c and d, microfluidic induced graphene biosensors were capable of detecting the shifts from 4 pg/ml to 4 ng/ml. And self assembled hybrid graphene biosensors had the best detection limits from the "step" response of real-time measurements. As is shown in Fig.3.12e and f, the device presented response down to 4 fg/ml PSA solutions. The surface profile of self assembled hybrid graphene composites have great porous topography, which is more suitable to decorate capture proteins, providing the greatest sensing surface area per unit volume. This factor contributes to the detection limits more. On the other hand, the pure graphene biosensors have the smoothest surface, which demonstrates the lowest detection limits.

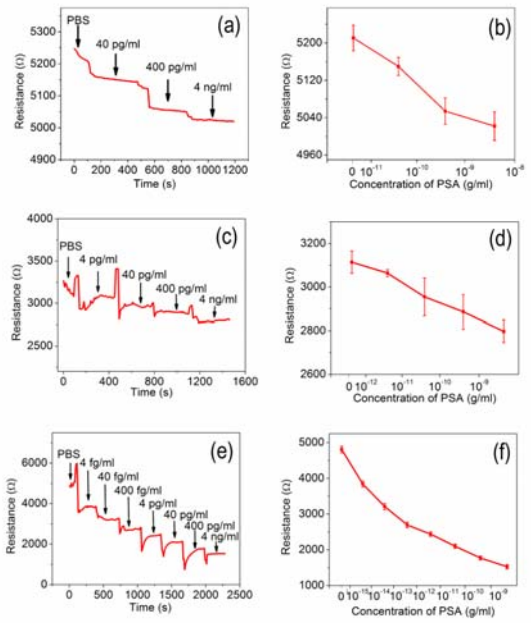


Figure 3.12(a, b) Change of resistance versus PSA concentration for mechanical exfoliation graphene biosensors. The detection limit is 40 pg/ml. (c, d) Shifts of resistance versus PSA concentration for microfluidic induced graphene biosensors. The detection limit is 4 pg/ml. (e, f) Shifts of resistance versus PSA concentration for self assembled graphene biosensors. The detection limit is 4 fg/ml. The data for figures in the right was extracted from the stable region of the real time conductance measurement curve in the left. After delivering the PSA solution each time, it takes several minutes for the resistance to get stable, allowing sufficient inmunoreaction and avoiding the disturbance generated by the delivery of PSA solutions.

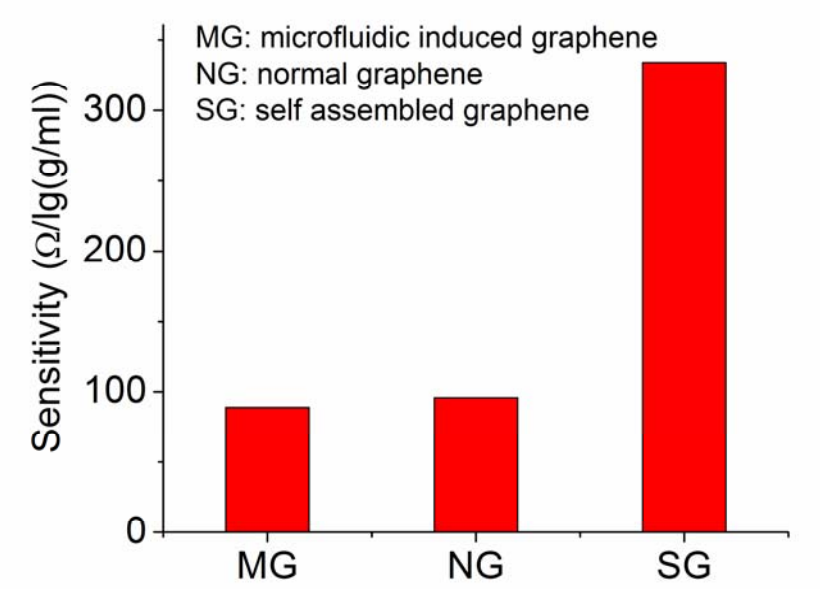


Figure 3.13 Sensitivity analysis of different graphene biosensors. The self assembled graphene presents the highest sensitivity.

The sensitivities of different PSA graphene sensors were compared. The sensitivity is defined as the input parameter change required to produce a standardized output change. Herein, the slopes of calibration lines present the sensitivities of different sensors. As is shown in Fig. 3.13, the self assembled graphene demonstrates the largest sensitivity. This can be explained by the porous surface profile of self assembled graphene, which can enhance the absorption of molecules or ions.

The long-term stability of different graphene biosensors was also investigated, by measuring the response of pH 9 solutions in continuous 7 days. During the non-measurement time, the sensors were kept in PBS water (pH 7) to prevent contamination and disturbance. In order to obtain more clear readout, a normalized resistance was introduced. Resistancefor the PBS (pH 7) measurement was used as an initial resistance

$R_0$. Normalized resistance was represented as the ratio of pH 9 resistance to the initial resistance. As is shown in Fig.3.14, the pure graphene biosensor was most stable, but self assembled graphene biosensor produced much more fluctuation results. The absence of hybrid polymer in the graphene composites results less disturbance compared with the hybridized graphene structures.

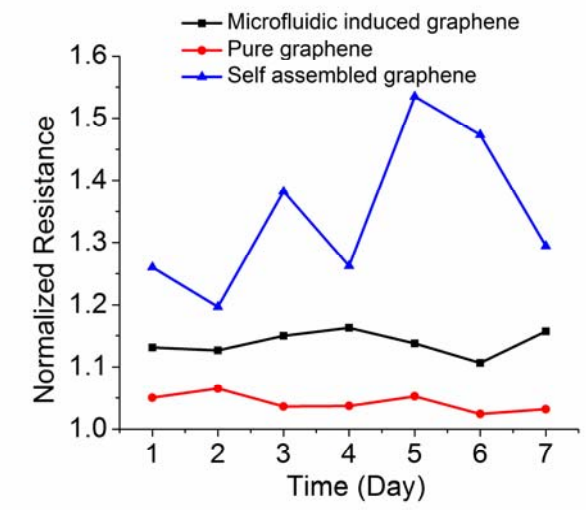


Figure 3.14 Long term stability analysis of different graphene biosensors.

### 3.6 Conclusion

In this chapter, graphene biosensor surface modification processes were presented. The basic sensing mechanism was also investigated. Different biotarget detections were shown, demonstrating this sensor can be a platform to diagnose cancer and other complex diseases.Three different types of graphene biosensors were synthesized and compared. From the comparison of the performance of the different graphene composite biosensors, it can be concluded that all of them can be used for biotarget detection. The self assembled graphene biosensors demonstrated the best detection limits and sensitivity, and

the pure graphene and microfluidic induced graphene biosensors showed the better stability. The trend in sensitivity and stability towards the different graphene structures is dependent on the hybrid polymers, which introduce electrical disturbance for sensor applications but enhance the absorption of target moleculeon the other hand.

# CHAPTER 4

# LOW-COST AND HIGH PERFORMANCE DYE SENSITIZED SOLAR CELL

## 4.1 Introduction

Energy crisis is not only the serious problems human has to face in the future, but also is the key factor to slow the world economic development. With the rapid economic rapid development, the demand for energy continues to increase. Sustainable development is increasingly dependent on energy. Currently, electricity, coal, oil and other non-renewable energy development and utilization has bottleneck, which is increasingly becoming a key restricting element of economic development. Some old oil fields and power stations are approaching their development limit. The high-cost and high-pollution of traditional energy has been difficult to meet the needs of economic development. Therefore, an urgent need for renewable energy development and utilization can meet the urgent energy need from economic and social development [85]. More and more countries have begun to implement and develop photovoltaic, which is the most promising renewable energy technique [86]. The growth of global solar photovoltaic is about six times, with an average annual growth of 50% or more during the past 10 years.With the enhancement of solar cell conversion efficiency and technology, the fabrication cost of solar cell will rapidly decline.

Especially, flexible photovoltaic attracts more and more attentions because it's low-cost, lightweight, and flexible. Due to organic polymer as its main material, flexible solar cell can be folded, curled, attached to the any surface of building [87]. According to the production process, compared with traditional silicon photovoltaic, polymer photovoltaic

preparation process is much easier and lower-cost. Moreover, since the flexible photovoltaic production is expected to achieve a roll-to-roll fabrication, facilitating large-scale continuous production, it is with the potential to greatly reduce production costs. Therefore, the development of flexible photovoltaicis is significant to reduce production costs and broaden the scope of photovoltaic applications.

Among numerous types of solar cells, dye-sensitized solar cells (DSSCs) can provide lower cost and potentially higher efficiency because of their simple structure and high internal quantum efficiencies [88]. DSSCs have force solar cell development to come to a molecular and nano level. DSSCs also provide promising directions due to several exciting research records, including up to 15% record efficiency, critical 1000 hour stability test at 80°C. The DSSC development is more than a solar cell technology, which also include chemical engineering and nanotechnology. Nanotechnology will play more and more important role in the development of DSSC, for example, property investigation in the quantum-size domains and new sensitized dye synthesis. Therefore, nanotechnology provides a powerful tool to create new path to succeed. In fact, the great success of DSSC should thank the application of $TiO_2$ nanoparticles, which is also nanotechnology. With a porous surface electrode, DSSC can utilize a very large internal surface area for heterogeneous electron transfer reactions to produc electricity. Moreover, this $TiO_2$ coated electrode provides a simple way of contacting the electrode interface by an electrolyte. In this chapter, nanotechnology will be fully used to extend the surface area of DSSC much more to achieve better efficiency.

## 4.2 Working Principle of DSSC

In order to sustainable develop global society, renewable energy sources are essential. Global energy consumption rate was increasing year by year due to population growth and technique progresses [89]. Considering the crisis of traditional coal and oil energy, solar energy has the largest potential to satisfy the energy need in future. The sun can release $1.7\times10^5$ TW of solar energy, and 600 TW energy will strike the earth surface. This is huge amount of clean and renewable energy.The sun emits light with a range of wavelengths from the ultraviolet and visible to the infrared. However, the solar light will be influenced by atmospheric absorptionand the position of the sun. Ozone can filter out ultraviolet light, and water and $CO_2$ can influence infrared light.

When the conditions of sky and the positions of sun are different, the solar energy amount the earth can absorb will be different. A standard should be estimated for research and calculation. Nowadays, the light travel path length is called theair mass (AM) and can be approximated by

$$AM = 1/\cos\varphi$$

where φ is the angle of elevation of the sun. The standard solar spectrum used for efficiency measurements of DSSCs is AM 1.5 G (φ = 42° ). The measurement in this thesis strictly follows this standard. After the spectrum normalized by area and time, the radiant energy received is 1000 $Wm^{-2}$[90].

The incident sun light also can be divided as director diffuses light. Sunlight scatteringin the atmosphere makes diffuse light, as a fraction of 15%. DSSCs with porous surfaces are relatively better suited for diffuselight than perfectly flat surfaces and are less sensitive tomovements of the sun.

When researchers investigate solar cell, the most important parameter is energy conversion efficiency (ECE).For a DSSC, ECE isgiven by this equation [91]:

$$\eta = \frac{J_{sc} V_{oc} FF}{P}$$

where η is ECE, $J_{sc}$ is short circuit photocurrent density, $V_{oc}$ is open circuit photovoltage, P is the incident power density, and FF is filling factor of DSSC. FF can be defined by this equation:

$$FF = \frac{P_{\max}}{J_{sc} V_{oc}}$$

The maximum power ($P_{max}$) is obtained as the product of the photocurrent and photovoltage at the voltage where the poweroutput of DSSC is maximal.Another fundamental measurementof the performance of DSSC is the incident photon to current conversionefficiency (IPCE). The IPCE is defined by thephotocurrent density produced in DSSC undermonochromatic illumination divided by the incident photon flux.

$$IPCE = \frac{J_{sc}(\lambda)}{e\Phi(\lambda)}$$

The typical DSSC structure is shown as Fig. 4.1.The main structure frame of DSSC is two parallel electrodes. One is the anode coated mesoporous oxide layer composed of anetwork of $TiO_2$ nanoparticles. The standard ruthenium sensitizers N749 are immobilized on the surface of $TiO_2$ nanoparticles. Another electrode is the cathode coated by Pt. When the incident photons excite the sensitized dye to oxidized state, electrons will be injection into the conduction band of $TiO_2$. The electrons will move to

the cathode, and reaction with the iodide/triiodide redox system, where Pt is the catalyst. The dye is restored to its ground state by electron transfer from the electrolyte.

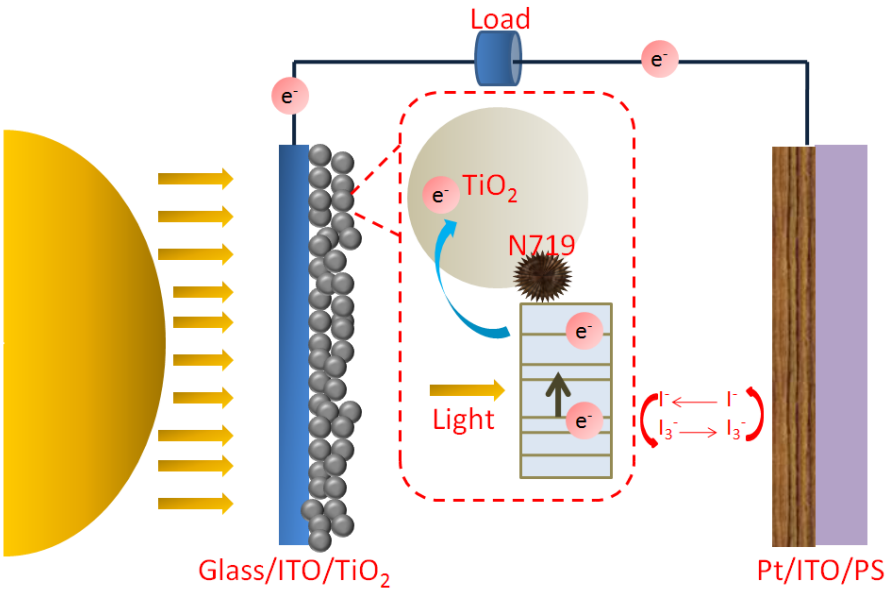


Figure 4.1 The basic structure of typical DSSC.

These chemical reaction equations can demonstrate this photoelectron generation process:

$$Dye + h\nu \rightarrow Dye^{*} \rightarrow Dye^{+} + e^{-}$$

$$Dye^{+} + e^{-} \rightarrow Dye$$

$$I_3^{-} + 2e^{-} \rightarrow 3I^{-}$$

where Dye is ground state sensitized dye, $Dye^{*}$ is excited state sensitized dye, $Dye^{+}$ is oxidized state sensitized dye.

### 4.3 High Performance DSSC with Shrink Induced Nanostructures

Although DSSCs attract more and more attentions, DSSCs have some inherent drawbacks, such as fast recombination and slow carrier diffusion, resulting in lower ECE

compared with silicon based solar cell [92]. Recently, various light manipulation approaches have been proposed to enhance the ECE of photovoltaic devices according to introducing micro/nano structures such as strips [93], nanowires [94], pyramids [95], etc. The appropriate design of micro/nano structures is capable of increasing the light absorption by increasing the internal scattering of incident light and introducing near-field surface plasmonic evanescent waves. Thus, the ECE of photovoltaic devices will be effectively enhanced. Despite several lithographic techniques including electron beam, ion beam and nanoimprint enable the precise fabrication of micro/nanoscale patterns, the inevitable higher cost introduced by these lithographic techniques will weaken the most significant cost advantages brought by DSSC compared with silicon based photovoltaics. Metal wrinkles and nanogaps are natural responses to the stress mismatch between thin films of metal and shrink polymer substrates during heat shrink process, and can be easily extended to large areas at very low-cost [96]. Flexible photodiodes [97], transistor arrays [98], and solar cell systems [99] have been successfully demonstrated by using these low-cost wrinkles. Although the mechanical properties of these devices present an enhancement on wrinkled surfaces, the effects of the wrinkles and nanogaps on the ECE of DSSC have not been explored. In addition, more efforts have been focused on photoanodes in DSSC, leaving the photocathodes of DSSC a lot of unexplored spaces where may offer new paths to enhance the ECE of DSSC. Therefore, the properties of a DSSC with wrinkles and nanogaps on the photocathodes based on shrink polymer were investigated. By simply introducing heat, the shrink stress mismatch between the shrunk polymer substrate and nonshrinkable Pt and ITO films will cause the wrinkles and

nanogaps. These structures can enhance the absorption by light trapping and manipulation, and increase the catalytic surface area of Pt film as well. High performance DSSC was demonstrated based on this low-cost technique.

### 4.3.1 Fabrication Processes

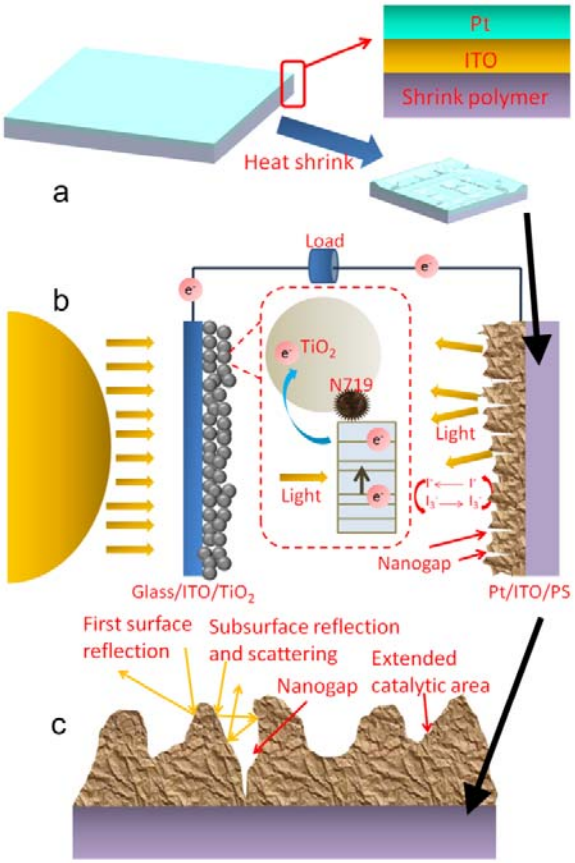


Figure 4.2 (a) Scheme of the fabrication process of shrink induced wrinkles and nanogaps. The shrink polymer substrate with wrinkles and nanogaps generated on the top surface will serve as photocathode. (b) Scheme of DSSCs incorporating with shrink induced structures. (c) Scheme of the photocathodes utilizing shrink induced wrinkles and nanogaps to enhance the incident light scattering and Pt catalytic area.

To form the wrinkles and nanogaps**,** first, ITO/Pt layers were deposited on the shrink polymer(Polystyrene, Shrinky-Dinks, Alex Inc.) with an AJA sputter system (Model ATC 2000). Subsequently, the shrink film coated with ITO/Pt bilayer was placed in a convection oven (Model 280A) at 150° C for uniform heating. The substrate was heated to desired temperature in a slowly rising process allowing approximately 5 minutes and held for 10 minutes. Due to the stiffness mismatch of materials, the shrunk PS material substrates induce the stiffer, nonshrinkable ITO/Pt bilayer to buckle and crack, resulting in the wrinkle and nanogaps. The wavelength of wrinkles and nanogaps can be controllably generated by simply adjusting the sputtering layer thickness.

As shown in Fig. 4.2a, due to the heat shrinkage of the PS substrates, the stiffer, nonshrinkable bilayer filmsintends to buckle, generating the wrinkles quickly and simply. The biaxial compressive stress will crack the fragile ITO layer to obtain the nanogaps. The wrinkle patterned substrate will serve as photocathode in DSSC, as shown in Fig. 4.2b. The dye molecules cannot absorb incident photons completely, and the residual light is reflected or scattered by the photocathode, improving the efficiency of light harvesting. As shown in Fig. 4.2c, the first surface reflectionis strongly directional. Since the wrinkles and nanogaps are introduced to the surface, a light trapping and manipulation behavior due to diffraction and interference effects appears as the subsurface reflection and scattering. He-Torrance model [100] can be used to describe this complex situation, which proposed a bidirectional reflectivity $\rho_{bd}$ consisting of three components:

$$\rho_{bd} = \rho_{first-reflection} + \rho_{directional-diffusion} + \rho_{subsurface-reflection\&scattering}$$

The $\rho_{first\text{-}reflection}$ and $\rho_{directional\text{-}diffusion}$ are due to specular reflection by the mean surface and diffraction scattering by the surface roughness, respectively. The $\rho_{subsurface\text{-}reflection\&scattering}$ is attributed to subsurface reflections and scattering. The governing equations of this mode are listed as below:

$$\rho_{first-reflection} = \frac{|F|^2 e^{-g} S}{\cos\theta_i d\omega_i} \Delta$$

where $\Delta$ is a delta functionwhich is unity in the specular cone of reflection and zero otherwise, $|F|^2$ is the Fresnel reflectivity which depends on the index of refraction of the surface material [101], $g$ is relative to the effective surface roughness, $S$ is the shadowing function [102]. The incident light will determine the $\theta$ and $\omega$. Herein, the wrinkles and nanogaps will greatly increase the surface roughness, resulting in the increasing of parameter $g$. And the $\rho_{first\text{-}reflection}$ will be decreased.

$$\rho_{directional-diffusion} = \frac{|F|^2 GS}{\pi \cos\theta_i \cos\theta_r} \frac{\pi^2 r^2}{4\lambda^2} \sum_{m=1}^{\infty} \frac{g^m e^{-g}}{m!m} \exp(-\frac{\upsilon_{xy}^2 \tau^2}{4m})$$

where the $G$, $\lambda$,$\tau$, and $\upsilon_{xy}$ are determined by the incident light. The wrinkles and nanogaps will increase $g$, and then increase the term $g^m e^{-g}$. Therefore, the diffraction scattering term $\rho_{directional\text{-}diffusion}$ is increased by introduction of wrinkles and nanogaps.

$$\rho_{subsurface-reflection\&scattering} = \alpha(\lambda)$$

This term is relative to the multiple surface reflections, subsurface reflections or light scattering. Surface profile of light scattering material is very important to determine this term. In our case, the wrinkles will attribute the first and second components, but the nanogaps will be relative to the third components

To Fabricate DSSCs, first, the photoanodes were fabricated based on ITO coated glass (thickness, 1.1 mm; IT5-111-25; Nanocs, Inc.) The substrate was cleaned in acetone under ultrasonic condition for 15 min, and then rinsed with water. After blowing dry, a layer of $TiO_2$ paste (P6-2100-13; Aqua Solutions, Inc.) was coated on the ITO glass plates by doctor blading. After drying for 10 minutes, the substrate was placed on a hotplate for 30 minutes at 450° C. Then, the $TiO_2$ coated substrate was treated by UV light for 24 hours. After that, the substrate was immersed into 0.5 mM N719 dye (703214; Sigma-Aldrich, Inc.) solution in ethanol for 24 hours to load the sensitized dye onto the electrode. The photocathodes were prepared from shrink polymer coated with ITO/Pt. The electrolyte was 50 mM of tri-iodide in methoxypropionitrilepurchased from Solaronix Inc. The dye-loaded $TiO_2$ photoanodes and photocathodes with shrink induced structures were assembled into a DSSC, and sealedwith epoxy (1838B/A; 3M Inc.).

### 4.3.2 Characterize of Shrink Induced Nanostructures

To manipulatethe incidentlight by controlling the wavelength of the wrinkles and nanogaps, several factors, such as the thickness of the thin films, the material properties of the filmand PS substrate, play very important roles. To control the wavelength ofshrink induced wrinkles, it is critical to understand the mechanism of generation of wrinkles depending on the material properties of the nonshrinkable film and shrink polymer substrate. Wrinkles are the competition results between the elastic bending energy of the ITO/Pt film and the elastic energy of deformation of the shrink film substrate. The wrinkle wavelength can be described as below [96, 103]:

$$\lambda \propto \eta^{1/3} h$$

where λ is the wrinkle wavelength, $h$ is the thickness of the nonshrinkable films, and $\eta$ is the ratio of the nonshrinkable thin film's young's modulus to the PO's young's modulus. According to experiment analysis results shown in Fig. 4.3c, the wavelength of wrinkles are increased along with the increasing of ITO thickness, which confirms this theoritical model. In experiments, there were no boundary conditions applied, resulting in the biaxial shrink mechanism. Another critical parameter is the persistance distance $j$, over which wrinkles lose orientational coherence. It is defined as below [96, 103]:

$$j \propto \eta^{2/3} h$$

From this equation, this wavelength for biaxial shrink is also proportional to the film thickness. Therefore, the wavelength of the shrink induced wrinkles can be easily adjusted by depositing different thickness of ITO/Pt films.

The nanogaps are introduced by the cracking of ITO layer. The formation of the wrinkles is given by the fighting between the bending stress of the nonshrinkable thin films and the deformation stress of the shrink polymer substrate [104].When wrinkles occur, the fragile ITO film is not strong enough to support the tensile stress induced by bending in the film and a crack initiating from the upper surface of the film. To analyze the cracking process, some researchers have proposed a critical stress $\sigma$:

$$\sigma \propto \frac{E}{\sqrt{1-v^2}}$$

where $E$ is the material young's modulus, and $v$ is the Poisson ratio. If the compressive stress brought by the shrink process is smaller than $\sigma$, the cracking is impossible. Thus,

smaller $\sigma$ will have much more chance to introduce these nanogaps. According to the material properties, the ITO will offer much smaller $\sigma$ than Pt.

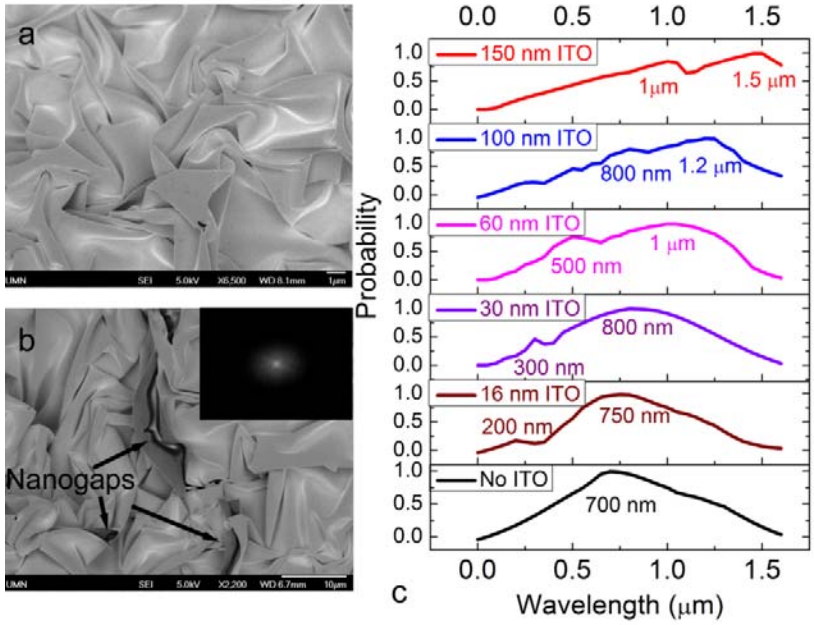


Figure 4.3 (a) SEM image of wrinkles generated from shrunk Pt film 50 nm thick without ITO layer. (b) SEM image of wrinkles and nanogaps obtained from shrink ITO/Pt films with 30/50 nm thick. Inset: the disc-shaped 2D FFT pattern, indicating a broad distribution of wavelength in k-space. (c) Wavelength distributions of shrink induced nanostructures are generated fromdifferent bilayers with various thickness of ITO layer, but the Pt films are kept as 50 nm thick.The larger wavelength peak represents the wrinkles and the smaller one is for nanogaps.Two spectra peaks are measured by introducingthe ITO films, but only one peak appears without ITO film, which confirms that fragile ITO layer causes the nanogaps.

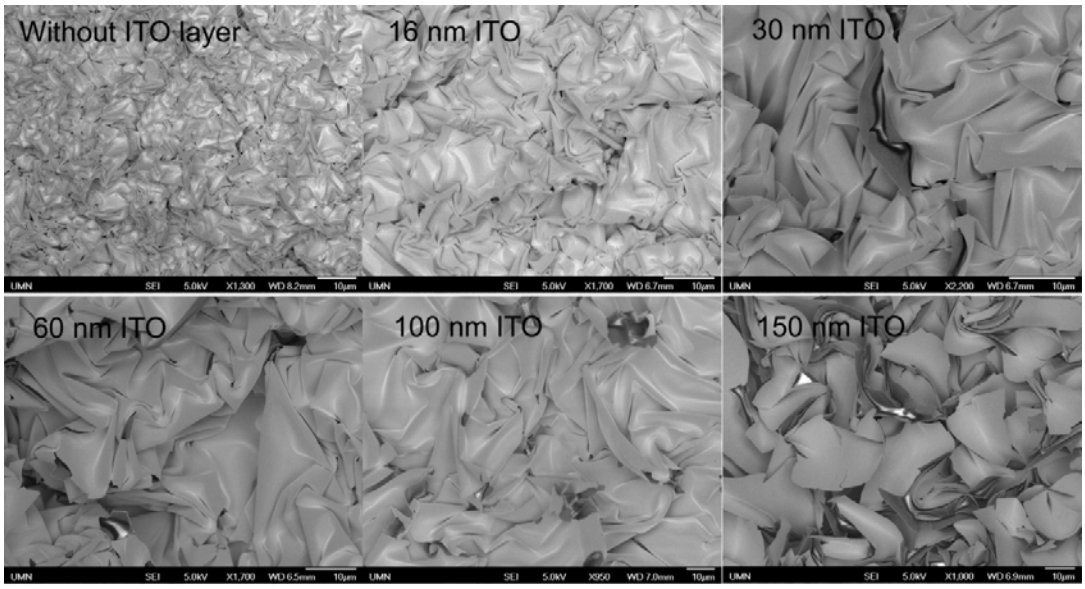


Figure 4.4 SEM images of different thickness of ITO layers incorporated with 50 nm Pt film deposited on PS substrate after shrinking.

SEM images (Fig. 4.3a, b, Fig. 4.4) were used to investigate the wrinkles and nanogaps generated by shrink process. The absence of ITO layer will result in only wrinkles by shrinkage of Pt film (Fig. 4.3a), and the fragile ITO layer will introduce the nanogaps by the cracks after shrinking (Fig. 4.3b). In order to quantitatively determine the wavelength of shrink induced wrinkles and nanogaps, SEM images were analyzed by using mathematic analysis and multiple image processing with the assistance of Matlab program. The images were first treated by Canny Operator, the most optimized algorithm of edge detection, to reduce low frequency component. Then, the images were filtered by median filter, an efficient algorithm to eliminate salt and pepper noise, to reduce high frequency component. After that, two-dimensional fast Fourier transform (2D FFT) was applied to the images. The fundamental formula of is shown as follow:

$$F(u,v)=\frac{1}{\sqrt{MN}}\sum_{x=0}^{N-1}\sum_{y=0}^{M-1}f(x,y)e^{-j2\pi(\frac{u}{M}x+\frac{v}{N}y)}$$

N, M is the width and height of image with the unit pixel. However, from the 2D FFT analysis, we still cannot qualitatively obtain the distribution of wavelength. But it was easier to quantitatively measure the wavelength distribution from the view of power. Thus, we transferred 2D FFT into a power spectrum density (PSD). According to Parseval law, PSD and FFT of signal share the relationship as follow:

$$S_x(f)=\lim_{T\to\infty}\frac{1}{T}\left|X(f)\right|^2$$

After reorganization, it shows that:

$$PSD(u,v)=\frac{1}{MN}\left|\sum_{x=0}^{N-1}\sum_{y=0}^{M-1}z(x,y)e^{-j2\pi(\frac{u}{M}x+\frac{v}{N}y)}\right|^2$$

The distribution of wavelength can be estimated by further transforming corresponding PSD to real space.

The disc-shaped power spectral density indicates a broad distributionof wrinkle and nanogap wavelength in k-space (the inset of Fig. 4.3b). As shown in Fig. 4.3c, different thickness of ITO layer incorporated with 50 nm Pt film were quantitatively investigated. Two spectra peaks will show up by introducing ITO films, but only one peak appears without ITO film, which confirms that fragile ITO layer causes the nanogaps. The larger wavelength peak represents the wrinkles and the smaller one is for nanogaps. The wavelength and distribution of wrinkles and nanogaps can be easily tuned by simply adjusting the thickness of ITO layer.

### 4.3.3 Characterization of DSSC

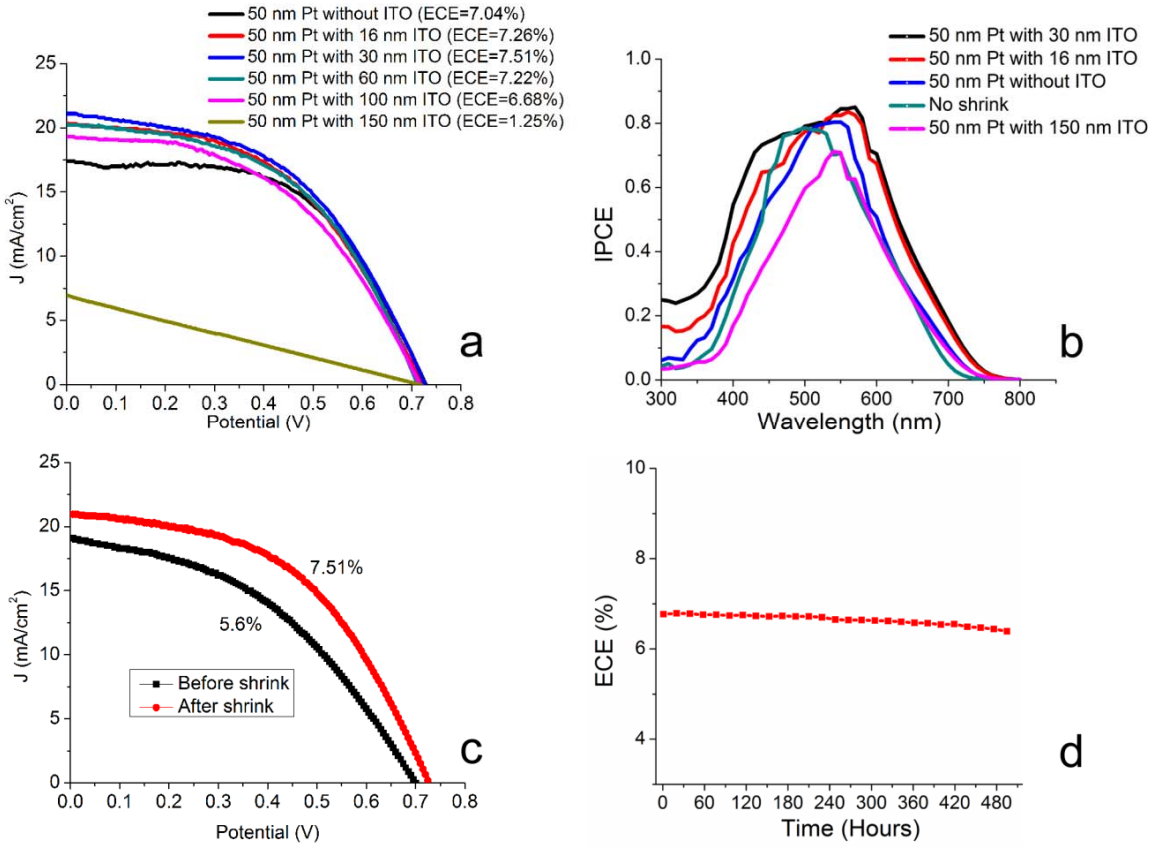


Figure 4.5 (a) The current densities versus voltage characteristics of the DSSCs with various shrink induced nanostructures due to different thickness of ITO layers. Only properly designed structures can enhance the ECE greatly. (b) IPCE spectra of DSSCs with different photocathodes. The nanogaps with 200 nm and 300 nm wavelength, generated by ITO with 16 nm and 30 nm thick respectively from the quantitative analysis, enable a great IPCE enhancement at incident wavelengths from 300 nm to 400 nm. (c) The optimal DSSC with Pt/ITO 50/30 nm thick presents 34.1% increase of ECE compared with DSSC with the flat photocathode. (d) Long term stability characterization

of DSSCs. The DSSCs kept 94% of its initial efficiency after 500 hours at 60° C under a real irradiance of successive outdoor sunlight soaking.

To investigate the ability of manipulating light of wrinkles and nanogapsin DSSC, we fabricated DSSCs with different nanostructures on the photocathode. By depositing different thickness of ITO and Pt films, various wavelengths of wrinkles and nanogaps were generated by shrink process. After quantitatively analyzing the wavelength distribution of wrinkles and nanogaps as well as the testing results of DSSCs, the optimal enhancement of efficiency can be easily achieved. N719 was used as the photo-absorbing dye in our DSSCs, and the photoanode was fabricated by conventional method. Instead of flat Pt film on ITO glass, the shrink polymer with wrinkles and nanogaps served as photocathode. As shown in Fig. 4.5a, the current densities versus voltage characteristics of the DSSCs with different ITO layers demonstrate that the ECE is relative to the different surface profile of photocathodes. According to the analysis of surface profile of photocathodes, the Pt coated substrate without ITO will have no nanogaps, presenting only 7.04 ± 0.12 % efficiency. After introducing nanogaps by depositing ITO layer underneath Pt film, the ECE will rise up to 7.51 ± 0.18 % at ITO 30 nm thick, and then drop along with the increasing of ITO thickness.

We also kept the ITO with constant 30 nm thick, and adjusted the thickness of Pt films. As shown in Fig. 4.6, the characterization results also confirm that the photocathode with 30 nm ITO and 50 nm Pt will give the optimal results. Though the photocathodes have various surface structures generated by different thickness of ITO and Pt, we observed

almost the same $V_{oc}$ of 0.7 V for all the DSSC. However, the $J_{sc}$ presented different responses relative to the surface nanostructures.

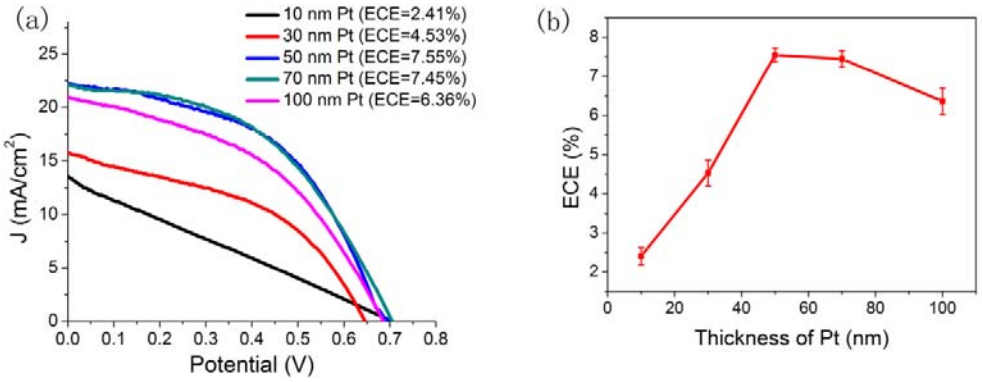


Figure 4.6 (a) The current densities versus voltage characteristics of the DSSCs with various shrink induced nanostructures. The ITO layer was kept as 30 nm thick, but the thickness of Pt film was different. (b) The ECE of different samples corresponding to the testing in (a). Ten devices were tested, and the error bars represent standard deviations in values.

As shown in Fig. 4.5b, the IPCE spectra of DSSCs with certain wavelength of nanostructure on photocathodes showed the enhancement extending over the wavelength range from 300 nm to 750 nm. Especially, the introducing of nanogaps with 200 nm and 300 nm wavelength (ITO with 16 nm and 30 nm thick respectively) presented a great IPCE enhancement at incident wavelengths from 300 nm to 400 nm.

The ECE enhancement can be contributed to the increase of light scattering and/or trapping induced by the textured platinum/ITO back contact, as well as the expended catalytic surface area of Pt film. We also investigated the effects of these factors on the enhancement of ECE. As shown in Fig. 3c, the optimal DSSC with Pt/ITO 50/30 nm

thick presents 34.1% increase of ECE compared with DSSC with the flat photocathode. First of all, the shrink process will offer 4 times larger Pt catalytic surface area due to reduction by half of the lateral dimension of shrink polymer substrates.

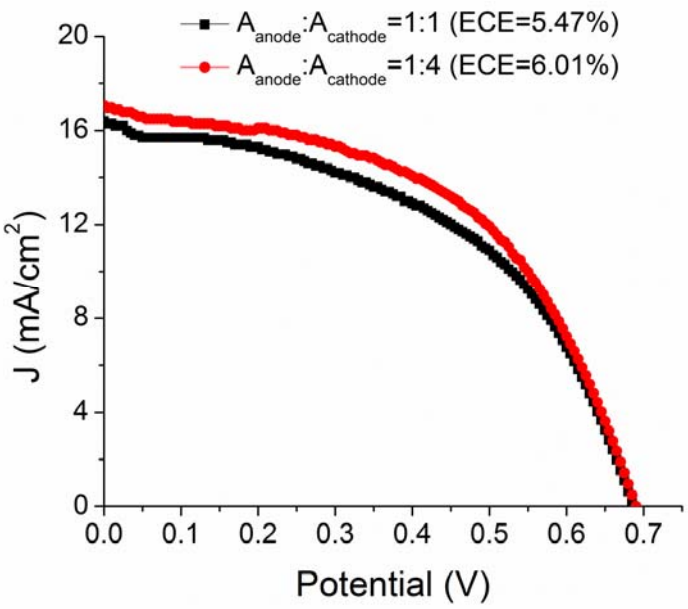


Figure 4.7 Comparison of DSSCs with same photoanodes but different photocathode area.

As shown in Fig. 4.7, we compared the ECE of DSSCs with same photoanodes but different photocathodes area, showing only 9.9% ECE enhancement with the enlargement of Pt catalytic area. Therefore, besides the enlarged catalytic area, these shrink induced wrinkles and nanogaps will efficiently improve the ECE by the light scattering effect. The multiple scattering of light will lead to an increasing of optical path length and the optical absorption, thereby increasing the ECE. However, the DSSC with only wrinkles can provide 7.04 ± 0.12 % efficiency, compared with 5.60 ± 0.15 % efficiency from photocathodes, showing only 25.7% enhancement in ECE. So the nanogaps are capable of supplying more photon scattering and diffusion between the interfaces. But the

wavelength of nanogaps should be controlled at an optimal level. Huge wavelength of nanogaps will introduce large cracks to the electrodes. This will result in larger sheet resistance of electrodes (Fig. 4.8), and dramatically decrease the ECE, which has been confirmed in Fig. 4.5a.

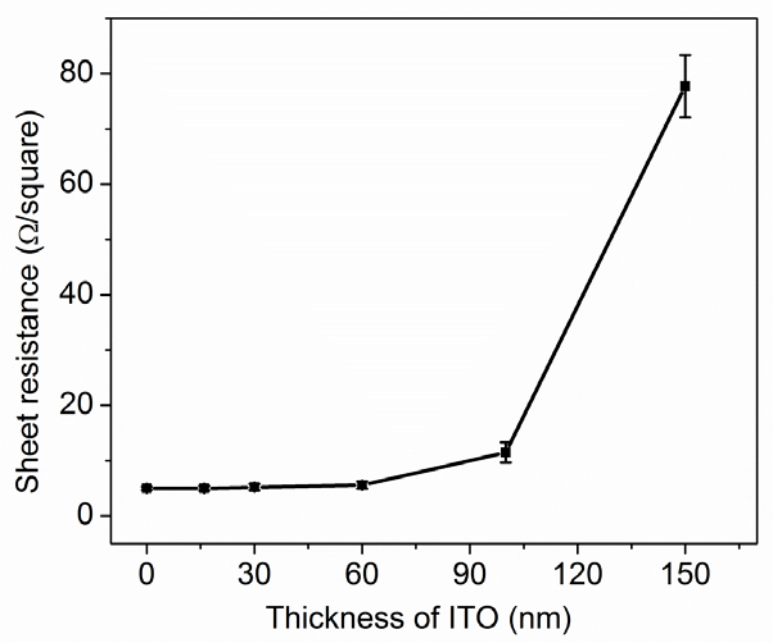


Figure 4.8 Sheet resistance of different thickness of ITO layers with 50 nm Pt film deposited on PS substrate after shrinking.

In addition, we observe the peak of the IPCE spectrum for the conventional sample (no shrink) locates at around 500 nm, which is consistent with previous results using the same type of dye [105], while other samples with textured back contact are red-shifted with respect to the conventional samples. This red-shift is attributed to plasmon resonance effect, which promoted by the structured back contact [106].

In addition, the device stability of our best sample was characterized, shown in Fig. 4.5d. According to the optimization analysis, the ITO/Pt with 30/50 nm thick was deposited on

the shrink polymer to form the photocathode after shrinking. After fabrication, the DSSC was stored under a real irradiance of successive outdoor sunlight soaking for 500 hours at 60° C. It only counts daytime for the 500 hours in the characterization, but the DSSC was still exposed to the real outdoor environment during the night time. To obtain the ECE, the I-V curves of DSSCs were measured by electrochemical station under a calibrated AM 1.5 solarsimulator at 60° Cevery day. The initial ECE of the testing cell are 6.77%, and this cell exhibited a good stability, still keeping 94% ofits initial efficiency after 500 hours of aging.

### 4.4 All Polymer and Flexible DSSCs

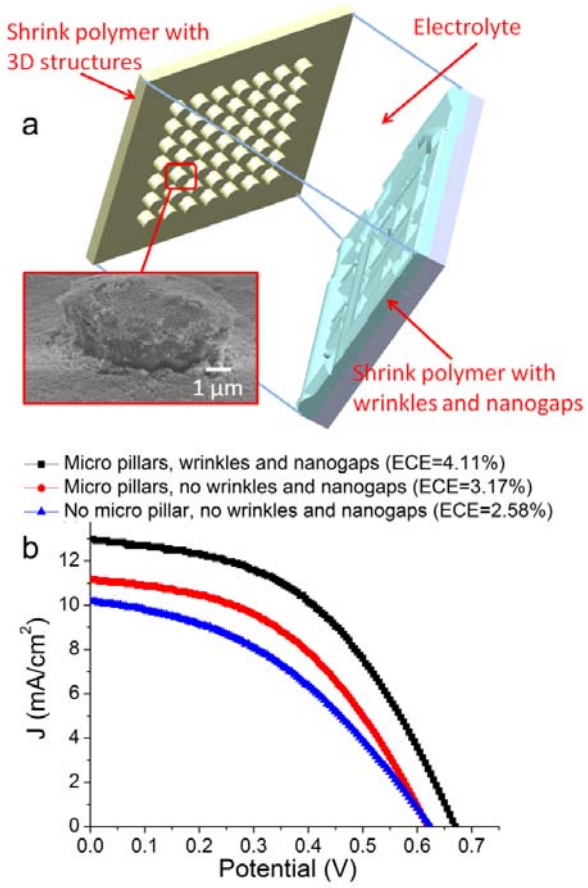

Figure 4.9 (a) Scheme of all-polymer DSSC with shrink induced structures on both anode and photocathode. Inset: SEM image of shrink induced micro pillar coated with $TiO_2$. (b) The current densities versus voltage characteristics of DSSCs with or without shrink induced structures. There is up to 59.3% ECE enhancement of DSSC with shrink induced micro/nanostructures compared with the control group with flat electrodes.

As shown in Fig. 4.9a, the conventional glass photoanodes was replaced with patterned shrink polymer substrate coated with $TiO_2$ to form all-polymer structure of DSSC, and investigated the enhancement of ECE by the shrink induced structures. It has been proposed to enhance the ECE of DSSC by introducing micro/nanostructures on the photoanodes. However, the conventional fabrication methods on glass substrate are very high-cost, compared with the shrink polymer substrate combining with hot embossing process. By shrink processes, shrink polymer is capable of generating high aspect ratio and various feature sizes of micro structures from a single mold by controlling shrink temperatures.The fabrication processes were presented in Fig. 4.10. First, the shrink polymer based photoanodes were fabricated with micro pillar arrays. A silicon mold was fabricated by photolithography and ICP dry etching (Fig. 4.11). Next, the patterns were transferred from the silicon mold to the shrink polymer by Maual Pressor (Model Grimco 12-1-HT). Then, the patterns on the shrink polymer were gently polished and removed by sandpaper. Subsequently, the polished shrink polymers were shrunk at 150° C to obtain high respect ratio micro pillar array.After deposition of 100 nm ITO, a layer of $TiO_2$ paste was blading coated on the patterned shrink polymer substrate, then dried for

30 min at 150 ºC followed by UV light treatment for 24 hours. The photocathodes and assembly procedure were the same with the fabrication of DSSCs discussed above.

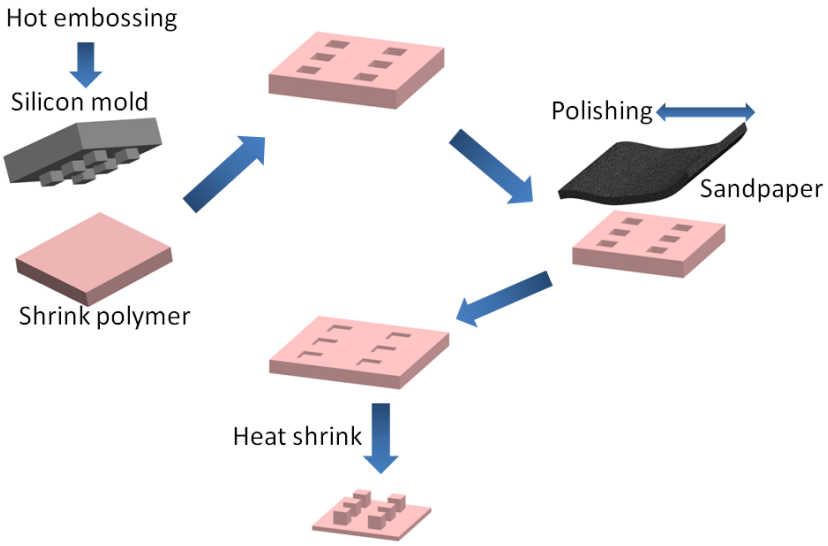


Figure 4.10 Schematic illustration of fabrication process of micro pillar array on shrink polymer substrate.

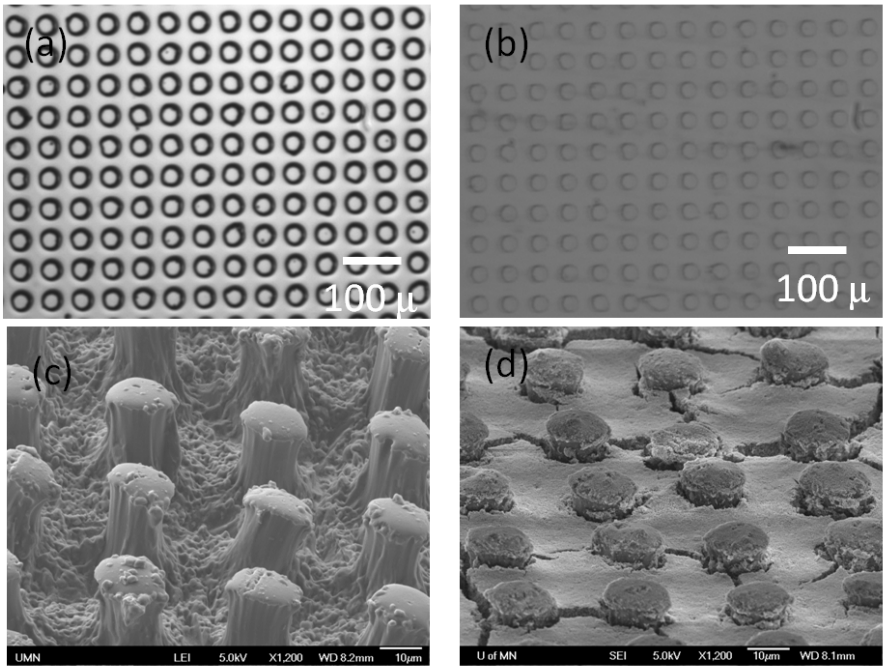

Figure 4.11 (a) Optical images of fabricated silicon mold. The diameter of micro pillar is about 30 μm. (b) Optical images of embossed pattern on PS substrate. (c) SEM image of micro pillar array on photoanodes after shrinking. The diameter of micro pillar is about 15μm. (d) SEM image of $TiO_2$ coated photoanodes with micro pillar array.

Here, we fabricated three groups of all-polymer structure DSSCs to investigate the enhancement of ECE, as shown in Fig. 4.9b. The photoanodes of first group of DSSCs constructed on the shrink polymer substrate with micro pillar array patterns (Fig. 4.11), and the photocathodes were fabricated with wrinkles and nanogaps by shrink process. The second groups of DSSCs had the same photoanodes with the first group, but the photocathodes were flat without any shrink induced structures. The third group was the control group, and both the photoanodes and photocathodes were flat without any shrink induced structures. The control group has only 2.58 ± 0.23 % efficiency, and the patterned photoanodes will provide 3.17 ± 0.15 % efficiency. The first group is capable of offering up to 4.11 ± 0.18 % efficiency, demonstrating 59.3% enhancement of ECE by shrink induced structures on both the photoanodes and photocathodes.

A flexible all polymer DSSC was also developed. As shown in Fig. 4.12a, to fabricate the flexible photoanodes with micro pillar arrays, a silicon mold was fabricated by photolithography. Next, the patterns were transferred from the silicon mold to the shrink polymer by embossing. The patterns on the shrink polymer were gently polished and removed by sandpaper. Subsequently, heat was applied to the polished shrink polymers at different temperatures to obtain various shrink polymer molds. By controlling the shrink temperatures, different densities of pillar array were obtained. The shrink polymer

molds were used to generate the PDMS chip with micro pillar arrays. A layer of $TiO_2$ paste was blading coated on the patterned PDMS substrate on top of 100 nm ITO, then dried for 30 min at 150 ºC followed by UV light treatment for 12 hours. After N719 dye adsorption for 24 hours, a $TiO_2$ photoanode and a platinum/PET counter-cathode were assembled to form a sandwich-type cell, and sealed with epoxy. Due to the all-polymer structure of the DSSC, it is capable of bending at a large degree (Fig. 4.12b, c).

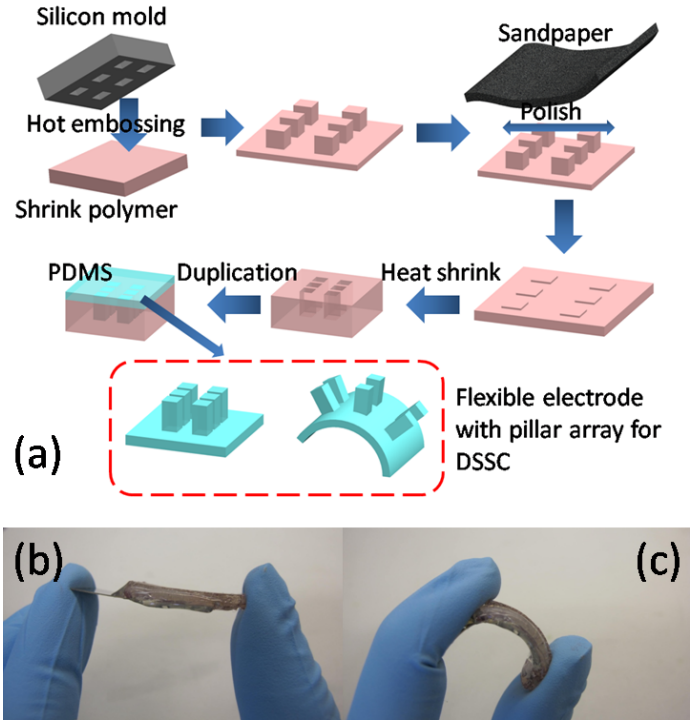


Figure 4.12 (a) Schematic illustration of fabrication processes of the flexible electrode with micro pillar arrays; (b) Unbending state of DSSC; (c) Bending state of DSSC. The all-polymer structure of DSSC presents very good flexibility.

As shown in Fig. 4.13, the fabricated micro pillar arrays were also inspected by SEM, presenting the decreased feature size compared with original size on the molds. We further investigated performance of DSSCs with different densities of pillar arrays (Fig.

4.14). Compared with a non-shrink plat substrate without micro pillar arrays, the ECE was increased by 45.7% for high densities pillar arrays (60 μm pitch, 10 μm in diameter). In addition, bending effect of the flexible DSSC was also studied, demonstrating that the DSSC with 3D structures had better performance after bending, compared with the samples without structures (Fig. 4.15).

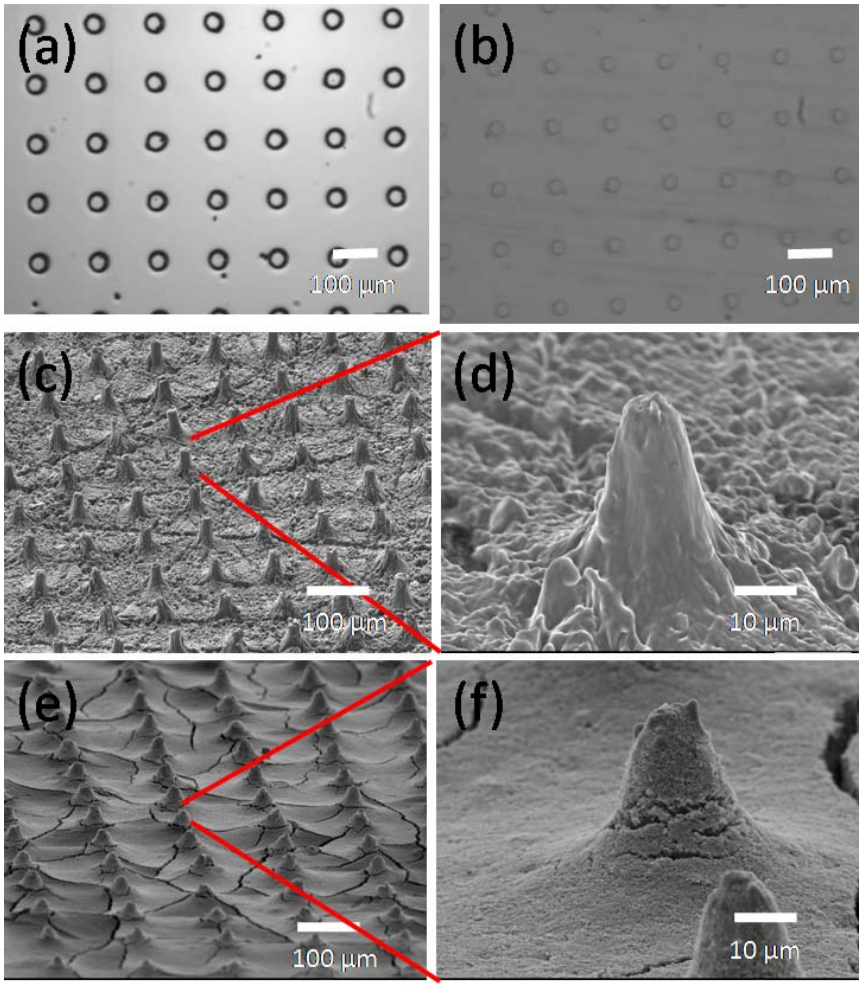


Figure 4.13 (a) Optical microscopy image of pillar arrays on silicon mold (120 μm pitch, 30 μm diameter); (b) Patterns on shrink polymer before shrink (c) SEM images of Pillar arrays fabricated on PDMS (60 μm pitch, 10 μm diameter); (d) High magnitude SEM

image of pillar; (e) Substrate is coated with $TiO_2$ by doctor blade method; (f) High magnitude SEM image of pillar coated with $TiO_2$.

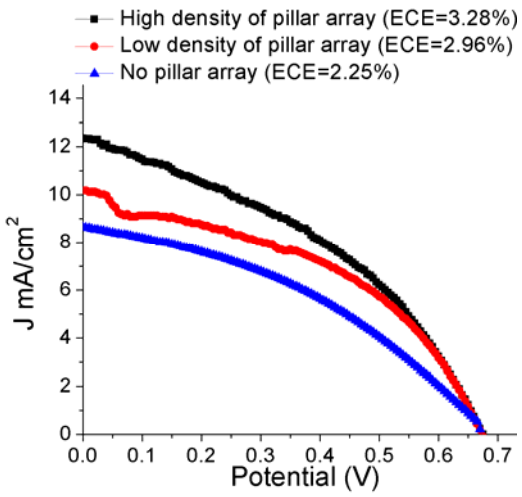


Figure 4.14 I-V curves of DSSCs with different densities of pillar arrays. The high density of pillar array electrode (60 μm pitch, 10 μm diameter) can enhance the ECE by 45.7% compared with no pillar array electrode. The ECE is rising along with the increasing of pillar array density. The density of pillar arrays can be simply controlled by adjusting the shrink temperature.

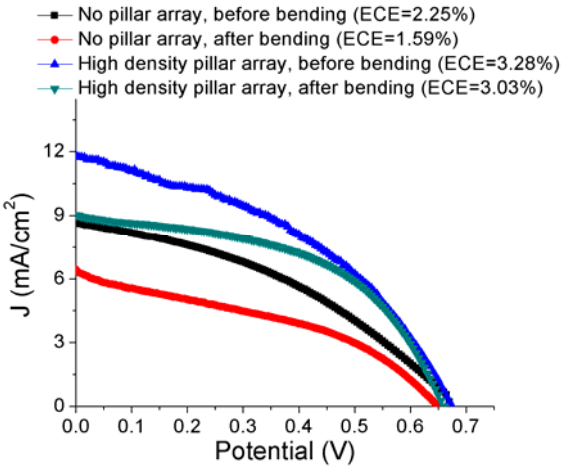

Figure 4.15 Characterization of bending effects on DSSC. DSSC with 3D structure will keep better performance compared with no structure ones. The ECE only decreases 7.6% for DSSC with 3D structure, but 29% for the DSSC without 3Dstructure. The decreasing of ECE after bending was caused by the cracking of ITO layer, which were mentioned in several other literatures.

### 4.5 Conclusion

In this chapter, the background of solar cell development was introduced, and the basic mechanism of DSSC was investigated. Wrinkles and nanogaps on shrink polymer substrates are natural responses to the heat shrink induced stress mismatch of materials, and can be easily introduced to large areas in a very low-cost way. By using these shrink induced structures on the photocathodes, the ECE of DSSCs can be enhanced 34.1% due to the increase of light scattering and/or trapping as well as the enlargement of Pt catalytic surface area. Especially, these nanogaps enhance the light absorption at the incident wavelength from 300 nm to 400 nm. Moreover, the shrink polymer can also provide low-cost patterns on photoanodes, demonstrating all-polymer structure of DSSC with 59.3% enhancement of ECE. The all-polymer structure DSSC can provide great flexibility. It is believed that these low-cost shrink induced micro/nanostructures enable to extend in many other photovoltaic deviceapplications such as quantum dot solar cells and organic solar cells.

# CHAPTER 5

# SHRINK INDUCED FABRICATION AND APPLICATIONS

## 5.1 Introduction

The semiconductor industry has achieved continuing reductions in device feature size with optical photolithography due to decreasing of the exposure wavelength with accompanying improvements in the photoresist chemistry and optics techniques [107]. At the same time, the costs and complexity increase significantly with each decreasing in wavelength for optical photolithography. Unfortunately, decreasing the wavelength from the current state of the art presents very significant technical challenges. Nowadays, the developments of novel lithography techniques provide promising approaches to offer high performance in resolution. A variety of lithography techniques such as scanning electron beam [108], nanoimprint [109], dip pen [110], copolymer [111], and chemical resolution enhancement [112], have effectively achieved sub 100 nm resolution with better performance. But the resolution limits still have much space to improve. And many of these lithography techniques are incredible expensive and complex to realize. Therefore, alternatives to traditional optical photolithography are being pursued to continue decreasing device size in a low cost way.

Lithography can be divided into two categories on the basis of patterning strategy: parallel replication and serial writing. Nanoimprint lithography is a typical parallel patterning process in which a mold is pressed into a deformable material to generate a pattern in nanometer scale [113]. The simplicity of this type of technique, especially its success in transferring nanoscale patterns with high quality, make it attractive for a wide

range of applications. Nanoimprint is a typical mechanical process, therefore, the resolution is not limited by the diffraction of light or the photoresist chemistry and development, as generally in optical photolithography. As the template fabrication process improves, imprint resolution should also improve as well. Nanoimprint lithography has generated sub-20 nm resolution. However, the template is the critical limitation of nanoimprint lithography. A high resolution template is required, which is usually very expensive and complex to obtain. Besides, the patterns cannot be changed once the mold is fixed. Scanning electron beam lithography is a typical serial writing method by emitting a beam of electrons in a patterned way across a surface coated with a special photoresist to create very small structures in the resist that can subsequently be transferred to the substrate material. Scanning electron beam lithography has successfully demonstrated sub-10 nm resolution [108], however, it requires point by point pattern in a serial manner, which greatly increases the cost and prevent its economical practical for mass production.

In order to overcome the drawbacks of the two types of lithographic methods, Several unconventional lithography methods have been proposed. Dip pen lithography is an unconventional patterning process which is capable of fabricating nanometer scale patterns in a low cost way [114]. In its patterning work, a coated probe served as a "pen" in which the tip of the probe was the drawing "nib". Molecules or polymer absorbed onto the pen became the "ink," and the sample substrate was the "paper." By pressing the tip aganist the substrate, the "ink" moves on the substrate by capillary transport through the meniscus, which transfers the patterns from the mold to the

substrate. Due to its low cost and facility, the dip pen lithgraphy can achieve nanometer scale pattern without the limitation of the multiple materials patterning at the same and the types of the materials. But this tpye of untraditional lithography also suffers from the high cost of the template. Beside, it is even harder to achieve very small featrue size due to its expansion results and the requirements of optimized working conditions. Copolymer lithography is another unconventional lithography which is also capable of offering sub-25 nm resolution [115], by using self assembling polymers to define templates for patterning dense features at nanometer scale. One of the advantage of the copolymer lithography is the fabrication of large-area periodic nanoscale structuresusing in a simplicity and low cost process. But it suffers from the limitation of pattern variety due to the copolyer properties. Only limited types of periodic pattern shapes are possible to generate due to the chemical and physical properties. Chemical resolution enhancement lithography is a sidewall formation process by making use of the thermal cross-linking reaction with the acid existing at the resist wall [112]. After fine resolution lithography process, the chemical material is applied to the developed pattern, and forms the side wall further. As a result, the original resolution is reduced. It has an obvious disadvantage that it depends on the original fine resolution lithography method. It cannot fabricate nanometer scale pattern without assistance of other lithography.

To overcome the hurdles of the previous lithography methods, a new lithography method which can provide smaller feature size in a low cost way is badly needed. In the meanwhile, thermoplastics are being used increasingly for patterning in recent years [116]. There are several advantages of thermoplastics including better mechanical

rigidity, superior resistance to organic solvents, easier and more persistent surface modification, and less nonselective absorption of hydrophobic molecules [117]. Thermoplastic film with a pattern on its surface provides another way to obtain smaller structures. The shape of the thermoplastic film can be controllably changed by turning the external temperature. The patterns directly transferred onto the thermoplastic will be simultaneously shrunk to get smaller feature size. Yokoo *et al.* [118] developed a pattern fabrication process onto a heat shrinkable film based on nanoimprint lithography. After pattern transferring by nanoimprint, the shrink film is shrunk by heating. Simultaneously, the pattern on the film can be shrunk. 60 nm feature size of pattern was successfully achieved by this method. Alternative lithography approaches have also been developed to pattern thermoplastic substrates in order to decrease the cost. Grimes *et al.* reported a low cost and simple method for fabrication of microfluidic devices by utilizing polystyrene [119]. Lee *et al.* developed the process of solvent-assisted nanoscale embossing (SANE) to fabricate arrays that could be utilized for fabrication of biosensors in the future [120]. In their method, PDMS was against the mold with hexagonal array of posts to generate PDMS molds. The PDMS mold was then treated with a solvent before uniformly contact with photoresist on silicon wafer. Another method that was used to fabricate new arrays with higher densities was performed by wetting the PDMS mold with photoresist and then using a convection oven to heat the patterned resist with shrink film, which helped with reducing the separation between the features. Furthermore, in order to increase the spacing between the features, the thermoplastic could also be mechanically stretched. Then the stretched master could be molded again with PDMS,

and then SANE methods were applied to fabricate metallic nanoparticle arrays and the spacing between the particles was tuned by varying the shrinking time of the polymer. The ability to control these metallic nanostructures can be utilized for fabrication of plasmonic biosensors.

### 5.2 Thermoplastic Shrink Lithography and Its Applications

Thermoplastics are attracting more and more attention in micro fabrication in recent years. Depending on resin selection and blend proportion, these thermoplastics can shrink by varying amounts when heat is applied. Molding is a low cost and high throughput mean to replicate functional and artisanal patterns. However, the molds are very expensive to create and control at nanoscale dimensions. Herein, shrink lithography combines the thermoplastic film with molding process to successfully achieve 21 nm metal lines and large scale array patterns. In addtion, using shrink lithography, a suspended graphene nanoribbon biosensor was fabricated, demonstrating that shrink lithography has the potential to become a commerically viable lithography for the manufacture of nano scale structure.

The procedure of shrink lithography is outlined in Fig. 5.1a. First, a cleaned silicon wafer with $SiO_2$ 300 nm thick was patterned by photolithography with photoresist of Shipley S1813 spin-coated at 3,000 rpm for 30 s and exposed for 6 s, followed by buffered HF (BOE 10:1) etching for 7 minutes. Next, the patterned wafer was etched by 20% KOH at 80°C for 10 minutes, and the $SiO_2$ was the passivation layer. In order to impenetrate the shrink film, an additional KMPR (MicroChem Inc.) layer around the patterns was deposited. Next, chromium/gold layers 50/50 nm thick as a seed layer were deposited on

the substrate by an AJA sputter system (Model ATC 2000). Nickel electroforming was conducted on a nickel plating station (SE-101, Digital Matrix Co., U.S.) using the patterned wafer as mandrel. A nickel sulfamate bath and a pulse reverse power were used to obtain uniform and stress free nickel mold. After electroplating, the silicon wafer was completely removed by 20% KOH at 80°C. The obtained nickel mold was further cleaned by acetone and de-ionized water.

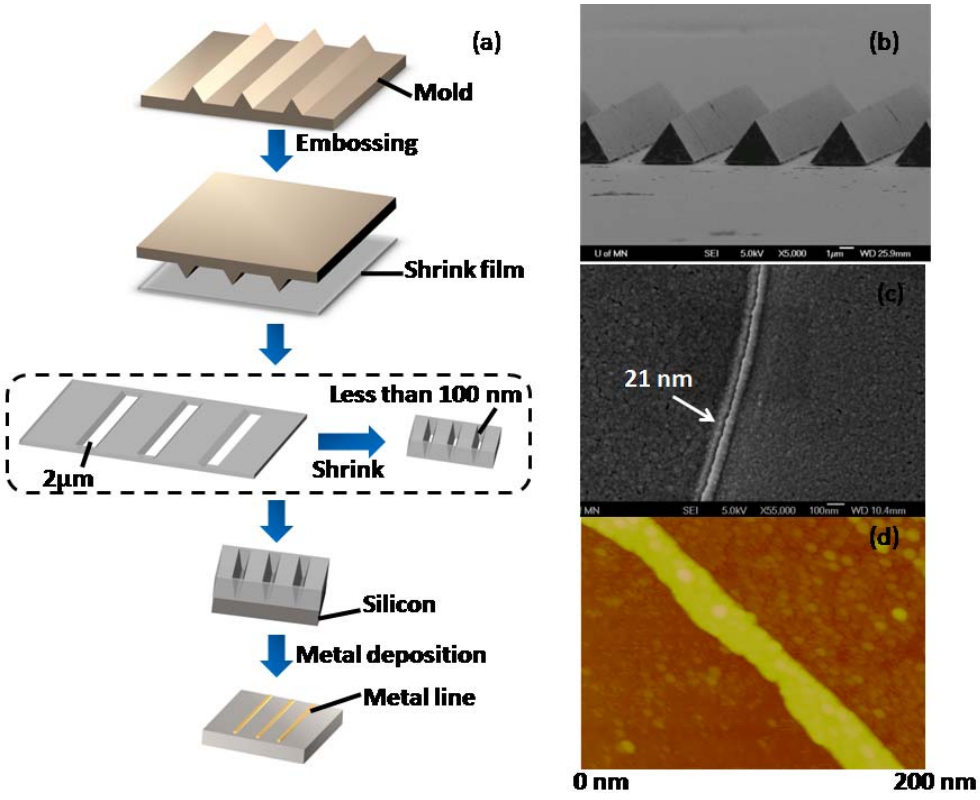


Figure 5.1 (a) Sketch of shrink lithography processes. The shrink lithography uses embossing molding method to pattern the shrink film, and thermally shrink the film as a shadow mask subsequently. Metal patterns are obtained by sputtering. SEM images of (b) mold and (c) 21 nm line. (d) AFM image of 21 nm line.

After preparation of the mold (Fig. 5.1b), it was embossed against the shrink film and held for 2 minutes by Maual Pressor (Model Grimco 12-1-HT). The shrink film (Sealed Air Nexcel multilayer shrink film 955D) comprising of 5 layers of co-extruded polyolefin (PO) was purchased from Sealed Air. Next, release the mold, and PO shrink film with impenetrated patterns was made. Sequencially, the patterned PO shrink film was placed between two silicon wafers for uniform heating, and heated to desird temperature in a slowly rising process for approximately 5 minutes and held for 10 minutes for shrinkage in a convection oven (Model 280A). Due to the adhesion of shrink polymer film at high shrink temperature, the PO shrink film bonded with silicon very well, as the shadow mask for metal deposition. Finally, chrome was depostied on the substrate by sputtering. As is shown in Fig. 5.1c and d, a 21 nm line pattern was fabricated by this shrink lithography.

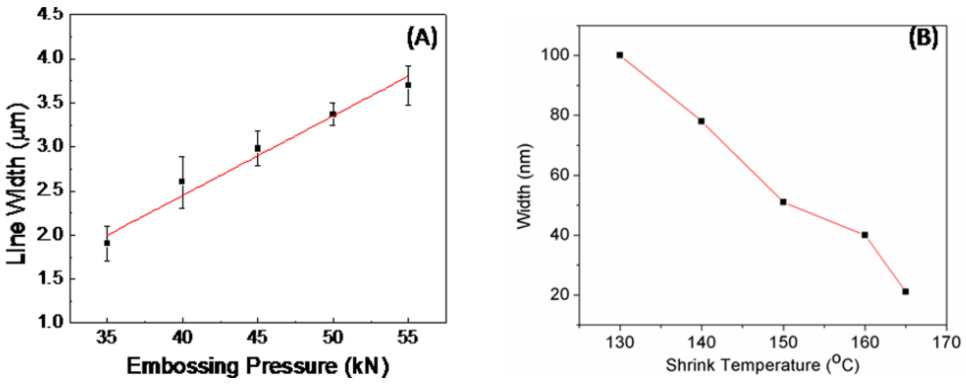


Figure 5.2 (a) Shift in line width versus embossing pressure for shrink lithography. Width of the lines raises with the increase of embossing press when the operating temperature is controlled at room temperature. (b) Line width versus shrink temperature under the condition of controlling the embossing press at 50 kN. Width of the metal lines decreased with the rising of the temperature.

In the meanwhile, most current molding methods have a common goal that is to generate replicas of the molds. Therefore, if different features of pattern are desired, new molds are necessary to create for every new pattern, which is very high cost. However, shrink lithography is capable of generating various feature sizes of patterns from a single mold according to a control of the embossing pressure and shrink temperature conditions. Therefore, the material and shrinkage properties of these films are characterized under different embossing pressure and shrink temperatures. As shown in Fig. 5.2a, the width of the grooves embossed by the mold raises with the increase of embossing press when the operating temperature is controlled at room temperature. SEM images of these samples were taken and demonstrated this trend clearly in Fig. 5.3. Besides, by controlling the embossing press at 50 kN, the width of metal lines fabricated by shrink lithography from the same mold were characterized at different shrink temperatures. As is shown in Fig. 5.2b, the width of the metal lines decreased with the rising of the temperature. SEM images of these samples were taken and demonstrated this trend clearly in Fig. 5.4.

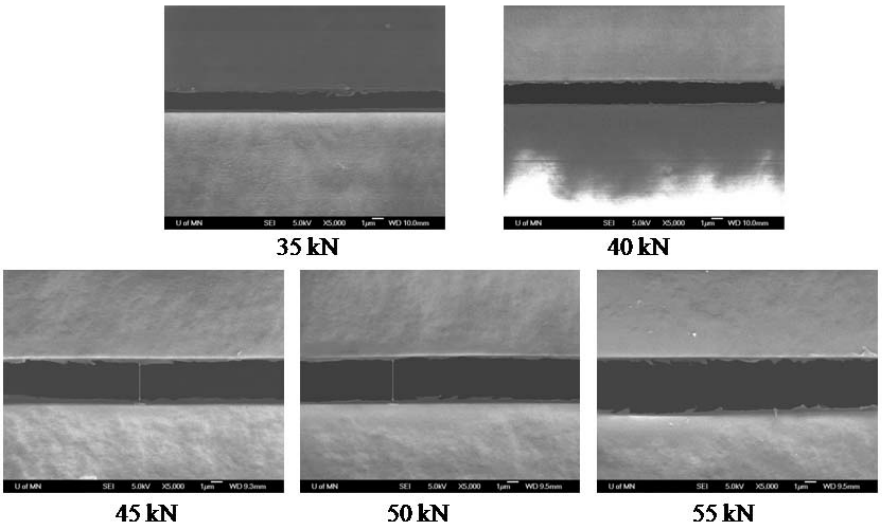

Figure 5.3 SEM images of the grooves embossed by the mold with the increase of embossing press when the operating temperature is controlled at room temperature.

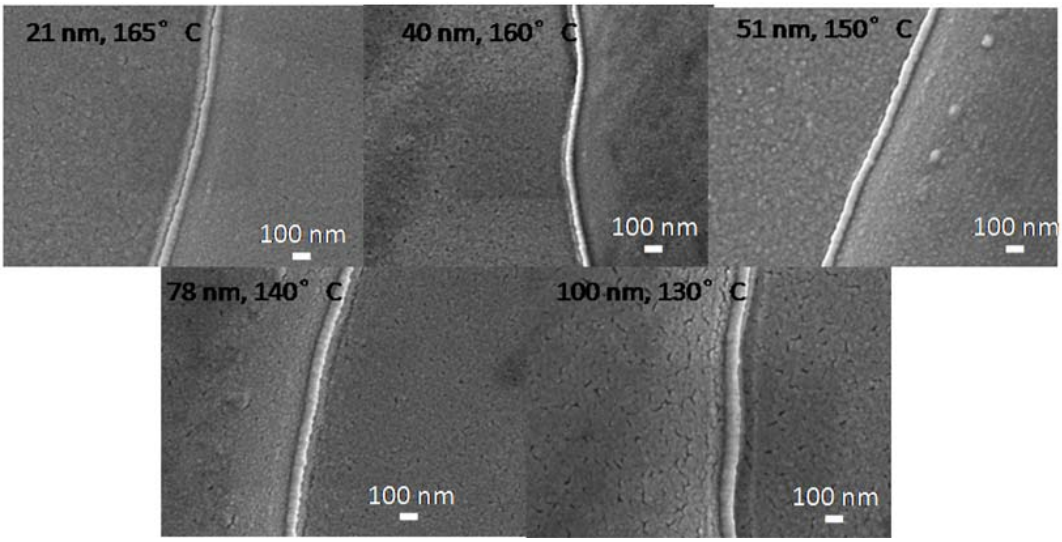


Figure 5.4 SEM images of the metal lines fabricated by shrink lithography from the same mold at different shrink temperatures.

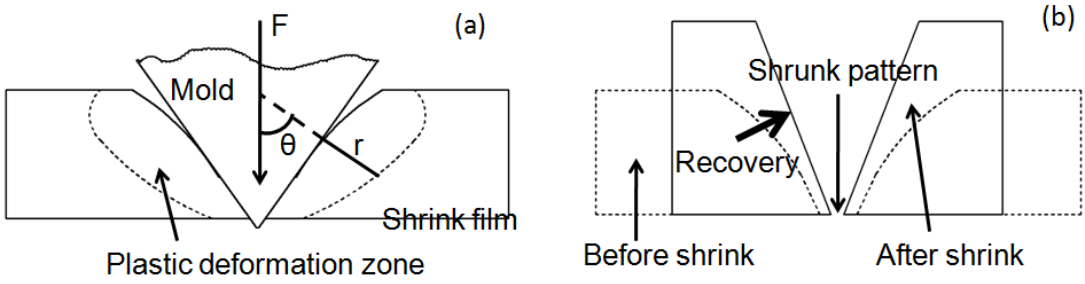


Figure 5.5 (a) A load on the mold positioned onto the shrink film causes local plastic deformation below the tips around. (b) The recovery of shrink film will decrease the width of the patterns greatly.

As reported in the previous literature, the PO shrink films can shrink reproducibly up to 95% in area. However, our shrinkage results are from several micrometer down to sub-100 nm level, which is much larger. The reason is that the thermal recovery property of

PO shrink film enhances the shrinkage of impenetrated patterns. As is shown in Fig. 5.5a, applying a load on the mold positioned onto the PO shrink film will initially cause local plastic deformation below the tips around cutting wedge of impenetrated patterns. This deformation depends on the load necessary for indentation, the elastic modulus of shrink film and the local shear stresses under the wadge [121]. Based on the appropriate boundary conditions, a general solution for linear elastic stresses supporting the applied cutting force yields a solution for shear stress τ:

$$\tau = -\frac{F\cos\theta}{\pi r}$$

Where $F$ is the wedge force per unit thickness, $r$ is the distance from the wedge to the point under consideration, and $\theta$ is the angle measured from the direction of the force [122]. If these shear stresses exceed the shear strength of shrink film, delamination will occur [123]. Thus, the plastic deformation zone size R can be derived from the equation above with r=R. Due to the thermal recovery property of PO shrink film, the matter squeezed aside next to the wedge will attend to recover to its initial shape before embossing when heat is applied. As is shown in Fig. 5.5b, this recovery of PO shrink film will sharpen the grooves width greatly, combining with the intrinsic shrinkage of PO film, to offer the extremely large shrink ratio.

Graphene nanoribbon patterned from shrink lithography were also successfully used to fabricate suspended PSA cancer biosensor, revealing the practical application potential of this shrink lithography. With the shrink lithography technique, the shrunk ultra-narrow patterns were transferred to the graphene fabricated by mechanical exfoliation. The graphene nanoribbons were generated at a level of 50 nm width. We started with a

graphene plate genearated by mechanical exfoliation method on a $SiO_2$/Si wafer. A photoresist layer (Shipley S1818) was used as a transfer stamp to exfoliate graphene patterns from highly oriented pyrolytic graphite (HOPG), and transferred patterns onto a $SiO_2$/Si substrate. First, patterns in microscale were formed on the surface of HOPG by photolithography followed by an oxygen plasma etching with STS etcher (Model 320, 30 seconds). A layer of S1818 was spun on the pre-treated HOPG, and a thermal releasing tape was used to gently peel graphene flakes off, and transferred them onto the $SiO_2$/Si substrate. The substrate was pre-patterned with marks for the alignment and location. Photoresist was removed by acetone later.

By using shrink lithography, extreme narrow impenetrated pattern was obtained on the PO shrink film. A layer of $Al_2O_3$ 8 nm thick was depostied, and the shrunk PO film was acting as shadow mask. Next, the PO film was stripped, and a $Al_2O_3$ nanoribbon left on the graphene as the mask. The substrate was followed by oxygen plasma etching with STS etcher (Model 320, 10 seconds). The masks on the substrate assisted the alignment and location. After that, the substrate was immersed into KOH solution to remove the $Al_2O_3$ mask. Next, chromium/gold electrodes 50/200 nm thick were deposited on the two ends of grapheme nanoribbon by an electron-beam evaporation (Model SEC 600), and metal lift-off. The $SiO_2$ layer 300 nm thick underneath graphene ribbons was etched away by buffered HF (BOE 10:1) for 7 minutes. The suspended structure was obtained by super critical dryer (Fig. 5.6c and 5.6d).

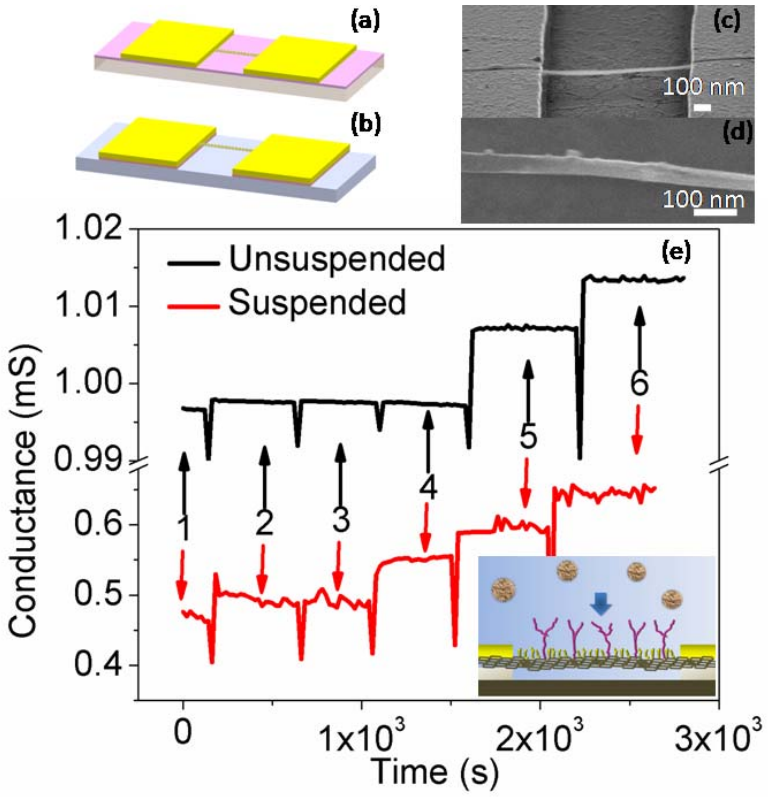


Figure 5.6 Sketches of (a) unsuspended and (b) suspended graphene nanoribbon. (c) SEM images of suspended grapheme nanoribbon. (d) High magnitude SEM image of graphene nanoribbon. (e) The detection limit results of graphene nanoribbon based biosensor in both suspended (lower curve) and unsuspended (upper curve) situations. Conductance versus time data recorded after alternate delivery of the following concentrations of PSA: (1) PBS contains no PSA, (2) 0.1 pg/ml, (3) 1 pg/ml, (4) 10 pg/ml, (5) 1 ng/ml, (6) 1 μg/ml. inset: the illustration of PSA sensing mechanism, where the graphene nanoribbon is modified with PSA antibody receptors. PSA bonded specifically to receptors will produce a conductance change of the graphene nanoribbon.

Next, anti-prostate specific antigen (PSA) antibodies as bioreceptors were immobilized on the graphene nanoribbon to test the PSA. After the suspension of grapheme

nanoribbon, the biosensor was functionalized by immobilization of antibody on the surface. Due to the surface tension of water, the modification process was executed in aqueous solution all the time to keep the suspension structure. A suspended graphene nanoribbon sensor was first immersed into a 0.1% poly-l-lysine (Sigma–Aldrich Inc.) solution for 1 hour. Next, the biosensor was incubated for overnight at 4 ºC in anti-PSA capture antibody solution (BioCheck Inc.) at a concentration of 10 μg/ml prepared by a dilution into PBS (Dulbecco's phosphate buffered saline, Invitrogen Inc.). The sensor was then immersed in a PBS solution for 10 minutes to rinse the biosensors. Next, the sensor was incubated in 3% bovine serum albumin blocking solution (Sigma–Aldrich Inc.) at room temperature for 5 hours to block nonspecific binding sites. After repeating the rinsing step, the label free sensor was ready for testing.

The detection mechanism of the biosensor are illustrated in the inset of Fig. 5.6e. Given that the conductance of graphene is proportional to the product of charge carrier density and mobility, it is believed that changes in density and/or mobility of charge carriers must be responsive when PSA are captured by the antibodies modified on a graphene nanoribbon. The equation, $\sigma = nq\upsilon$ , can show the relationship clearly, where σ is conductance, n is carrier density, q is charge per carrier, and υ is the carrier mobility. As is shown in Fig. 5.6e, the conductance-versus-time measurements recorded on the graphene nanoribbon biosensor in both suspended and unsuspended situations demonstrated the good perfermance of detection of PSA. The suspended biosensor showed better detection limits (1pg/ml) than the unsuspended one (10 pg/ml) due to the enhanced signal to noise ratio in the suspended graphene.

## 5.3 Hydrogel Shrink Lithography and Its Applications

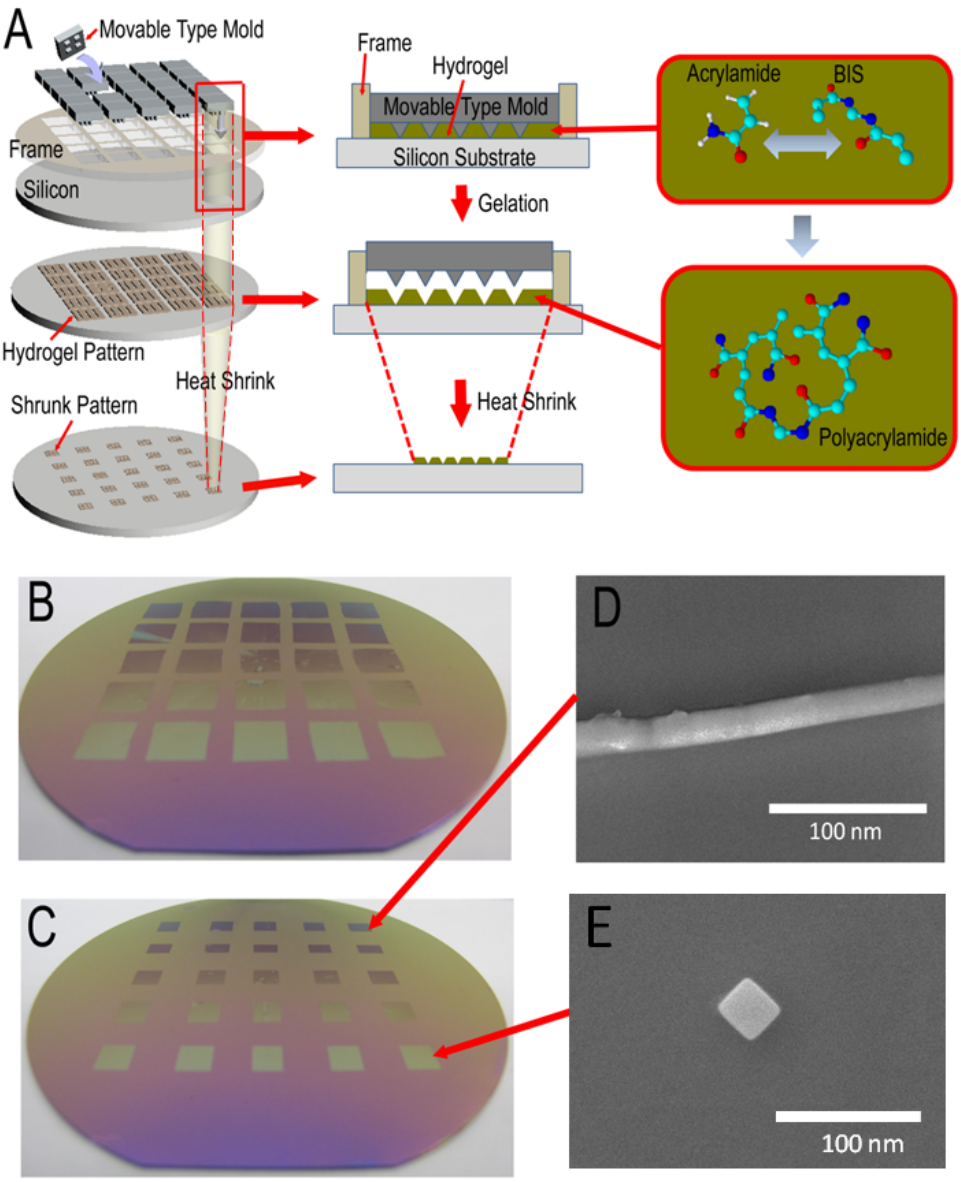


Figure 5.7 (a) Schematic illustration of basic concept of movable type shrink lithography. Optical image of wafer scale pattern array (b) before shrink and (c) after shrink. Different patterns including (d) line with 20 nm width and (e) dot with 20 nm diameter were achieved on the same wafer substrate by simply using different sub-molds.

Hydrogel has been involved in micro fabrication in recent years [124]. Depending on components, blend proportion, the hydrogel can hold more than 50% (v/v) water and shrink by various amounts when heat is applied, resulting in a nearly isotropic and crack-free shrinkage. Inspired by movable type , the system of printing and typography that uses movable components to reproduce the elements of a document invented in China around 1040 A.D. during the Song Dynasty, it was demonstrated here that movable type shrink lithography combines the hydrogel with movable type process to successfully achieve 20 nm feature size and wafer scale pattern arrays, showing that this shrink lithography has the potential to become a commerically viable lithography for the manufacture of nanoscale structure. The process of movable type shrink lithography proposed here does not involved any high cost nanofabrication method such as electron beam lithography. By controlling the shrink temperature and altering the movable dies of the modular mold, the movable type shrink lithography can achieve arbitrary patterns without fabricating extra molds.

The basic concept of movable type shrink lithography is outlined in Fig. 5.7a.

As shown in Fig. 5.8, a set of modular mold containing thousands of pyramid-shaped tips was firstly fabricated by conventional photolithography and KOH etching. First, a cleaned silicon wafer with $SiO_2$ 300 nm thick was patterned by photolithography with photoresist of Shipley S1813 about 1 μm thick spin-coated at 3,000 rpm for 30 s and exposed for 6 s, followed by buffered HF (BOE 10:1) etching for 7 minutes. Next, the patterned wafer was etched by 20% KOH at 80°C for 10 minutes, and the $SiO_2$ was the passivation layer. After the patterns were generated on the wafer, the substrate was

immersed into buffered HF to remove $SiO_2$ passivation layer. In order to obtain the 1 cm by 1 cm movable type sub-molds, wafer saw (Model: Disco DAD 2H/6T) were used to cut the patterned silicon wafer.

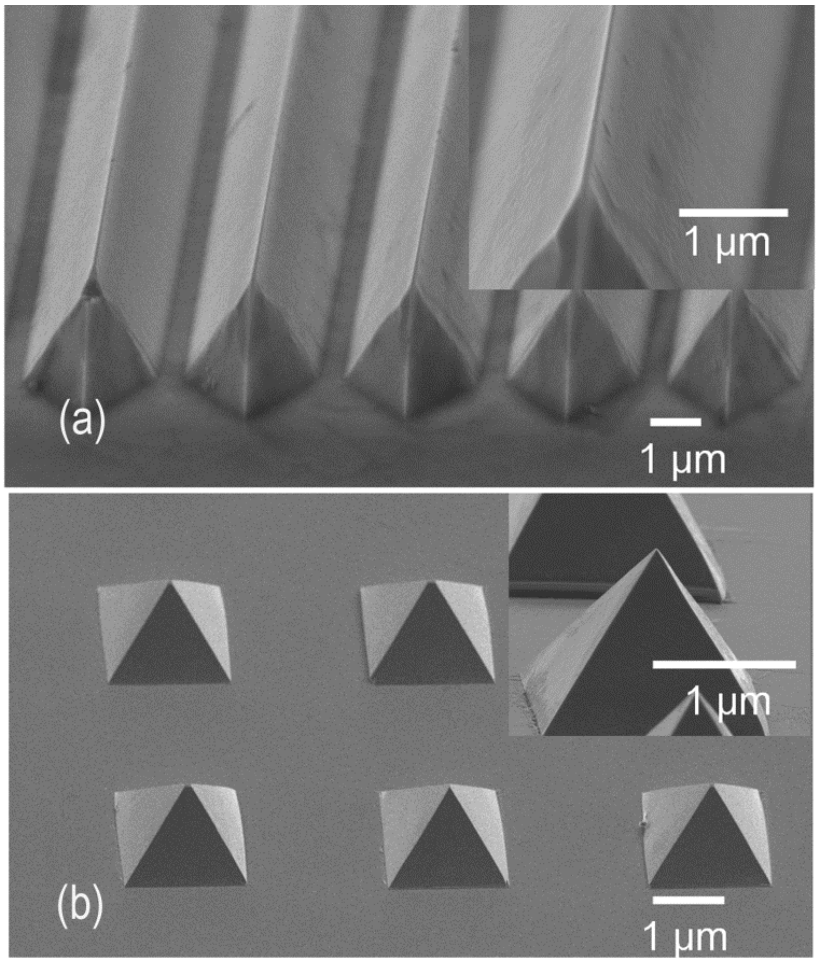


Figure 5.8 SEM image of different sub-molds including (a) line arrays and (b) dot arrays.

Hydrogel was synthesized by the polymerization of acrylamide and bis-acrylamide ("bis," N,N'-methylene-bisacrylamide) in pH 7 buffer solution, in the presence of basic catalysts: ammonium persulfate (Sigma-Aldrich Inc.) and TEMED (tetramethylethylenediamine, Sigma-Aldrich Inc.). 6.8 ml 30% 19:1 acrylamide and bis acrylamide solution (Sigma-Aldrich Inc.) was added to pH 7 buffer solution and stirred

for 15 min. An aqueous solution of 100 μl 10 mg/ml ammonium persulfate and 6 μl TEMED were then added and the mixture was stirred for 5 min at room temperature.

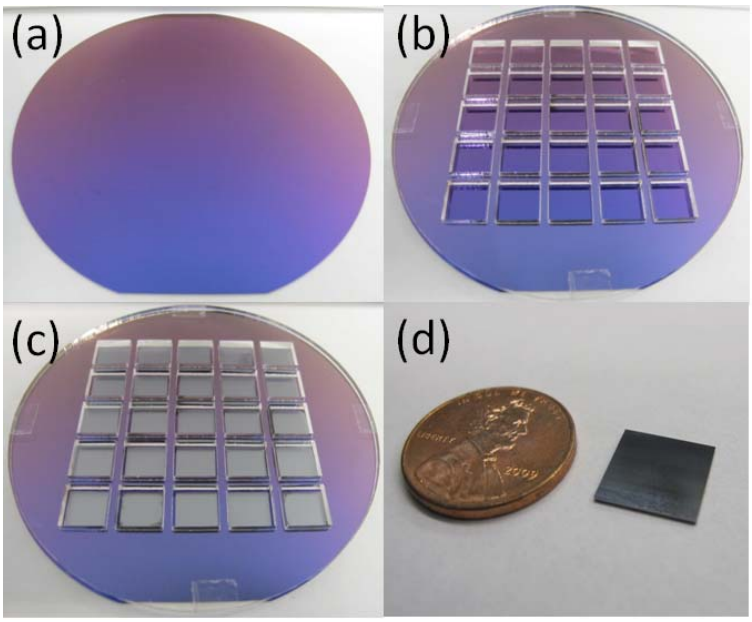


Figure 5.9 (a) Optical image of $SiO_2$/Si wafer substrate. (b) Frame fabricated by laser cutting machine was fixed on top of substrate. (c) Movable type sub-molds were assembled with the frame. (d) Optical image of individule sub-mold.

The frame was fabricated by laser cutting machine, and assembled with substrate and sub-molds, as shown in Fig. 5.9. Then, the gel precursor solution was poured onto this molding area confined by frame and was allowed to polymerize for about 30 minutes. The inert atmosphere was maintained by purging $N_2$ gas during the polymerization process at the room temperature. After gelation, release the mold, and hydrogel film with impenetrated patterns was made. Sequencially, the substrate with patterned hydrogel film was placed in a convection oven (Model 280A) for uniform heating, and heated to desird temperature in a slowly rising process for approximately 5 minutes and held for 10

minutes for shrinkage. Finally, metal was depostied on the substrate by sputtering. After striping the hydrogel film, various nano patterns were obtained.

As shown in Fig. 5.7b and c, the wafer scale pattern array can be generated and shrunk. The shrunk patterned hydrogel acted as a shadow mask for metal depositon, and the shrunk nanoscale line arrays are transferred from the hydrogel film to the substrate. Most current molding methods have a common goal that is to generate replicas of the molds. Therefore, if different features of pattern are desired, new molds are necessary to create for every new pattern, which is very high cost. However, movable type shrink lithography is capable of generating different feature sizes of patterns by assemblying different modular molds. According to the confinement of frame, the molds are movable to achieve different patterns without extra molds. By using modular mold in movable type shrink lithography, numerous permutations and combinations of duplicates can be molded with little efforts. As shown in Fig.5.7 d and e, different nanopatterns can be achieved on the same wafer substrate by simply using different sub-molds. Besides, the feature size can also be adjusted from single mold according to control the embossing pressure and shrink temperature conditions. And the cost of the hydrogel material in most cases is negligibly low.

The hydrogel, as a class of materials that can hold large volumes of water, plays the cirtical role in movable type shrink lithography. According to the previous research, the hydrogel has shown large shrink in volume in response to changes in the environmental conditions, such as pH, ionic strength, temperature, electric field, and light. As shown in Fig. 5.7a, hydrogels are formed by polymerization reaction of acrylamide and bis-

acrylamide ("bis," N,N'-methylene-bisacrylamide) initiated by by ammonium persulfate and TEMED (tetramethylethylenediamine): TEMED accelerates the rate of formation of free radicals from persulfate and these in turn catalyze polymerization. The persulfate free radicals convert acrylamide monomers to free radicals which will react with inactivated monomers to begin the polymerization chain reaction. The elongating polymer chains are randomly cross linked, resulting in a gel depending on the polymerization conditions and monomer concentrations. Herein, we pay more attention to the temperature response of hydrogel during the shrink lithography. Hydrogel with a through pattern on its surface provides a way to obtain smaller structures, which is different from most conventional molding methods that is to generate replicas of the molds. By applying heat, any patterns on the hydrogel will shrink. Then, it can obtain a final pattern that has a smaller pitch than the initial pattern fabricated on the mold.

Besides the assembly of modular molds, the movable type shrink lithography is also capable of generating various patterns from single mold according to controlling the shrink temperature conditions. Therefore, if different features of pattern are desired, new molds are not required for every new pattern, which is very low-cost. The shrinkage properties of hydrogel are characterized at different shrink temperatures. As shown in Fig. 5.10, SEM images of nanopatterns generated by shrink lithography were taken and demonstrated the inverse relationship between feature size of patterns and shrink temperature. By controlling the shrink temperature from 50°C to 150°C, the width of metal lines fabricated by shrink lithography from the same mold were decreased with the rising of the temperature. The diameter change of nanodots corresponding to shrink

temperature also confirmed with this trend. The quantitively characterization of the feature size of patterns versus shrink temperature was presented in Fig. 5.11a.

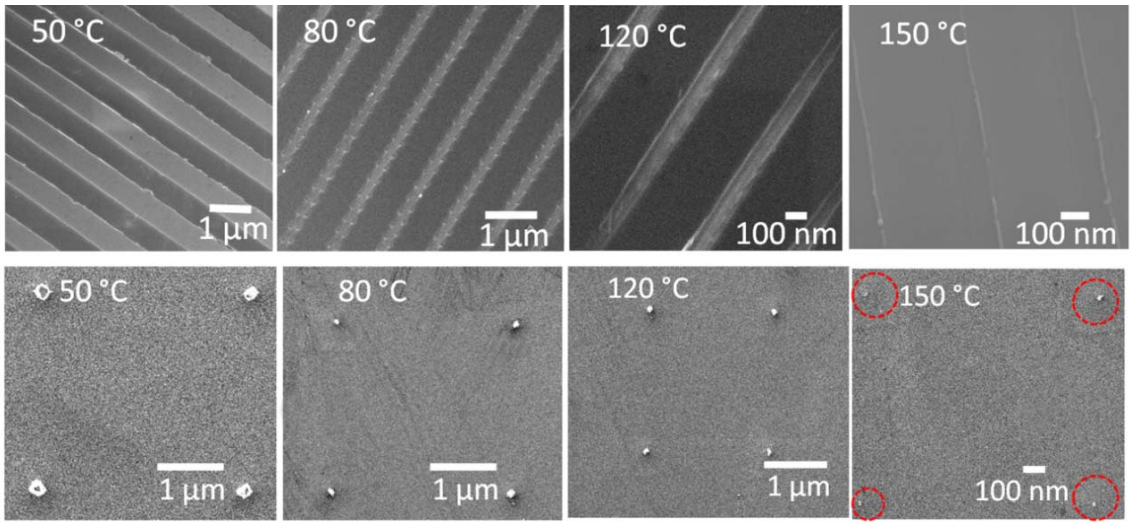


Figure 5.10. SEM images of nanopatterns generated by shrink lithography from the same mold were taken and demonstrated the inverse relationship between feature size of patterns and shrink temperature.

The hydrogel is a suitable nanofabrication material for shrink lithography: the hydrogels can hold high volume water content and thus their drying under controlled conditions results in a significant size reduction by a nearly isotropic and crack-free shrinkage of the gel. In order to investigate the relationship between shrinkage and temperature, the thermo gravimetric analysis of hydrogel was shown in Fig. 5.11b. Hydrogel was dried in a convection oven by gradually increasing the temperature from the room temperature to different temperatures. The water loss increased along with the increasing of the shrink temperature.

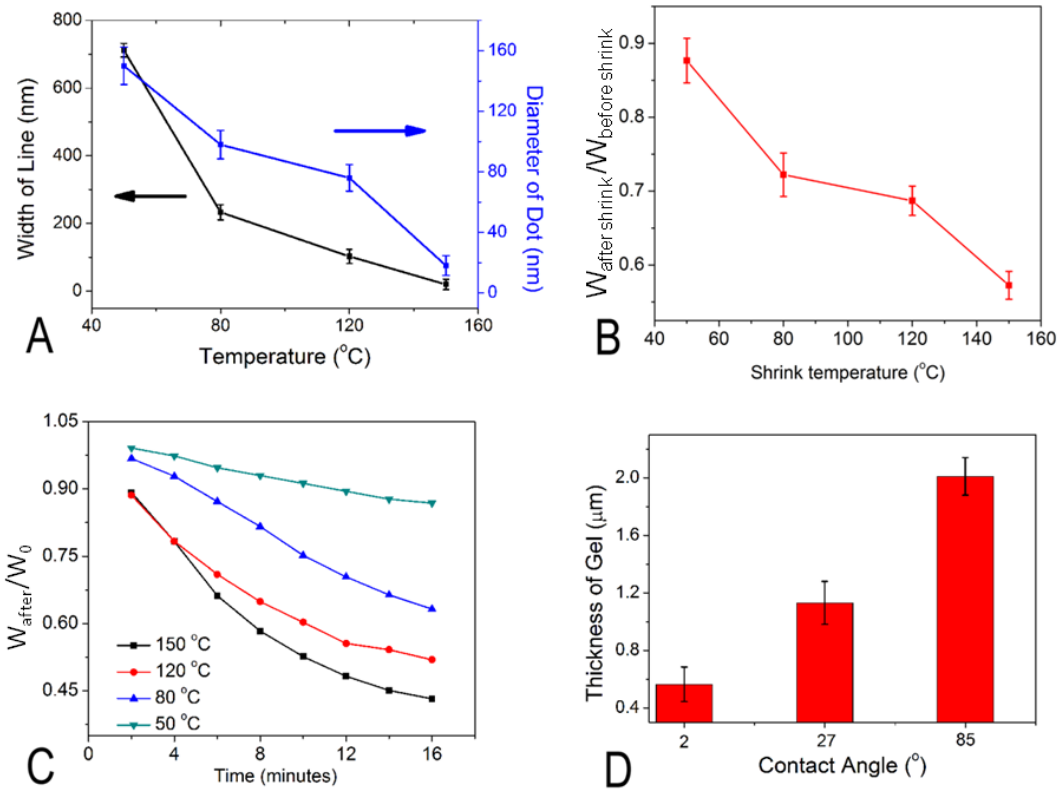


Figure 5.11 (a) The width of lines and the diameter change of dots fabricated by shrink lithography from the same mold were decreased with the rising of the shrink temperature. (b) Thermo gravimetric analysis of hydrogel. The weight of sample after shrinking to the weight of sample before shrinking ratio decreases along with the increasing of shrink temperature. (c) Real time record of thermo gravimetric testing. $W_0$ is the initial weight. (d) The thickness of hydrogel can be tuned by adjusting the surface wetting ability of substrate.

The weight shift versus time curves were also recorded at different shrink temperatures, as shown in Fig. 5.11c. In addtion, the thickness of the hydrogel film can be tuned according to adjusting the substrate surface wetting ability. As shown in Fig. 5.11d and 5.12, the thickness of hydrogel film will increase along with the increasing of contact

angle of substrate surface. The hydrophilic surface will offer thinner hydrogel film formation. Thinner hydrogel film will have higher successful chance to fabricate extremely small feature size of patterns due to the aspect ratio limitation.

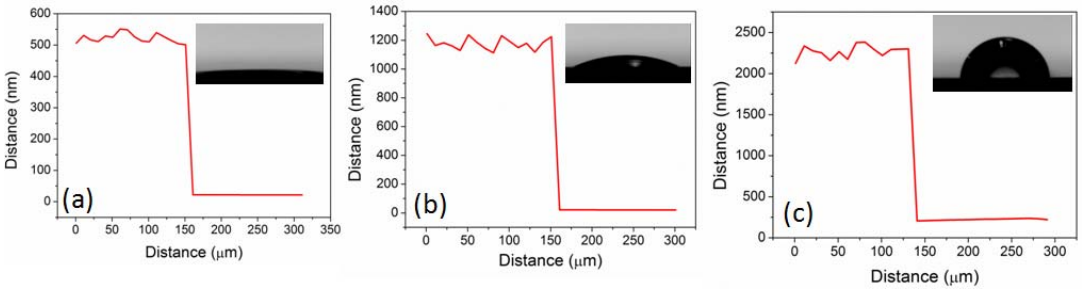


Figure 5.12 The thickness of hydrogel can be tuned by adjusting the surface wetting ability of substrate. The step measurement of hydrogel film thickness on different substrate with different surface wetting abilities: (a) contact angle 2°, (b) contact angle 27° , (c) contact angle 85° .

In addition, the shrink lithography can also generate large scale nano patterns with one entire mold. As shown in Fig. 5.13, 2 inch by 2 inch nanoribbon array patterns were generated by this shrink lithography with only one 4 inch by 4 inch mold. The sub-mold size can be adjusted from 1 $cm^2$ to 16 $inch^2$, showing much larger potential pattern area.

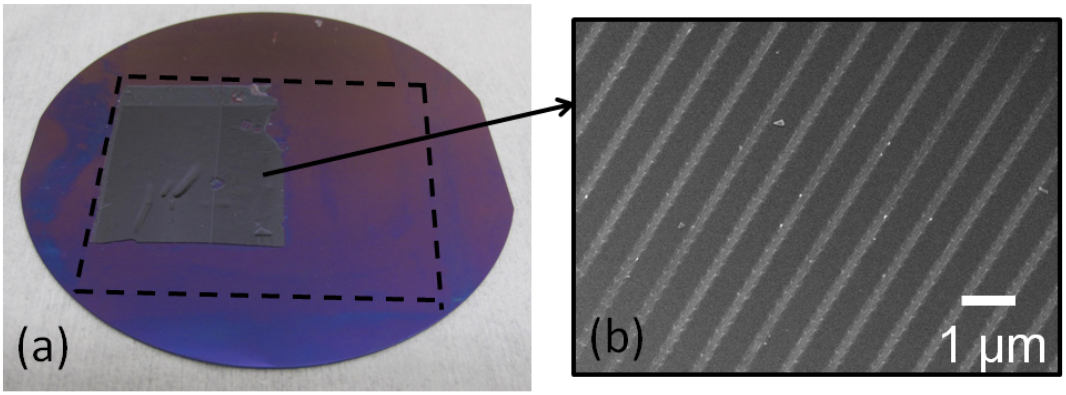

Figure 5.13 (a) Optical image of large-scale shrunk hydrogel film with line array patterns. The black dash line area is the original hydrogel area before shrink. (b) SEM of line array patterns.

As proof of concept, suspended graphene nanoribbon arrays were successfully generated by movable type shrink lithography. Suspended graphene nanoribbon arrays were used to fabricate PSA biosensor, revealing the potential practical application of this shrink lithography. The ultra-narrow line array patterns, at a level of 100 nm in width, were patterned by the shrink lithography technique on the microscale graphene fabricated by mechanical exfoliation.

We started with a microscale graphene plate genearated by mechanical exfoliation method on a $SiO_2$/Si wafer. Next, by movable type shrink lithography process, the hydrogel film with extreme narrow impenetrated pattern was obtained as a shadow mask on the top of graphene. Then, a layer of $Al_2O_3$ 8 nm thick was depostied by atomic layer deposition, and the hydrogel film was acting as shadow mask. Next, the hydrogel film was stripped, and a $Al_2O_3$ nanoribbon array left on the graphene as the mask. The substrate was followed by oxygen plasma etching with STS etcher (Model 320, 10 seconds). After that, the substrate was immersed into KOH solution to remove the $Al_2O_3$ mask. Next, chromium/gold electrodes 50/200 nm thick were deposited on the two ends of grapheme nanoribbon array by an electron-beam evaporation (Model SEC 600), and metal lift-off. The $SiO_2$ layer 300 nm thick underneath graphene ribbons was etched away by buffered HF (BOE 10:1) for 7 minutes. The suspended structure was obtained by super critical dryer (Model 915 B), as shown in Fig. 5.14b.

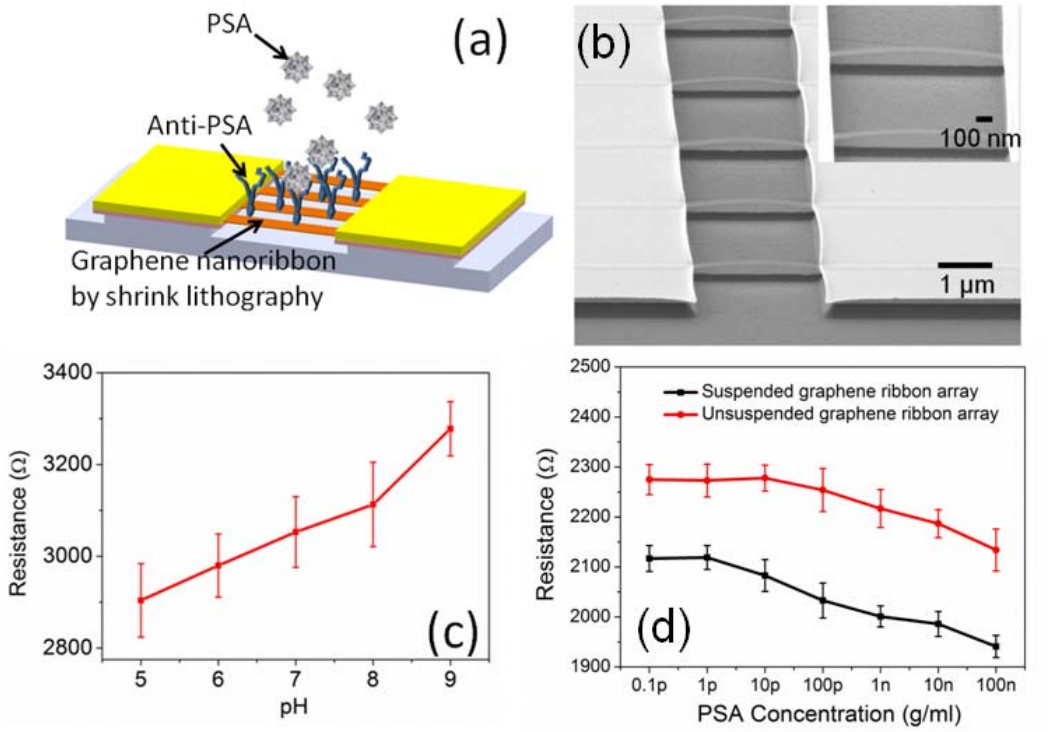


Figure 5.14 (a) Sketch of suspended graphene nanoribbon array based biosensor for PSA testing. The immunoreactions between PSA and anti-PSA result in the decrease of graphene nanoribbon array resistance. (b) SEM images of suspended graphene nanoribbon array. The width of the ribbon is about 50 nm. (c) The graphene nanoribbon biosensor was characterized by pH measurements. (d) Different concentrations of PSA solutions were introduced to both the suspended and unsuspended graphene nanoribbon biosensors. The suspended biosensors demonstrated better detection limit than the unsuspended biosensors.

After the suspension of grapheme nanoribbon array, the biosensor was functionalized by immobilizing of antibody on the surface. Due to the surface tension of water, the modification process was executed in aqueous solution all the time to keep the

suspension structure. A suspended graphene nanoribbon sensor was first immersed into a 0.1% poly-l-lysine (Sigma–Aldrich Inc.) solution for 1 hour. Next, the biosensor was incubated for overnight at 4 ºC in anti-PSA capture antibody solution (BioCheck Inc.) at a concentration of 10 μg/ml prepared by a dilution into PBS (Dulbecco's phosphate buffered saline, Invitrogen Inc.). The sensor was then immersed in a PBS solution for 10 minutes to rinse the biosensors. Next, the sensor was incubated in 3% bovine serum albumin blocking solution (Sigma–Aldrich Inc.) at room temperature for 5 hours to block nonspecific binding sites. After repeating the rinsing step, the label free sensor was ready for testing.

As shown in Fig. 5.14c, different pH buffer solutions were introduced onto the graphene nanoribbon sensor, and the resistance shift of graphene nanoribbon array was monitored by the Agilent Data Logger (34970A, Agilent Inc.). Given that the resistance of graphene is proportional to the product of charge carrier density and mobility, it is believed that changes in density and/or mobility of charge carriers must be responsive when different pH solutions are introduced.

Finally, anti-PSA antibodies as bioreceptors were immobilized on the suspended graphene nanoribbon arrays for the testing of PSA. The detection mechanism of the PSA biosensor is illustrated in Fig. 5.14a. The surface charge of graphene nanoribbon will be changed when PSA are captured by the antibodies modified on a graphene nanoribbon, resulting in the resistance change of graphene nanoribbon. As is shown in Fig. 5.14d, the resistance measurements recorded on the graphene nanoribbon array biosensor in both suspended and unsuspended situations demonstrated the good perfermance of detection

of PSA. The suspended biosensor showed better detection limits (1pg/ml) than the unsuspended one (10 pg/ml) due to the enhanced signal to noise ratio in the suspended graphene.

### 5.4 Application of Shrink Induced Nanostructures to Biosensing

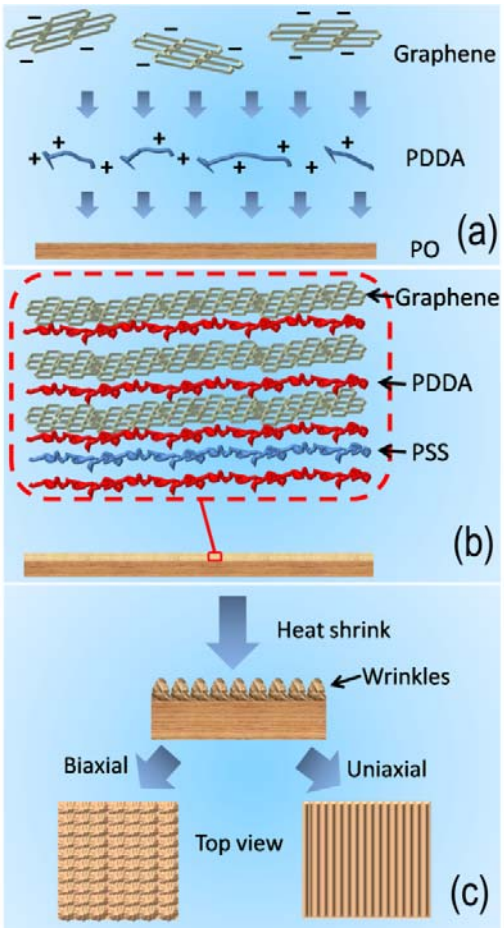


Figure 5.15 Schematic illustration of synthesis of the shrink induced graphene composites. (a) LbL self-assembly of graphene nanoplatelets on the PO substrate. (b) The structure of the LbL self-assembled graphene layers. (c) Heat shrink of the PO substrate, and the tunable wrinkles were generated.

A tunable shrink induced graphene composites with a heat shrink film as the substrate, use self-assembly technique to deposit the graphene nanoplatelets. Different from the conventional graphene composites structures with fixed properties, this proposed graphene composites are tunable and controllable on the resistance and surface nanowrinkles due to heat shrink of the substrate at different temperature. This shrink induced graphene nanowrinkles of tunable size can affect the sensitivity of the sensors based on this graphene composites and the surface wetting ability of the graphene composites.

The fabrication processes of the graphene composites are illustrated in Fig. 5.15. Two types of shrink mechanism including biaxial and uniaxial shrinkage were investigated according to applying different boundary conditions. First of all, the graphene nanoplatelets were LbL self-assembled on the heat shrink film. The shrink film (Sealed Air Nexcel multilayer shrink film 955D) comprise 5 layers of co-extruded PO. The substrate was immersed into the charged suspensions with a sequence of [poly(diallyldiamine chloride) (PDDA) (10 min) + poly(styrene sulfonate) (PSS) (10 min)]$_2$ + [PDDA (10 min) + graphene suspension (20 min)]$_5$. The polyelectrolytes used in self-assembly were purchased from Sigma–Aldrich Inc. The concentrations of aqueous PDDA and PSS were 1.5 and 0.3 wt%, respectively, with an addition of 0.5 M sodium chloride to enhance the surface properties. Research grade graphene (PureSheets$^{TM}$, 0.25 mg/ml) suspension solution was purchased from Nanointegris Inc. Subsequently, in order to obtain biaxial nanowrinkles, the PO shrink film coated with self-assembled graphene was placed between two silicon wafers for uniform heating, and

heated to desird temperature in a slowly rising process allowing approximately 5 minutes and held for 10 minutes for shrinking in a convection oven (Model 280A). During the shrink process, there were no fixed boundary conditions applied at the edges of PO shrink film. Due to the stiffness mismatch of materials, the shrunk PO material substrates induces the stiffer, nonshrinkable self-assembled graphene film to buckle at different shrink temperature. This can controllably create nanoscale graphene wrinkles, which is very critical in introducing the tunable strategy. To fabricate uniaxial nanowrinkles, fixed boundary conditions were applied at the edges of PO shrink film when heats were introduced. During the shrink process, two edges of a PO shrink film were clamped by clips (2 inch binder clips; OfficeMax) to ensure it could only shrink in one direction while the other one is fixed. This provided the necessary constrained shrinking along one direction to form uniaxial nanowrinkles.

As shown in Fig. 5.16, the graphene composites were inspected by SEM, presenting the surface profile of both shrink induced nanowrinkles of LbL self-assembled graphene on the PO substrate at different shrink temperature. It is very easy to observe that large areas of uniform biaxial nanowrinkles can be produced on the substrate. And the density of the graphene nanowrinkles is increasing along with the increasing of the shrink temperature. To verify the theoretical predictions for biaxial shrinkage, a quantitative analysis of the surface profile of the graphene composites was realized by AFM and the analysis software NanoScope (R) III (version 5.31R1, Veeco Instruments, Inc.). As shown in Fig. 5.17a-e, three-dimensional AFM images of the self-assembled graphene thin films demonstrated that, at different heat treatment temperature, the surface

morphologies and roughness of the graphene films were obviously different. The film shrunk at higher temperature has a higher surface roughness (Fig. 5.17f). Besides, the surface area of the samples prepared at different shrink temperature under the same scanning area was also different. As was shown in Fig. 5.17g, the surface area increased along with the rising of the temperature. These results confirmed the theoretical analysis of the relationship between density of the nanowrinkles and the shrink temperature.

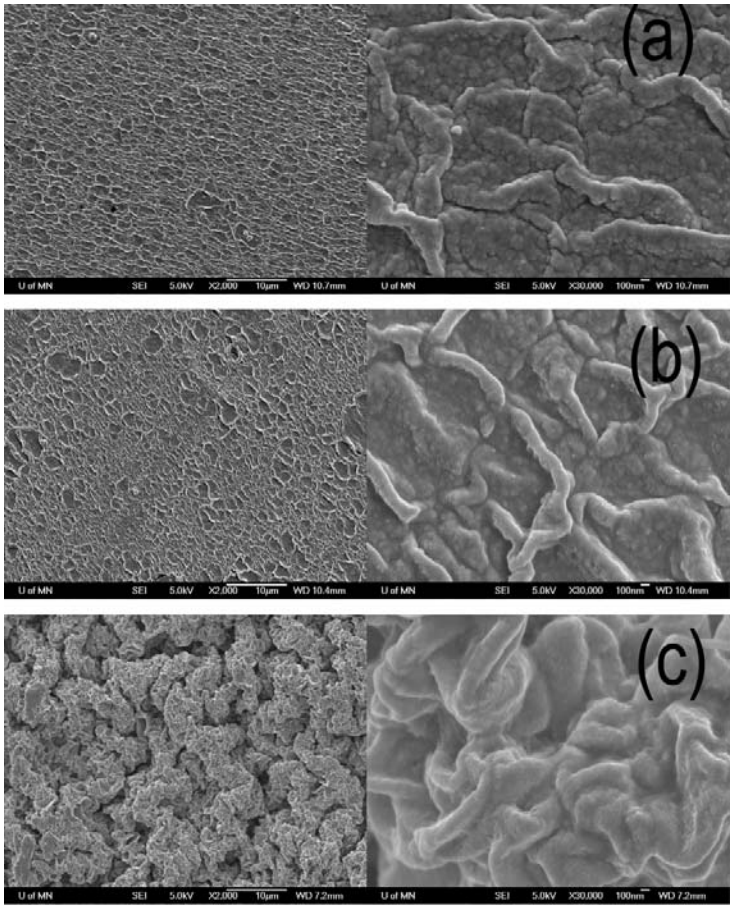


Figure 5.16 SEM images of graphene composites treated at different temperature: (a) 100°C; (b) 120°C; (c) 140°C. Left: the lower magnitude of SEM image; right: the larger magnitude of SEM image. The surface morphologies of the samples from various shrink

temperature is obvious different. The density of the graphene nanowrinkles is increasing along with the increasing of the shrink temperature.

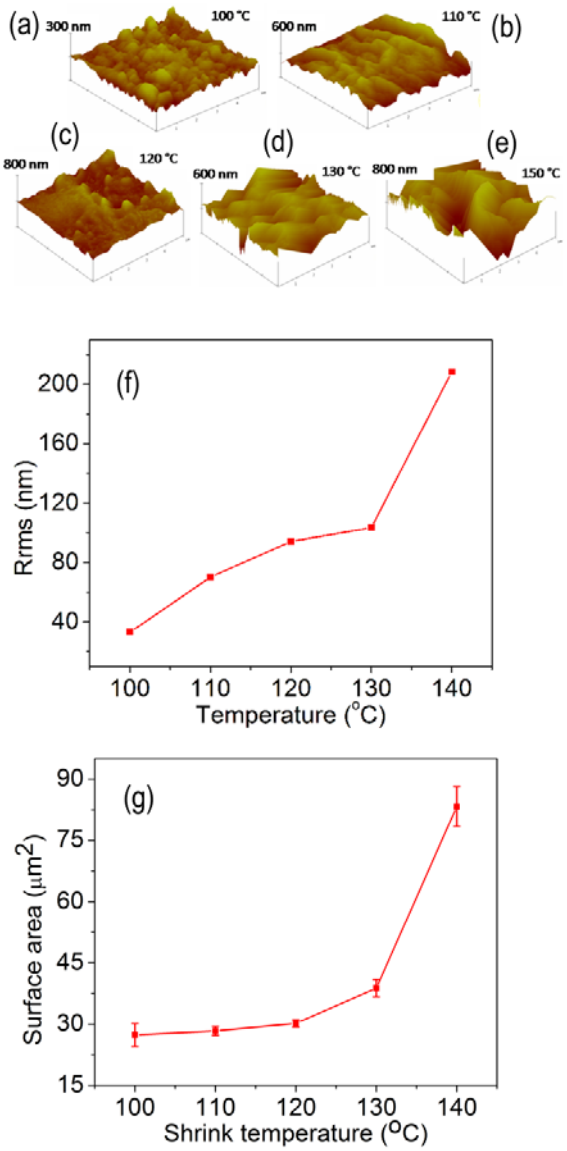


Figure 5.17 (a-e) 3D AFM images of the self-assembled graphene composites from various shrink temperature. The (f) surface roughness and (g) surface area of the graphene composites versus the shrink temperature curves demonstrate that the higher shrink temperature induces higher density of the nanowrinkles.

In the uniaxial shrink case, two edges of a PO shrink film were fixed to provide it constrained shrink along only one direction. The surface deformation of uniaxial shrinkage presents more regular cosine pattern compared with biaxial shrinkage, which is demonstrated in Fig. 5.18.

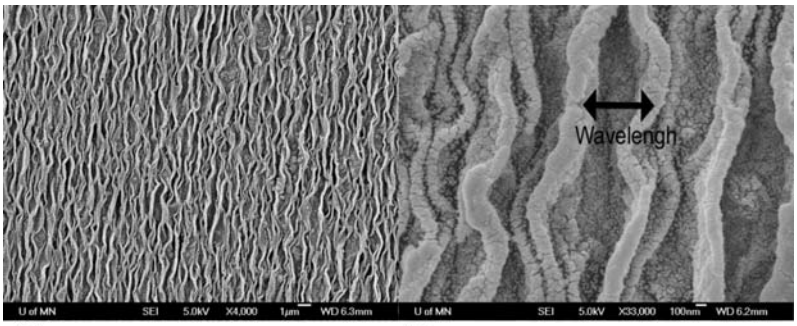


Figure 5.18 SEM images of uniaxial shrink graphene composites. During the shrink process, two edges of a PO shrink film were clamped by clips to ensure it could only shrink in one direction while the other one is fixed.

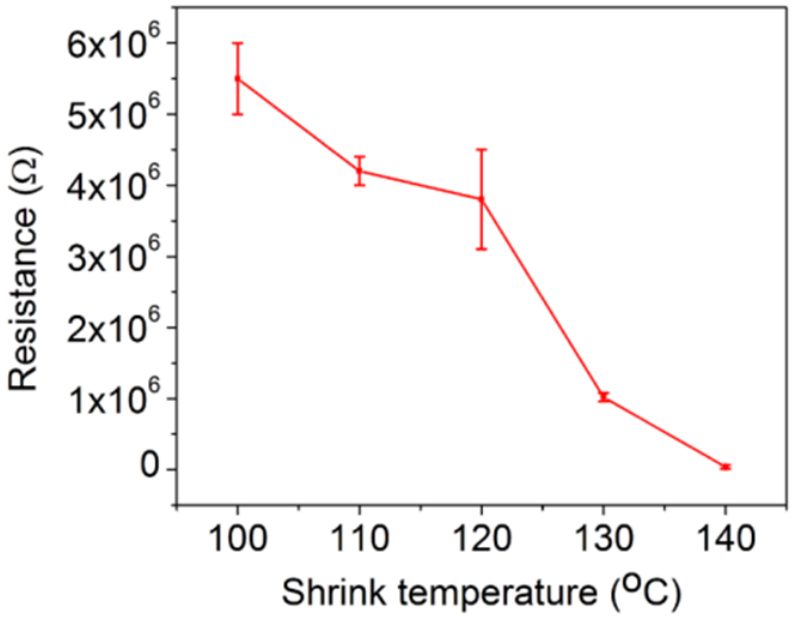

Figure 5.19 Chemical sensors based on the shrink induced graphene composites were fabricated. The original resistance versus the shrink temperature curve was investigated. A pH sensor was fabricated based on the shrink induced graphene composites. After self-assembly of graphene nanoplatelets on the PO shrink film, the substrate was shrunk in the convection oven. Then, a piece of 500 μm polyimide ribbon was fixed on the shrunk substrate as the shield mask. And chromium/gold layers 50/200 nm thick was deposited on the substrate as the electrodes with an AJA sputter system (Model ATC 2000). Finally, the sensor was finished after striping of the shield mask. The original resistance of the chemical sensors was measured, shown in Fig. 5.19. All the sensing area was compared based on same final projected area. Since the shrink rate is different at different shrink temperature, the higher temperature will have larger initial area in order to keep the final projected area same. The higher shrink temperature was able to offer lower resistance. Then, different pH buffer solutions were introduced onto graphene sensor, and the conductance shift was monitored by the Agilent Data Logger (34970A, Agilent Inc.). The higher shrink temperature will give higher density of graphene nanowrinkles and the surface area, which is confirmed by the AFM analysis. This will aggrandizes the ability of absorption of hydrogen ions, contributing to the better sensitivity at higher shrink temperature. The lower resistance of graphene composites from higher shrink temperature is also dependent on the surface morphologies. Because electrons can move faster through the interconnected graphene composites, and higher density of wrinkles can offer more paths for the electrons, which can reduce the resistance.

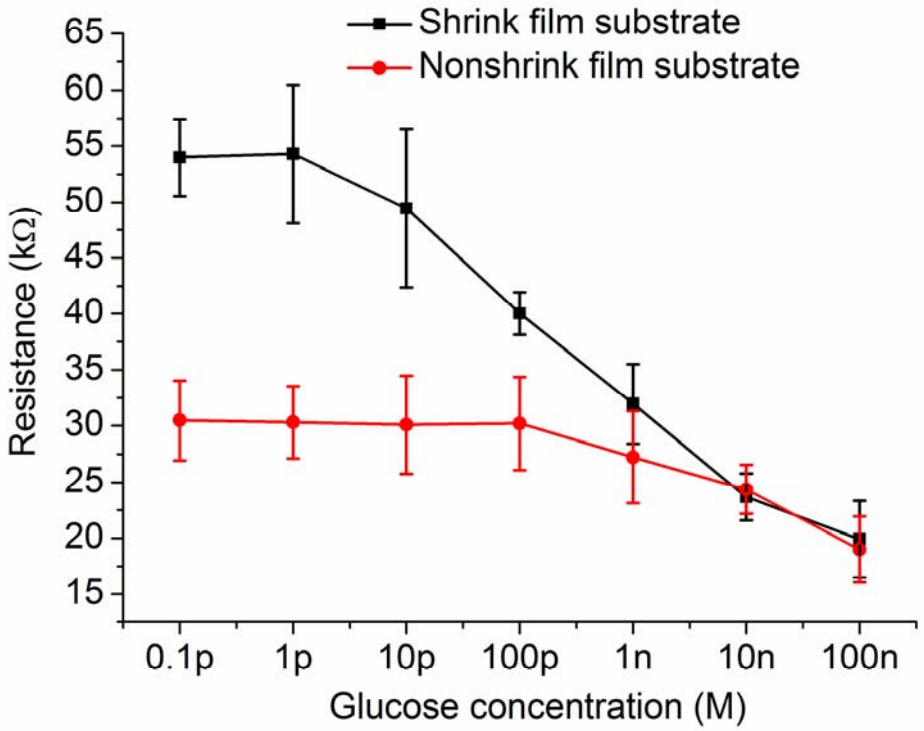


Figure 5.20 Glucose detection was characterized on the chemical sensor based on the shrink induced graphene composites, presenting a detection limit down to 10 pM. The control group with nonshrink substrate was investigated, presenting worse detection limits compared with shrink substrate group. The shrink substrate will introduce low-cost nanowrinkles.

The shrink induced graphene sensors was also verified for functionality and detect limitation of glucose sensing. After the graphene sensor was fabricated, glucose oxidase (GOx) was immobilized on the sensing region by LbL self-assembly. The GOx and glucose were prepared from Dulbecco's phosphate buffered saline (PBS). All the above materials were purchased from Sigma–Aldrich Corporation. The GOx functionalization was achieved by applying a layer of PDDA then of GOx until we have a trilayer

$[PDDA+GOx]_3$. The GOx on the surface reacted with the glucose and generated hydrogen ions. Biocatalyzed hydrolysis of glucose in the presence of GOx resulted in the changes of local pH. Different concentrations of glucose would lead to different response of graphene resistance change due to the various amount of hydrogen ions generation. As shown in Fig. 5.20, the resistance of graphene composits were changing according to different concentrations of glucose solutions were delivered. The graphene sensor was capable of responding down to 10pM. To confirm the detection limit of glucose, we also introduced 0.1pM and 1 pM solution onto the graphene sensors. The response of 0.1pM and 1 pM glucose were the same.

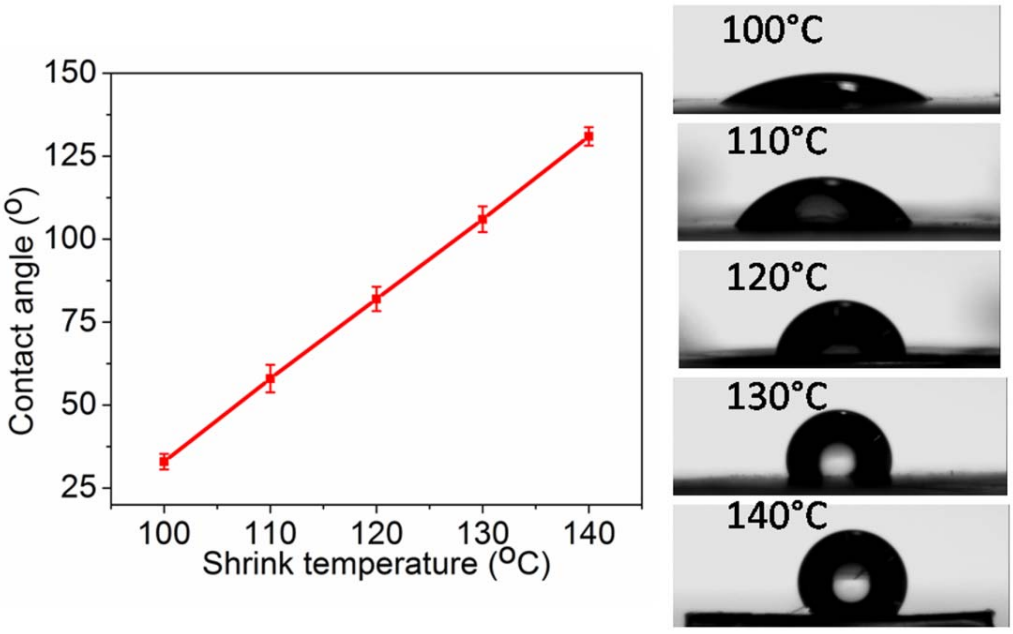


Figure 5.21 Contact angle of the graphene composites raised along with the increasing of the shrink temperature.

In addition, this shrink induced graphene composites can also serve in the microfluidic applications due to its tunable surface morphology, which can controllably change the surface wetting ability. The contact angle was a direct reflection of surface wetting ability, which was measured for the graphene composites samples treated at different shrink temperature. As shown in Fig. 5.21, the contact angle of the graphene composites raised along with the increasing of the shrink temperature, which means that heavier density of graphene nanowrinkles can provide lower wetting ability. It can be explained by Cassie–Baxter model, which describes the situation that droplets settle only on the peaks of the roughened surface and leaves the air trapped below. The Cassie–Baxter model defines the contact angle as the equation:

$$\cos\theta = f_s(\cos\theta_0 + 1) - 1,$$

where θ is the contact angle, $f_s$ is the fraction of liquid droplet surface in contact with the solid, and $\theta_0$ is the intrinsic contact angle of the self-assembled graphene layers on its flat surface. The rougher graphene composites surface from higher shrink temperature has a smaller fraction of solid area in contact with the water droplet ($f_s$), resulting a larger contact angle according to the Cassie–Baxter model. With the tunable surface wetting ability, there will be potential microfluidic applications by shrinking the graphene composites in the microchannels patterned in the PO shrink film.

## 5.5 Conclusion

The thermoplastic shrink lithography and movable type shrink lithography offer a number of advantages over the current conventional lithography techniques. Both of the shrink lithography achieves very low cost process in manufacturing nano scale patterns

without any expensive technique such as electron beam lithography. The embossing molding of shrink lithography is capable of patterning large area at once, which offers the oppotunity of mass production. Numerous permutations and combinations of movable type molding are capable of fabricating different patterns on the same substrate without extra new molds. In addition, different feature size of patterns can be realized by shrink lithography from a single mold by controlling the embossing pressure and shrink temperatures, which introduces a programable lithography and further decreases the cost. The tunable shrink induced graphene composites based on LbL self-assembly offers a number of advantages over the current graphene based composites. Due to the heat shrink of the PO substrate, the graphene composites are capable of controllably turning the surface morphologies by simply adjusting the shrink temperature, which is superior to that of general macroscopic graphene structures with fixed properties. The unique tunable properties of graphene composites should enable many applications including high-performance chemical sensing and microfluidic. In addition, owing to versatility and facility of the LbL self-assembly technique, it can be a general strategy for fabricating a broad class of macroscopic graphene structures with tunable properties and new applications.

# CHAPTER 6

# BIOSENSOR SYSTEM POWERD BY DSSC

## 6.1 Introduction

Power source is very important for many electrical systems, including various sensor systems. In many situations, power source will limit the performance of system, such as mobile devices. The size and life time of power sources will greatly influence the design of sensor systems. In most of the cases, battery will be the power source of sensors. However, battery contains many toxic components which are harmful to human health and environments [125]. In addition, the fabrication and the recycling of battery are very high cost and not environmental friendly processes. Therefore, a nanomatrial based sensor will make the sensor system much easier to design, in a low-cost and green strategy.

Generally, nanomatrial based sensors can be attributed into several catalogs, such as chemical, nuclear, or solar cell based sensors. Nanomatrial based sensors can scavenge energy from environment [126] to support their energy consumption requirements without an external power source like battery or electrical outlet.

The first nanomatrial based sensor was used for nuclear sensing. Normally, the radioactive decay or nuclear reactions can be used to support the energy consumption of a sensor system. Another large category of nanomatrial based sensors are the electrochemical based nanomatrial based liquid/wetness sensor. These sensors are initially dry. When liquid is applied, electrochemical reaction will happen, providing energy to support the working of sensor system. However, these two types of nanomatrial

based sensors have many limitations in their applications. The nuclear based nanomatrial based sensor system is very high cost and complex. The nuclear source is hard to recycle and control after usage. In addition, this type of sensor is not good for human health and environment because of radio contamination. The electrochemical based nanomatrial based sensor system can only be used under liquid conditions. Because it is initially dry, the electrochemical reaction cannot happen without liquid introduced.

Meanwhile, renewable energy harvesting are attracting interests as an alternative to traditional sources of energy such as fossil fuels [127]. Photovoltaic devices converting light into electricity are a viable solution for alternative energy these days. Solar energy is acknowledged as clean and renewable energy. Therefore, solar cell based nanomatrial based sensor system shows much more advantages compared with the other nanomatrial based sensor systems.

Research in biosensors started in the 1980's and has been growing very fast due to the strong demands from health care industry developments. Successful biosensor technology has expanded and the current market is valued over $10 billion. Low-cost and sensitive biosensors capable of quickly detecting various diseases can dramatically reduce the heavy loads of regular clinical diagnosis. Many fully developed biosensors are integral parts of disease control including diseases such as diabetes, prostate cancer. However, a lot of biomedical equipments are built with incredible expensive and complex structures, and the power consumption cannot be ignored.Even for smaller units, the battery recharge or recycling are also big challenges. Therefore, nanomatrial based biosensor system is very useful in the biomedical applications.

### 6.2 Self Powered Biosensor System Development and Characterization

According to the chapter 5 discussions, a high performance and low cost solar cell has been developed. By integrating solar cell, it is desirable to develop biosensor systemsforbetter performance and lower cost. The biosensor systems can also work without external energy sources using photovoltaic techniques, reducing the cost in a green strategy. On the other hand, in chapter 4, shape memory polymers, which can offer a mechanical action triggered by an external stimulus, introduce promising applications in molecular detection, high-surface-area conductors and actuators in a tunable and controllable strategy. Here a nanomatrial based biosensor system integrated with DSSC was developed. The tunable shrink induced three-dimensional structure was also introduced to enhance the performance of both glucose biosensors and DSSCs in a very low-cost way. Unlike the conventional microstructures, this proposed method introduces tunable and controllable microstructures from a shrink polymer using a single mold. The improved DSSC with shrink induced three-dimensional structures can transfer the solar energy into the energy storage unit (CBC-EVAL-10), which supports the biosensor energy demand. Meanwhile the performance of biosensor was improved by the shrink induced three-dimensional structure. The total system was connected to a computer through a USB control unit (PICDEFS-USB). This nanomatrial based biosensor system integrated with communication technologies may have great point-to-care medical applications.

Fig. 6.1 shows the fabrication processes of the tunable shrink induced three-dimensional pillar arrays for both biosensor and DSSC. Firstly a silicon mold was fabricated by

photolithography. Then the patterns were generated on the shrink polymer (Polystyrene, Shrinky-Dinks, Alex Inc.) by hot embossing (Model Grimco 12-1-HT). The patterns on the shrink polymer were gently polished and removed by sandpaper. The polished shrink polymers were heated for shrinkage at different temperatures to obtain various micro pillar arrays. Due to the properties of the shrink polymer, the lateral dimension will decrease by 50%, however, the vertical dimension will increase by 400%. As a result, high-respect-ratio micro pillar arrays were generated [128]. To fabricate the biosensors, the substrate was immersed into the charged suspensions with a sequence of [poly(diallyldiamine chloride) (PDDA) (10 min) + graphene suspension (20 min) + PDDA (10 min) + CNT suspension (15 min)]n. The polyelectrolytes used in self-assembly were purchased from Sigma–Aldrich Inc. The concentrations of aqueous PDDA were 1.5 wt%, with an addition of 0.5 M sodium chloride to enhance the surface properties. Research grade graphene (PureSheetsTM, 0.25 mg/ml) suspension solution and CNT (PureTubesTM, 0.05 mg/ml) suspension solutionwere purchased from Nanointegris Inc. After deposition of gold electrodes, the glucose oxidase (GOx, Sigma Inc) was immobilizedon the surface of patterned substrate by self-assembly.

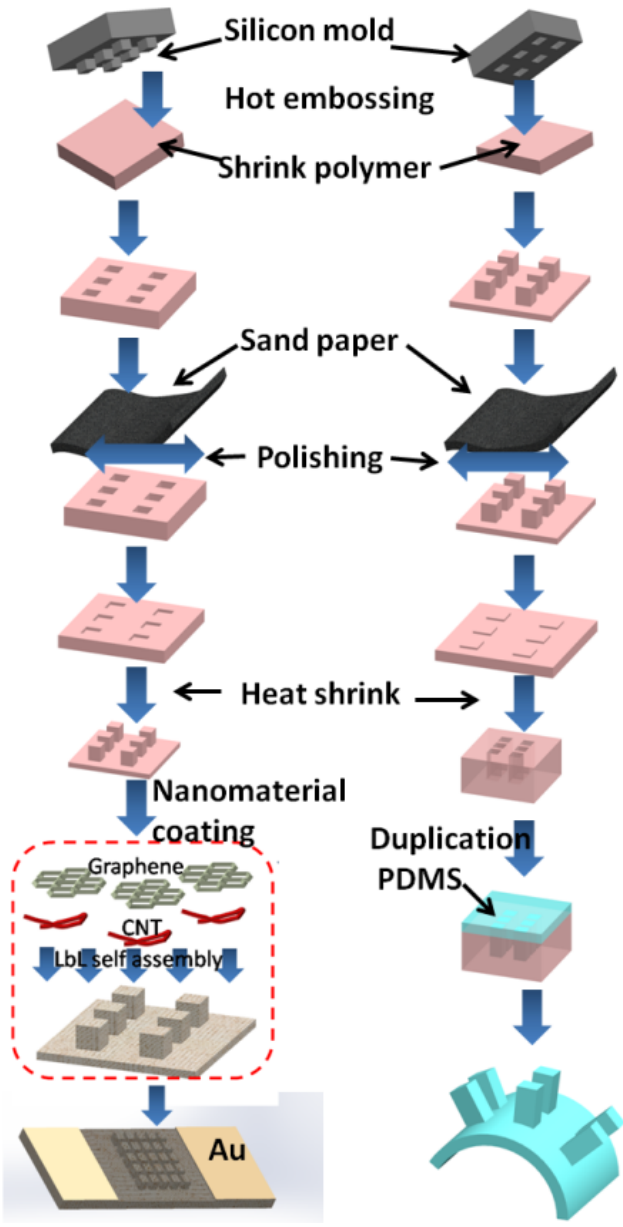


Figure 6.1 Schematic illustration of fabrication processes of the shrink induced three-dimensional structures for biosensor and DSSC.

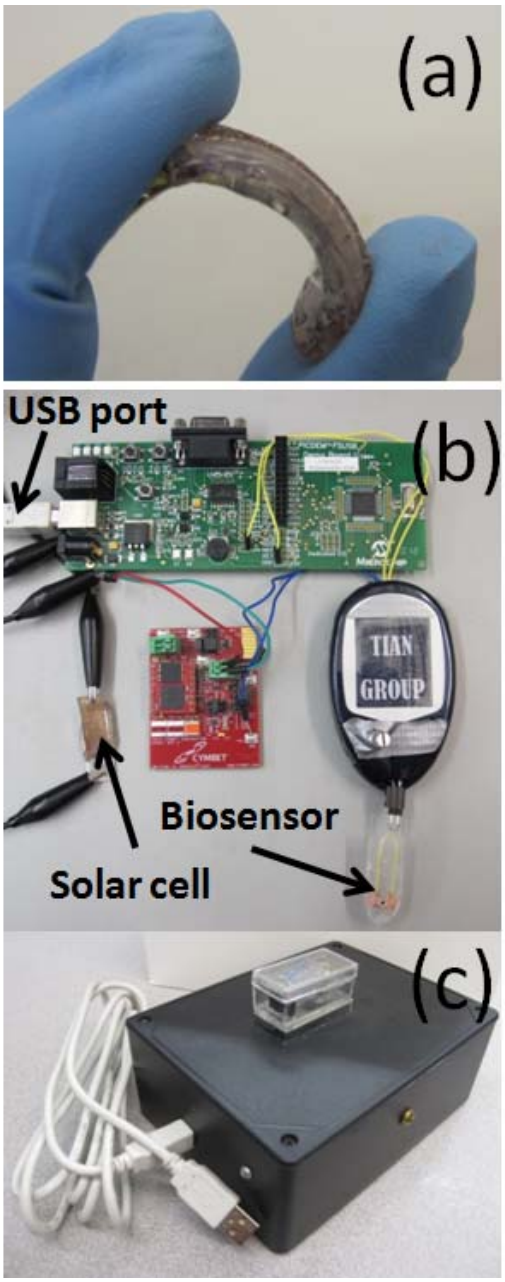


Figure 6.2: (a) The all-polymer structure of DSSC presents very good flexibility. (b) Circuit connection between biosensor and solar cell. (c) All components were packaged to form a biosensor system.

To fabricate the flexible DSSC with micro pillar arrays, the shrink polymer molds with micro pillar arrays were used to generate the PDMS chips. A layer of $TiO_2$ paste (P6-2100-13; Aqua Solutions, Inc.) was blading coated on the patterned PDMS substrate on top of 100 nm ITO, then dried for 30 min at 150 ºC, followed by UV light treatment for 12 hours. After N719 dye (703214; Sigma-Aldrich, Inc.) adsorption for 24 hours, the $TiO_2$ photoanode and a platinum/PET counter-cathode were assembled to form a sandwich-type cell, and sealed with epoxy. The electrolyte was 50 mM of tri-iodide in methoxypropionitrilepurchased from Solaronix Inc. As shown in Fig. 6.2a, due to the all-polymer structure of the DSSC, it is capable of bending at a large degree of angle. As shown in Fig. 6.2b, the solar energy storage uite CBC-EVAL-10 connected the improved DSSC with the biosensor to support its energy demand. In order to achieve user friendly, the total system was packaged and connected to a computer through a USB control unit PICDEFS-USB, shown as Fig. 6.2c.

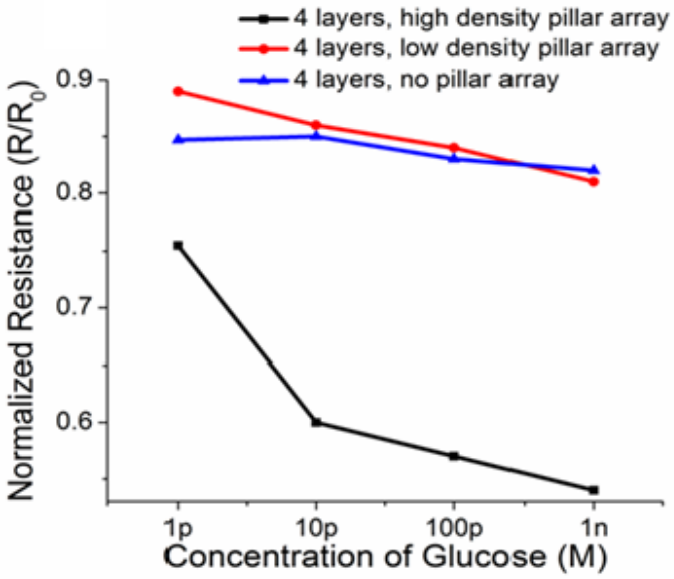

Figure 6.3 Detection limits characterization of three types of biosensors. The biosensor fabricated with pillar array can achieve 1 pM detection limit, better than the flat substrate with only 10 pM. In order to get clearer readout, normalized resistance was introduced.

The biosensor was also characterized for the detect limitation of glucose sensing. After the biosensor was fabricated, GOx was immobilized on the sensing region. The GOx on the surface reacted with the glucose and created hydrogen ions as such:

$$\beta - D - glucose + O_2 \xrightarrow{GOx} D - glucono - \delta - lactone + H_2O_2$$

$$D - glucono - \delta - lactone + H_2O \rightarrow D - gluconate^- + H^+$$

Different concentrations of glucose can cause different local pH. Given that the conductance of graphene is determined by carrier density and mobility, the conductance of graphene composites must shift when hydrogen ions are absorbed by graphene. As shown in Fig. 6.3, different concentrations of glucose solutions were introduced onto the biosensor with three-dimensional microstructures, and the resistance shift was monitored. The detection limit of glucose biosensor with pillar arrays can be achieved at 1 pM, but the flat biosensor can only reach 10 pM. The microstructure will give higher density of graphene nanowrinkles and the surface area, which is confirmed by the SEM analysis. This will aggrandizes the ability of absorption of hydrogen ions, contributing to the better detection limits.

### 6.3 Conclusion

In the present study, the low-cost and controllable shrink induced three-dimensional microstructures were introduced to enhance the performance of biosensors and DSSC. The improved DSSC can transfer the solar energy into the energy storage unit to support

the biosensor energy demand. The nanomatrial based biosensor system can be connected to a computer by a USB control unit to achieve point-to-care applications. The biosensor system was performed as a glucose detection platform with 1 pM detection limit.

# CHAPTER 7

# CONCLUSIONS

## 7.1. Summaries

The main objective of thesis research is to develop nanomatrial based biosensors integrated with nanomaterials, which is aim to achieve high performance in detection limits, sensitivity, stability, etc. Due to the unique structural, electrical, chemical, and mechanical properties of nanomaterials, the characteristic results of biosensors will demonstrate the advantages in the applications. According to using nanomaterials and improved fabrication processes, the cost of biosensors will be decreased dramatically. High efficiency DSSC will be integrated into the biosensor system to support the work of sensing without external sources. Different types of sensor structures and manufacture strategies will be investigated based on the biosensor platform, considering various factors and conditions that affect sensing performance of the system in order to optimize the biosensors and to find the best operating conditions for optimal sensing performance. Furthermore, more detailed analyses about biosensing characteristics will be done as well as stability characteristics of the biosensors.

In chapter 2, the general farication background information on graphene and graphene compositshas beendiscussed. There different types of graphene and graphene composits preparison processes were presented.The pure graphene was generated by mechanical exfoliation method developed by Dr. Peng Li. The assembled graphene composites were fabricated by microfluidic method without introducing other hybrid material. And the hybridized graphene composites were formed by self assembly technique. The

performance of the three different types biosensors were investigated and compared. The manufacture processes of biosensors were also introduced here, including flexible biosensor and suspended graphene sensors.

In chapter 3, graphene biosensor surface modification processes were presented. The basic sensing mechanism was also investigated. Different biotarget detections were shown, demonstrating this sensor can be a platform to diagnose cancer and other complex diseases. Three different types of graphene biosensors were synthesized and compared. From the comparison of the performance of the different graphene composite biosensors, it can be concluded that all of them can be used for biotarget detection. The self assembled graphene biosensors demonstrated the best detection limits and sensitivity, and the pure graphene and microfluidic induced graphene biosensors showed the better stability. The trend in sensitivity and stability towards the different graphene structures is dependent on the hybrid polymers, which introduce electrical disturbance for sensor applications but enhance the absorption of target moleculeon the other hand.

In chapter 4, the background of solar cell development was introduced, and the basic mechanism of DSSC was investigated. Wrinkles and nanogaps on shrink polymer substrates are natural responses to the heat shrink induced stress mismatch of materials, and can be easily introduced to large areas in a very low-cost way. By using these shrink induced structures on the photocathodes, the ECE of DSSCs can be enhanced 34.1% due to the increase of light scattering and/or trapping as well as the enlargement of Pt catalytic surface area. Especially, these nanogaps enhance the light absorption at the incident wavelength from 300 nm to 400 nm. Moreover, the shrink polymer can also

provide low-cost patterns on photoanodes, demonstrating all-polymer structure of DSSC with 59.3% enhancement of ECE. The all-polymer structure DSSC can provide great flexibility. It is believed that these low-cost shrink induced micro/nanostructures enable to extend in many other photovoltaic deviceapplications such as quantum dotsolar cells and organic solar cells.

In chapter 5, the thermoplastic shrink lithography and movable type shrink lithography were presented, offering a number of advantages over the current conventional lithography techniques. Both of the shrink lithography achieves very low cost process in manufacturing nano scale patterns without any expensive technique such as electron beam lithography. The embossing molding of shrink lithography is capable of patterning large area at once, which offers the oppotunity of mass production. Numerous permutations and combinations of movable type molding are capable of fabricating different patterns on the same substrate without extra new molds. In addition, different feature size of patterns can be realized by shrink lithography from a single mold by controlling the embossing pressure and shrink temperatures, which introduces a programable lithography and further decreases the cost.Due to the heat shrink of the PO substrate, the graphene composites are capable of controllably turning the surface morphologies by simply adjusting the shrink temperature, which is superior to that of general macroscopic graphene structures with fixed properties. The unique tunable properties of graphene composites should enable many applications including high-performance chemical sensing and microfluidic.

In chapter 6, the low-cost and controllable shrink induced three-dimensional microstructures were introduced to enhance the performance of biosensors and DSSC. The improved DSSC can transfer the solar energy into the energy storage unit to support the biosensor energy demand. The nanomatrial based biosensor system can be connected to a computer by a USB control unit to achieve point-to-care applications. The biosensor system was performed as a glucose detection platform with 1 pM detection limit.

### 7.2 Conclusions

In the present study, different biosensors were proposed and investigated including ion-selective sensors, cancer marker sensors, glucose sensors, etc. The performance of the biosensors was studied such as detection limits, sensitivity, stability, etc. Suspended structure of biosensors was also researched, which can offer down to 0.1 fg/ml detection limits. Various fabrication processes of graphene were introduced, such as LbL self assembly, microfluidics, and mechanical exfoliation. In addition, shrink lithography was also used to fabricate sensing materials of biosensors. GNR and shrink induced graphene composites were investigated on the performance of biosensors.

In addition, a DSSC was designed and fabricated to supply the power source of biosensors without external sources. Different techniques will be applied to design and manufacture photovoltaic with higher energy conversion efficiency, such as shrink polymer and hot embossing. Nanostructure in active layer can be used to scatter the incident light to enhance the transfer path of photon, which can increase the energy conversion efficiency. What's more, the life time of the solar cell was studied to achieve considerable long stability in order to support the sensing work of biosensors.

### 7.3 Future Recommendations

First, more nanomaterials may be investigated to get better biosensors. Nanoparticles or quantum dots are good candidates to act as sensing materials. Graphene has been used as sensing material with good performance including sensitivity, detection limits, etc. However, the accuracy is also critical for biosensing applications. More biosensors based on new nanomaterials can be developed and compared with the existing sensors to determine the optimal material and design. Especially, the detection limits and the resolution will be paid more attention to get better performance biosensor for medical applications. The quantum dots are capable of providing single molecule detection, which is very useful for fundamental understanding of biosensing mechanism.

Second, new designs of biosensors' structure can be developed. Besides the designed biosensors, other structures of biosensor can be studied which may obtain better performance. Ion sensitive electrodes and surface plasmon resonance are developed rapidly these days for biosensing applications. Nanomaterials can be extended to the new structure biosensors to perform sensing work, compared with these results.

## Reference


[1]Y. Shao, J. Wang, H. Wu, J. Liu, I. Aksay, Y. Lin, Graphene Based Electrochemical Sensors and Biosensors:A Review, Electroanalysis, 22 (2010) 1027-1036.

[2] J. Wang, Carbon-Nanotube Based Electrochemical Biosensors: A Review, Electroanalysis, 17 (2005) 7-14.

[3] J.Vidal, L. Bonel, A. Ezquerra, S. Hernández, J.Bertolín, C. Cubel, J.Castillo, ElectrochemicalAffinity BiosensorsforDetectionofMycotoxins: A Review, Biosensors andBioelectronics, 49(2013)146–158.

[4] X. Chen, D. Kim, S. Hong, The Carbon Nanotube-Based Nanobiosensor: A Key Component for Ubiquitous Real-Time Bioscreening System?Nanomedicine, 9(2014) 565-567.

[5] T.Phan, P.Tran, X. Pham, N. Dang, V. Nguyen, V. Tran, T. Bui, M. Dang, D. Tong, Glucose Biosensor Based on Platinum Nanowires: A Clinical Study, International Journal of Nanotechnology, 10 (2013) 166-177.

[6] H. Yang, C. Lin , M.Hua , S. Liao , Y. Chen,H. Chen, W.Weng, C. Chuang, S. Pang, C. Ma, Combined Detection of Cancer Cells and a Tumor Biomarker using an Immunomagnetic Sensor for the Improvement of Prostate-Cancer Diagnosis, Advanced Materials, 26 (2014) 3662-3666.

[7]M. Spiegel, P. Sterrenburg, W. Haasnoot, H.J. van der Fels-Klerx, Towards A Decision Support System for Control of Multiple Food Safety Hazards in Raw Milk Production, Trends in Food Science & Technology, 34 (2013) 137-145.

[8] W. Zhang, A.Asiri, D. Liu, D. Du, Y. Lin, Nanomaterial-Based Biosensors for Environmental And Biological Monitoring of Organophosphorus Pesticides And Nerve Agents, TrAC Trends in Analytical Chemistry, 54 (2014) 1-10.

[9] L. Lu, H. Li, F.Qu, X. Zhang, G.Shen, R. Yu, In Situ Synthesis of Palladium Nanoparticle–GrapheneNanohybrids And TheirApplication in Nonenzymatic Glucose Biosensors, Biosensors andBioelectronics, 26 (2011) 3500–3504.

[10] T.Kurkina, A.Vlandas, A. Ahmad, K. Kern, K.Balasubramanian, Label-Free Detection of Few Copies of DNA with Carbon NanotubeImpedance Biosensors, Angew. Chem. Int. Ed. 50 (2011) 3710 –3714.

[11] X.Duan, Y. Li, N. Rajan, D. Routenberg, Y.Modis, M. Reed, Quantification of The Affinities and Kinetics of Protein Interactions Using SiliconNanowire Biosensors, Nature Nanotechnology, 7 (2012) 401-407.

[12]K. Zhou, Y. Zhu, X. Yang, C. Li, Electrocatalytic Oxidation of Glucose by the Glucose OxidaseImmobilized in Graphene-Au-NafionBiocomposite, Electroanalysis, 22 (2010) 259-264.

[13]B.Unnikrishnan, S.Palanisamy, S. Chen, A Simple Electrochemical Approach to Fabricate A Glucose BiosensorBased on Graphene–Glucose Oxidase Biocomposite, Biosensors andBioelectronics, 39 (2013) 70-75.

[14]K.Sreekanth, S.Zeng, K. Yong, T. Yu, Sensitivity Enhanced Biosensor Using Graphene-Based One-Dimensional PhotonicCrystal, Sensors and Actuators B 182 (2013) 424–428.

[15] A. Menegaki, Growth And Renewable Energy in Europe: Benchmarking with DataEnvelopment Analysis, Renewable Energy 60 (2013) 363-369.
[16] B. Shin, O.Gunawan, Y. Zhu, N. Bojarczuk, S. Chey, S.Guha, Thin film Solar Cell with 8.4% Power ConversionEfficiency Using An Earth-Abundant $Cu_2ZnSnS_4$ Absorber, Prog. Photovolt: Res. Appl. 21(2013) 72–76.
[17] S.Cai, X. Hu, Z. Zhang, J. Su, X. Li, A. Islam,L. Han, H.Tian, Rigid Triarylamine-Based Efficient DSSC Sensitizers withHigh Molar Extinction Coefficients, J. Mater. Chem. A, 1 (2013) 4763–4772.
[18] J.Krantz, T.Stubhan, M. Richter, S.Spallek, I.Litzov, G. Matt, E.Spiecker, C. Brabec, Advanced Function Materials 23 (2013) 1711–1717.
[19] B.O'Regan, M.Grätzel, A Low-Cost, High-Efficiency Solar Cell Based on Dye-Sensitized Colloidal $TiO_2$ Films, Nature 353 (1991) 737–740.
[20] S. Mathew, A. Yella1, P.Gao, R.Humphry-Baker, B. Curchod,N.Ashari-Astani, I. Tavernelli, U.Rothlisberger, M. Nazeeruddin, M.Gra¨tzel, Dye-Sensitized Solar Cells with 13% EfficiencyAchieved Through The Molecular Engineering ofPorphyrin Sensitizers, Nature Chemistry, 6, 242-247.
[21] M. Zhao, J. Huang, Y. Zhou, Q. Chen, X. Pan,H. He, Z. Ye, A Single MesoporousZnO/Chitosan Hybrid Nanostructure for A NovelFree Nanoprobe Type Biosensor, Biosensors and Bioelectronics 43 (2013) 226–230.
[22] S. Lo, Y. Hung, D. Jan, Stress Induction, UV Emission Variation AndEfficiency Variation In Dye-Sensitized SolarCells of Hollow ZnS/ZnO/ZnS Nanostructures, Journal of Material Chemistry A, 1 (2013) 10274–10280.
[23] J. Cork, R. Jones, J. Sawyer, Low Cost, Disposable Biosensors Allow Detection of Antibodies with ResultsEquivalent to ELISA in 15 Min, Journal of Immunological Methods 387 (2013) 140–146.
[24] Y. Choi, G. Lee, H.Ko, Y. Chang,M. Kang, J.Pyun, Development of SPR Biosensor for The Detection of Human HepatitisB Virus Using Plasma-Treated Parylene-N Film, Biosensors and Bioelectronics 56 (2014) 286–294.
[25] T. Yin, Y. Zhao, J.Horak, H.Bakirci, H. Liao, H. Tsai, Y.Juang, G. Urban, A Micro-Cantilever Sensor Chip Based on Contact AngleAnalysis for A Label-Free Troponin I Immunoassay, Lab on a Chip, 13 (2013) 834–842.
[26] K. Ratinac, W. Yang , S. Ringer, F.Braet, Toward Ubiquitous Environmental Gas Sensors Capitalizing on the Promise of Graphene, Environ. Sci. Technol. 44 (2010) 1167-1176, 2010.
[27] C. Song, G. Xie, L. Wang, L. Liu, G. Tian, H. Xiang, Dna-Based Hybridization Chain Reaction for An Ultrasensitive Cancer Marker EBNA-1 Electrochemical Immunosensor, Biosensors and Bioelectronics 58 (2014) 68-74.
[28] R. K. Joshi, P. Carbone, F. C. Wang, V. G. Kravets, Y. Su, I. V. Grigorieva, H. A. Wu, A. K. Geim,R. R. Nair,Precise and Ultrafast Molecular Sieving Through Graphene Oxide Membranes, Science, 343 (2014) 752-754.
[29] J. Torres, R. Kaner, Graphene Synthesis: Graphene Closer to Fruition, Nature Materials, 13 (2014) 328-329.

[30] B. Ahmadi-Moghadam, F. Taheri, Effect of Processing Parameters on The Structure And Multi-Functional Performance of Epoxy/Gnp-Nanocomposites, Journal of Materials Science, 49 (2014), 6180-6190.
[31] E. Jaworska, W. Lewandowski, J. Mieczkowski, K. Maksymiuk, A. Michalska, Critical Assessment of Graphene as Ion-To-Electron Transducer for All-Solid-State Potentiometric Sensors, 97 (2012) 414-419.
[32] W. Grosse, J. Champavert, S. Gambhir, G. Wallace, S. Moulton, Aqueous Dispersions of Reduced Graphene Oxide And Multi Wall Carbon Nanotubes for Enhanced Glucose Oxidase Bioelectrode Performance, 61 (2013) 467-475.
[33] X. Zhang, Y. Zhang, Q. Liao, Y. Song, S. Ma, Reduced Graphene Oxide-Functionalized High Electron Mobility Transistors for Novel Recognition Pattern Label-Free DNA Sensors, Small, 9 (2013) 4045-4050.
[34] A. Balandin, Low-Frequency 1/f Noise in Graphene Devices, Nature Nanotechnology, 8 (2013) 549-555.
[35] D. Ye, G. Liang, H. Li, J. Luo, S. Zhang, H. Chen, J. Kong, A Novel Nonenzymatic Sensor Based on Cuo Nanoneedle/Graphene/Carbon Nanofiber Modified Electrode for Probing Glucose in Saliva, 116 (2013) 223-230.
[36] Y. Dong, H. Ding, J. Zhang, X. Chu, Electrogenerated Chemiluminescence of Luminol at A Gold Nanoparticle-Carbon Nanotube-Graphene Composite Modified Glassy Carbon Electrode in Neutral Solution, 5 (2013) 5954-5960.
[37] X. Gan, R. Shiue, Y. Gao, I. Meric, T. Heinz, K. Shepard, J. Hone, S. Assefa, D. Englund, Chip-Integrated Ultrafast Graphene Photodetector with High Responsivity, Nature Photonics, 7 (2013) 883-887.
[38] J. Song, L. Xu, C. Zhou, R. Xing, Q. Dai, D. Liu, H. Song, Synthesis of Graphene Oxide Based CuO Nanoparticles Composite Electrode for Highly Enhanced Nonenzymatic Glucose Detection, ACS Applied Materials & Interfaces, 5 (2013) 12928-12934.
[39] S. Pei, H. Cheng, The Reduction of Graphene Oxide, Carbon, 50 (2012) 3210-3228.
[40] A. Kumar, K. Park,H. Kim, K. Kim, Noise And Its Reduction in Graphene based Nanopore Devices, Nanotechnology, 24 (2013) 495503.
[41] G. Dai, P. Cooke, S. Deng, Direct Growth of Graphene Films on TEM Nickel Grids Using Benzene as Precursor, Chemical Physics Letters, 531 (2012) 193-196.
[42] Y. Liu, X. Dong, P. Chen, Biological And Chemical Sensors Based on Graphene Materials, Chemical Society Reviews, 41 (2012) 2283-2307.
[43] S. Tongay, M. Lemaitre,X. Miao, B. Gila, B.Appleton, A.Hebard,Rectification at Graphene-Semiconductor Interfaces: Zero-Gap Semiconductor-Based Diodes, 2 (2012) 011002.
[44] G. Xu, Y. Zhang, X. Duan, A. Balandin, K. Wang, Variability Effects in Graphene: Challenges and Opportunities for Device Engineering and Applications, Proceedings of The IEEE, 101 (2013) 1670-1688.
[45] O. Kwon, S. Park, J. Hong, A. Han, J. Lee, J. Lee, J. Oh, J. Jang, Flexible FET-Type VEGF Aptasensor Based on Nitrogen-Doped Graphene Converted from Conducting Polymer, ACS Nano, 6 (2012) 1486-1493.

[46] E.Orabona, A.Ambrosio, A.Longo, G.Carotenuto, L.Nicolais, P.Maddalena, Holographic Patterning of Graphene-Oxide Films by Light-Driven Reduction, Optics Letters, 39 (2014) 4263-4266.
[47] L. Jiao, L. Zhang, L. Ding, J. Liu, H. Dai, Aligned Graphene Nanoribbons And Crossbars from Unzipped Carbon Nanotubes, Nano Research, 3 (2010) 387-394.
[48] Y. Hernandez, V. Nicolosi, M. Lotya, F. Blighe, Z. Sun, S. De, I.McGovern, B. Holland, M. Byrne, Y. Gun'ko, High-Yield Production of Graphene by Liquid-Phase Exfoliation of Graphite, Nature Nanotechnology, 3 (2008) 563-568.
[49] A. Reina, X. Jia, J. Ho, D. Nezich, H. Son, V. Bulovic, M. Dresselhaus, J. Kong, Large Area, Few-Layer Graphene Films on Arbitrary Substrates by Chemical Vapor Deposition, Nano Letters, 9 (2009) 30-35.
[50] D. Dikin, S. Stankovich, E. Zimney, R. Piner, G. Dommett, G. Evmenenko, S. Nguyen, R. Ruoff, Preparation And Characterization of Graphene Oxide Paper, Nature, 448 (2007) 457-460.
[51] S.Sonusen, O.Karci, M.Dede, S.Aksoy, A.Oral, Single Layer Graphene Hall Sensors for Scanning Hall Probe Microscopy (Shpm) in 3-300 K Temperature Range, Applied Surface Science, 308 (2014) 414-418.
[52] F.Mehmood, R. Pachter, Density Functional Theory Study of Chemical Sensing on Surfaces of Single-Layer Mos2 And Graphene, Journal of Applied Physics, 115 (2014) 164302.
[53] Z. Zhang, L. Luo, G. Chen, Y. Ding, D. Deng, C. Fan, Tryptamine Functionalized Reduced Graphene Oxide for Label-Free DNA Impedimetric Biosensing, Biosensors & Bioelectronics, 60 (2014) 161-166.
[54] M. Yadav, K. Rhee,S. Park, Synthesis And Characterization of Graphene Oxide/Carboxymethylcellulose/Alginate Composite Blend Films, Carbohydrate Polymers, 110 (2014) 18-25.
[55] P. Li, Z. You, T. Cui, Graphene Cantilever Beams for Nano Switches, Applied Physics Letters, 101 (2012) 093111.
[56] J. Gray, K. Bertness, N. Sanford, C. Rogers, Low-Frequency Noise in Gallium Nitride Nanowire Mechanical Resonators, Applied Physics Letters, 101 (2012) 233115.
[57] Z. Cheng, Q. Li, Z. Li, Q. Zhou, Y. Fang, Suspended Graphene Sensors with Improved Signal and Reduced Noise, Nano Letters, 10 (2010) 1864-1868.
[58] L. Ma, C. Wang, M. Zhang, Detecting Protein Adsorption And Binding Using Magnetic Nanoparticle Probes, Sensors And Actuators B-Chemical, 160 (2011) 650-655.
[59] F. Gutierrez, M. Rubianes, G. Rivas, Dispersion of Multi-Wall Carbon Nanotubes in Glucose Oxidase: Characterization And Analytical Applications for Glucose Biosensing, Sensors And Actuators B-Chemical, 161 (2012) 191-197.
[60] X. Gao, G. Zheng, C. Lieber, Subthreshold Regime has the Optimal Sensitivity for Nanowire FET Biosensors, Nano Letters, 10 (2010) 547-552.
[61] J. Wang, Electrochemical Biosensors: Towards Point-of-Care Cancer Diagnostics, Biosensors & Bioelectronics, 21 (2006) 1887-1892.
[62] J. Delehanty, H. Mattoussi, I. Medintz, Delivering Quantum Dots into Cells: Strategies, Progress And Remaining Issues, Analytical And Bioanalytical Chemistry, 393 (2009) 1091-1105.

[63] V. Singh, D. Joung, L. Zhai, S. Das, S. Khondaker, S. Seal, Graphene Based Materials: Past, Present And Future, Progress in Materials Science, 56 (2011) 1178-1271.
[64] Y. Lin, P. Avouris, Strong Suppression of Electrical Noise in Bilayer Graphene Nanodevices, Nano Letters, 8 (2008) 2119-2125.
[65] A. Balandin, S. Ghosh, W. Bao, I. Calizo, D. Teweldebrhan, F. Miao, C. Lau, Superior Thermal Conductivity of Single-Layer Graphene, Nano Letters, 8 (2008) 902-907.
[66] Y. Xu, K. Sheng, C. Li, G. Shi, Self-Assembled Graphene Hydrogel via a One-Step Hydrothermal Process, ACS Nano, 4 (2010) 4324-4330.
[67] B. Zhang, T. Cui, An Ultrasensitive And Low-Cost Graphene Sensor Based on Layer-By-Layer Nano Self-Assembly, Applied Physics Letters, 98 (2011) 073116.
[68] B. English, W. Min, A . van Oijen, K. Lee, G. Luo, H. Sun, B. Cherayil, S. Kou, X. Xie, Ever-Fluctuating Single Enzyme Molecules: Michaelis-Menten Equation Revisited, Nature Chemical Biology, 2 (2006) 87-94.
[69] R. Wilson, A. Turner, Glucose-Oxidase - An Ideal Enzyme, 7 (1992) 165-185.
[70] W. Shi, Q. Wang, Y. Long, Z. Cheng, S. Chen, H. Zheng, Y. Huang, Carbon Nanodots as Peroxidase Mimetics And Their Applications to Glucose Detection, 47 (2011) 6695-6697.
[71] S. Das, S. Adam, E. Hwang, E. Rossi, Electronic Transport in Two-Dimensional Graphene, Reviews of Modern Physics, 83 (2011) 407-470.
[72] L. Prodi, F. Bolletta, M. Montalti, N. Zaccheroni, Luminescent Chemosensors for Transition Metal Ions, Coordination Chemistry Reviews, 205 (2000) 59-83.
[73] A. Fuente, J. Martinpintado, J. Cernicharo, R. Bachiller, A Chemical Study of The Photodissociation Region NGC-7023, Astronomy & Astrophysics, 276 (1993) 473-488.
[74] A. Riklin, I. Willner, Glucose And Acetylcholine Sensing Multilayer Enzyme Electrodes of Controlled Enzyme Layer Thickness, Analytical Chemistry, 67 (1995) 4118-4126.
[75] T. Cui, B. Zhang, A Simple, Flexible, Low-Cost Acetylcholine Biosensor Based on Nano Self Assembly Of Graphene, Sensor Letters, 9 (2011) 1666-1669.
[76] R. Etzioni, N. Urban, S. Ramsey, M. McIntosh, S. Schwartz, B. Reid, J. Radich, G. Anderson, L. Hartwell, Early Detection: The Case for Early Detection, Nature Review, 3 (2003) 243-252.
[77] J.Todda, B.Freese, A. Lu, D. Held, J. Morey, R. Livingston, P.Goix, Ultrasensitive Flow-based Immunoassays Using Single-Molecule Counting, Clinical Chemistry, 53 (2007) 1990-1995.
[78] M. Lu, D. Lee, W.Xue, T. Cui, Flexible and Disposable Immunosensorsbased on Layer-by-Layer Self-Assembled Carbon Nanotubes And Biomolecules, Sensors and Actuators A: Physical, 150 (2009) 280-285.
[79] C. Campagnolo, K. Meyers, T. Ryan, R. Atkinson, Y. Chen, M. Scanlan, G. Ritter, L. Old, C. Batt, Real-Time, Label-Free Monitoring of Tumor Antigen And Serum Antibody Interactions, Journal of Biochemical and Biophysical Methods, 61 (2004) 283-298.
[80] G. Shekhawat, S.Tark, V. Dravid, MOSFET-Embedded Microcantilevers for Measuring Deflection in Biomolecular Sensors, Science, 311 (2006) 1592-1595.

[81] J. Lee, Z. Wang, J. Liu, Y. Lu,Highly Sensitive and Selective Colorimetric Sensors for Uranyl ($UO_2^{2+}$): Development and Comparison of Labeled and Label-Free DNAzyme-Gold Nanoparticle Systems, Journal of The American Chemical Society, 130 (2008) 14217-14226.
[82] N. Ferrara, H. Gerber, J. LeCouter,The Biology of VEGF And Its Receptors, Nature Medicine, 9 (2003) 669-676.
[83] N. Ferrara, K. Hillan, H. Gerber,W. Novotny, Discovery And Development of Bevacizumab, An Anti-VEGF Antibody for Treating Cancer, Nature Reviews Drug Discovery, 3 (2004) 391-400.
[84] A. Witmer, G. Vrensen, C. Van Noorden, R. Schlingemann, Vascular Endothelial Growth Factors And Angiogenesis in Eye Disease, Progress in Retinal and Eye Research, 22 (2003) 1-29.
[85] T. Zachariadis, A. Poullikkas, The Costs of Power Outages: A Case Study from Cyprus, Energy Policy, 51 (2012) 630-641.
[86] T. Ma, H. Yang, L. Lu, Solar Photovoltaic System Modeling and Performance Prediction, Renewable & Sustainable Energy Reviews, 36 (2014) 304-315.
[87] A. Banerjee, S. Joo, B. Min, NanocrystallineZnO Thin Film Deposition on Flexible Substrate by Low-Temperature Sputtering Process for Plastic Displays, Journal of Nanoscience And Nanotechnology, 14 (2014) 7970-7975.
[88] J. Bisquert, D. Cahen, G. Hodes, S. Ruhle, A. Zaban, Physical Chemical Principles of Photovoltaic Conversion with Nanoparticulate, Mesoporous Dye-Sensitized Solar Cells, Journal of Physical Chemistry B, 108 (2004) 8106-8118.
[89] C. Zheng, J. Pan, Assessment of The Global Ocean Wind Energy Resource, Renewable & Sustainable Energy Reviews, 33 (2014) 382-391.
[90] O.Ileperuma, Gel Polymer Electrolytes for Dye Sensitised Solar Cells: A Review, Materials Technology, 28 (2013) 65-70.
[91] S. Sutty, G. Williams, H. Aziz, Fullerene-Based Schottky-Junction Organic Solar Cells: A Brief Review, Journal of Photonics for Energy, 4 (2014) 040999.
[92] D. Callahan, K. Horowitz, H. Atwater, Light Trapping in Ultrathin Silicon Photonic Crystal Superlattices With Randomly-Textured Dielectric Incouplers, Optics Express, 21 (2013) 30315-30326.
[93] Q. Zhu, Y. Zhang, J. Wang, F. Zhou, P. Chu, Microwave Synthesis of Cuprous Oxide Micro-/Nanocrystals with Different Morphologies and Photocatalytic Activities, Journal of Materials Science & Technology, 27 (2011) 289-295.
[94] M. Law, L. Greene, J. Johnson, R. Saykally, P. Yang, Nanowire Dye-Sensitized Solar Cells, Nature Materials, 4 (2005) 455-459.
[95] D. Macdonald, A. Cuevas, M. Kerr, C. Samundsett, D. Ruby, S. Winderbaum, A. Leo, Texturing Industrial Multicrystalline Silicon Solar Cells, Solar Energy, 76 (2004) 1-3.
[96] C. Fu, A. Grimes, M. Long, C. Ferri, B. Rich, S. Ghosh, S. Ghosh, L. Lee, A. Gopinathan, M. Khine,Tunable Nanowrinkles on Shape Memory Polymer Sheets, 21 (2009) 4472-4476

[97] Y. Sun, W. Choi, H. Jiang, Y. Huang, and J. Rogers, Controlled Buckling of Semiconductor Nanoribbons for Stretchable Electronics Nature Nanotechnol. 1(2006) 201–207.
[98] D. Khang, H. Jiang, Y. Huang, and J. A. Rogers, A Stretchable Form of Single-Crystal Silicon for High-Performance Electronics on Rubber Substrates Science 311 (2006)208–212.
[99] J. Kim, P. Kim, N. Pegard, S. Oh, C. Kagan, J. Fleischer, H. Stone, Y. Loo, Wrinkles And Deep Folds as Photonic Structures in Photovoltaics.Nature Photon. 6(2012) 327–332.
[100] X.He, K.Torrance, F.Sillion, D.Greenberg, A Comprehensive Physical Model for Light Reflection, Computer Graphics, 25(1991)176-186.
[101] R. Siegel, J. Howell.Therms/ Radiarion Heat Transfer. 2nd edition (McGraw-Hill book Company, New York, 1981).
[102] B. Smith, Geometrical Shadowing of a Random Rough Surface, IEEE Transacriorrson Antennas and Propagation, 15(1967)668-671.
[103] Groenewold, J., Wrinkling of plates coupled with soft elastic media, Physica A, 298, (2001)32-45.
[104] L.Ponson, K.Diest, H. Atwater, G.Ravichandran, Bhattacharya, K., Competing failure mechanisms in thin films: application to layer transfer, J. Appl. Phys. 105, 073514 (2009).
[105] S. Hwang, J. Lee, C. Park, H. Lee, C. Kim, C. Park, M. Lee, W. Lee, J. Park, K. Kim, N. Park, C. Kim, A Highly Efficient Organic Sensitizer for Dye-Sensitized Solar Cells, Chem. Commun., 46 (2007) 4887–4889.
[106] N. C. Jeong, C. Prasittichai, J. THupp, Photocurrent Enhancement by Surface Plasmon Resonance of Silver Nanoparticles in Highly Porous Dye-Sensitized Solar Cells, Langmuir, 27 (2011)14609-14614.
[107] B. Lin, The Ending of Optical Lithography and The Prospects of Its Successors, Microelectron. Eng. 83 (2006) 604.
[108] P. Fischer, S. Chou, 10 nm Electron Beam Lithography and Sub-50 nm Overlay Using A Modified Scanning Electron Microscope, Appl. Phys. Lett. 62 (1993) 2989.
[109] E. A. Costner, W. Lin,W. Jen, C. G. Willson, Nanoimprint Lithography Materials Development for Semiconductor Device Fabrication, Annu. Rev. Mater. Res., 39 (2009) 155.
[110] R. D. Piner, J. Zhu, F. Xu, S. Hong, C. A. Mirkin, "Dip-Pen" Nanolithography, Science, 283 (1999) 661.
[111] M. Park, C. Harrison, P. M. Chaikin, R. A. Register, D. H. Adamson, Block Copolymer Lithography: Periodic Arrays of ~$10^{11}$ Holes in 1 Square Centimeter, Science, 276 (1997) 1401.
[112] T. Ishibashi, T. Toyoshima, N. Yasuda, T. Kanda, H. Tanaka, Y. Kinoshita, N, Watase, R. Eakin, “Advanced Micro-Lithography Processes with Chemical Shrink Technology”, Jpn. J. Appl. Phys. 40 (2001) 419.
[113] M. Domanski, R. Luttge, E. Lamers, X. F. Walboomers, L. Winnubst, J. A. Jansen, J G E Gardeniers, Submicron-Patterning of Bulk Titanium by Nanoimprint Lithography and Reactive Ion Etching, Nanotechnology 23 (2012) 065306.

[114] T. Wu, H. Lu, C. Lin, Dependence of Transport Rate on Area of Lithography and Pretreatment of Tip in Dip-Pen Nanolithography, Langmuir, 28 (2012) 14509.
[115] J. Poelma, K. Ono, D. Miyajima, T. Aida, K. Satoh, C. Hawker, Cyclic Block Copolymers for Controlling Feature Sizes in Block Copolymer Lithography, ACS Nano, 6, (2012) 10845.
[116] C.W. B. Pemg, Y. Shen, Y. Lin, Microfluidic Chip Fabrication Using Hot Embossing and Thermal Bonding of COP, Polym. Adv. Technol., 10.1002/pat.1447 (2009).
[117] C. W. Tsao, D. L. DeVoe, Bonding of Thermoplastic Polymer Microfluidics, Microfluid. Nanofluid., 6 (2009) 1.
[118] C. K. Fredrickson, Z. Xia, C. Das, R. Ferguson, F. T. Tavares, Z. H. Fan, Effects of Fabrication Process Parameters on the Properties of Cyclic Olefin Copolymer Microfluidic Devices, J. Microelectromech. Syst., 15 (2006) 1060.
[119] A. Grimes, D. N. Breslauer, M. Long, J. Pegan, L. P. Lee, M. Khine. Shrinky Dink Microfluidics: Rapid Generation of Deep and Rounded Channels, Lab Chip 8 (2008) 170.
[120] D. Lee, S. H. Park, H. Yang, K.-H. Chung, T. H. Yoon, S.-J. Kim, K. Kim, Y. T. Kim. Bulk-Micromachined Submicroliter-Volume PCR Chip With Very Rapid Thermal Response and Low Power Consumption, Lab Chip 4 (2004) 401.
[121] N. Stutzmann, T. A. Tervoort, K. Bastiaansen, P. Smith, Patterning of Polymer-Supported Metal Films by Microcutting, Nature, 407 (2000) 613.
[122] R. Meehan, S. Burns, Modeling Cutting: Plastic Deformation of Polymer Samples Indented With a Wedge, J. Manuf. Sci. E-T ASME, 129 (2007) 477.
[123] R. Meehan, S. Burns, Mechanics of Cutting and Slitting Webs, Experimental Mechanics, 38 (1998) 103.
[124] C. Sharma, A. Verma, M. Kulkarni, D. Upadhyay, A. Sharma, Microfabrication of Carbon Structures by Pattern Miniaturization in Resorcinol-Formaldehyde Gel, Applied Materials and Interfaces, 2 (2010) 2193.
[125] J. Rodriguez, M. Salazar, L. Steffan, M. Pignata, J. Franzaring, A. Klumpp, A. Fangmeier, Assessment of Pb And Zn Contents in Agricultural Soils And Soybean Crops Near to A Formerbattery Recycling Plant in Cordoba, Argentina, Journal of Geochemical Exploration, 145 (2014) 129-134.
[126] Y. Nie, D. Ping, Y. Zhao, P. Wang, L. Xing, Y. Zhang, X. Xue, The Conversion of PN-Junction Influencing The Piezoelectric Output of A CuO/ZnO Nanoarray Nanogenerator And Its Application as A Room-Temperature Nanomatrial based Active $H_2S$ Sensor, Nanotechnology, 25 (2014) 265501.
[127] P. Peumans, A. Yakimov, S. R. Forrest, Small Molecular Weight Organic Thin-Film Photodetectors and Solar Cells, J. App. Phy. vol. 93 (2003) 3693-3724.
[128] B. Zhang, T. Cui, Tunable Shrink Induced Graphene Composites for Chemical Sensors and Microfluidics, IEEE International Conference on Micro Electro Mechanical Systems, January 29- February 02, 2012, Paris, France, pp. 1360-1363.